Pathways to a Metallic Hydrogen

Dissertation Advisor | Author

Professor Isaac F Silvera | Vasily Dzyabura

Pathways to a metallic hydrogen

Abstract

The primary subject of this thesis is the study of warm dense hydrogen by means of pulsed laser heating in the pressure region 1 to 2 Mbar and temperatures above the melting line, where a liquid-liquid phase transition from the insulating molecular fluid to a conducting atomic hydrogen fluid, so called plasma phase transition (PPT), was predicted to take place. The first evidence of the PPT under static compression is reported. The observations are in agreement with the negative slope phase line predicted by *ab initio* methods.

The second subject of this thesis is the development of instrumentation and pulsed laser heating measurement techniques necessary for studying hydrogen under these high pressure and temperature conditions. This includes a design of a cryogen-free optical cryostat with a short optical distance suitable for high pressure studies; a technique of a controlled preparation (indentation) of a gasket, which is a vital part of any high pressure experiment inside a diamond anvil cell; and an in-depth discussion of spectral data reduction methods for pyrometry in the case of pulsed laser heating.

The third part of this thesis, closely related to the second, is the demonstration of a successful application of the measurement techniques for a control system: study of the behavior of platinum under pulsed laser irradiation. A surface reconstruction of platinum is reported at temperatures well below the bulk melting temperature of platinum.

The last subject of this thesis is a report of observation of pressure induced metallization of amorphous germanium monoxide. The transition to the amorphous metallic state is observed at ~12 GPa. The resulting metallic phase is metastable: GeO stays metallic upon releasing the pressure to zero. This

transition bears similarities to previously observed IM transitions in SiO and SnO, but it has its own unique features.

Table of Contents

Acknowledgments

I am grateful to many people who were there for the last six and something years. Some of them I'll list, but there are much more.

I thank:	f*or:*
Ike Silvera	being an **exceptional** advisor
Prof. Kaxiras, Prof. Pershan	being my dissertation committee
Lisa Cacciabaudo, Sheila Fergusson	navigation in academic requirements
Bill Nellis, Anatoly Dementyev, Eran Sterer, Goutam Dev Mukherjee	senior support and sharing their experience
Stan Cotreau	creating the unique machine shop atmosphere
Ashkan Salamat	a great help during preparation for my defense
Alex Tonyushkin	a rational vision of life and wisdom
Alex Soldatov	a very different type of wisdom
Shanti Deemyad	endless optimism and energy
Zhenya Zarechnaya, Mohamed Zaghoo, Javier R. Fuertes, Jieping Fang, Richard Dweck	the team
Timur, Daniyar, Max, Luda, Anton	the gang
Rano, Lena	the help
My parents Galina and Sergey, my brother Zhenya	the family
My wife Dasha and our daughters Nika and Katya	the inspiration

Dedicated, definitely dedicated…

1. Introduction

The focus of this research was to extend the knowledge of the phase diagram of hydrogen at high pressure and temperature, therefore a large part of the thesis is devoted to this subject

Chapter 2 is, essentially, a standalone piece: every aspect of the hydrogen project is described in it. A short review on the history of the subject is given in section 2.1. It is followed by a thorough description of the experimental apparatus and procedures, section "2.2 Experimental Method". All the high pressure specific terminology is defined there. Sections 2.2.6 to 2.2.8 are mostly for future reference, so that an accurate picture of the experiment could be reconstructed if such a need arises. The "2.2.9 History of measurement runs" section provides a brief story of our failures and successes with hydrogen over the course of my study. The last section of chapter 2, section 2.3 accomplishes several goals. First, we up the framework needed to analyze the spectroscopic data from the time averaged observations in the section 2.3.1. Next, section (2.3.2) deals with the separation of the actual spectral data into the part which can be analyzed with the methods proposed and all the contaminating background which turned out to be quite a challenging enterprise. In the remainder of the section (2.3.3 to 2.3.5) we discuss the physics of the observed plateaus, present the reduced data and discuss the implications for the phase diagram of hydrogen.

Chapter 3, "Platinum surface reconstruction upon pulsed laser heating" is closely related to Chapter 2. We describe the behavior of platinum under condition of pulsed laser irradiation. The discussion has a dual purpose: first, platinum exhibits interesting behavior, namely cold surface reconstruction which is described in detail; second, platinum is the material which was used in the hydrogen experiment to couple heating laser radiation into heat for hydrogen warming and then in reverse, to emit the thermal radiation which was analyzed later to infer the temperature evolution of the hydrogen sample. This makes platinum a good benchmark system to show that the proposed method of melting detection with laser heating works. That is, if it fails on platinum, it would be extremely difficult

to defend the results of the hydrogen experiment. As it turned out, the melting temperature of platinum can be measured accurately despite the surface reconstruction.

The rest of the thesis, chapters 4, 5 and 6 are completely independent. Chapters 4 and 6 describe instrumentation for the experiment and chapter 5 reports an observation of the pressure induced insulator to metal transition in amorphous germanium monoxide.

2. Hydrogen at high pressure: the Melting line and Plasma Phase transition.

2.1 Problem statement and literature review

Hydrogen is the most simple and the most abundant element in the visible universe. The variety of physical states it can take as its density is varied is noteworthy: the density of hydrogen in the solid state alone can change by more than one order of magnitude in the range of pressures experimentally achievable in static experiments.

There is no agreement on the nature of states of hydrogen even within the experimentally accessible region of the phase diagram. The search for one particular state, metallic hydrogen, which was predicted more than 75 years ago by Wigner and Huntington [1] to appear at a pressure of 25 GPa, long since surpassed, has been for a long time a Holy Grail of high pressure physics. There are several claims of creating metallic hydrogen: to date previous claims were proved wrong and the most recent claim is considered controversial [2] [3].

Outside the currently accessible region several interesting phenomena are predicted. Among them are a high temperature superconductivity (Ashcroft 1968 [4], Cudazzo 2008 [5]) and a new type of ordered quantum fluid (Babaev 2004 [6]) with a spectrum of states ranging from superconductor to superfluid.

Hydrogen is a quantum solid: because of its large zero point motion, it is beneficial for the crystal to expand. A way to look at it is that you reduce the interaction energy or overlap of hard cores (resulting from large zero point motion amplitude) at a sacrifice of attractive interaction energy in the well. High compressibility of the zero pressure solid is a direct consequence of this: the initial compression is against the weaker ‘kinetic pressure’ rather than harder ‘core’ pressure [7]. Numerically one can define a quantum parameter as a ratio of root mean square zero-point amplitude to the lattice constant. For molecular hydrogen it is 0.18, which is only surpassed by helium (~0.3 depending on isotope). As the

pressure goes up, hydrogen becomes more classical, but it stays quantum enough to pose a challenge to the current *ab initio* numerical methods: up to date there is no agreement on structures of high pressure solid phases. The region of molecular liquid – atomic liquid – solid triple point is not described by *ab initio* methods at all.

Made of simple parts, yet difficult to compute by traditional methods hydrogen presents a testing ground and a benchmark for numerical techniques. Thus, knowledge of the hydrogen phase diagram would allow better understanding these methods and advance the techniques.

The behavior of hydrogen at and above the melting line is far from simple as well. Interesting phenomena from a fundamental point of view include short range ordering in the molecular liquid above 100 GPa, possibly responsible for the unusual behavior of the melt line [8] and a possibly sharp liquid-liquid phase transition (LLT) from insulating molecular state to conducting atomic liquid, called the plasma phase transition, or PPT. From a practical point of view the equation of state of warm dense hydrogen is important for modeling planets such as Jupiter and Saturn, and fusion related topics, such as inertial confinement fusion. As an example one can compare a density step observed in deuterium by Fortov et al [9] to that of plutonium, which has very important practical implications.

This work is going to concentrate on probing the properties of hydrogen at and above the melting line. This includes the melting and the liquid to liquid phase transition.

2.1.1 Melting and above: experimental history

The melting line of hydrogen has been studied experimentally by many researchers, starting almost 100 years ago at the Leiden laboratory in the Netherlands. [10] I will review more recent measurements. In 1985 Diatschenko et al [11] performed thorough measurements of the melting line up to 7.7 GPa and 373 K using visual and barometric detection with essentially static temperature conditions. Their data was fitted well by the Simon-Glatzel [12] empirical equation which is an integration of the Clausius-Clapeyron equation assuming that the inverse of the right hand side varies linearly with pressure: $d(\frac{L}{\delta V})/dP = const$. This extrapolation works well for describing the melting behavior of

solids bonded by van der Waals forces such as solid gases. One of the consequences of the chosen approximation is that it is only capable of describing melting curves if the melting temperature increases with the pressure which is the most common case.

The next major work was done by Datchi at al in 2000 [13] up to 15.2 GPa and 530 K. They used essentially the same technique as Diatschenko et al. The pressure range was limited by the fact that hydrogen diffused out of the cell and a lot of work was performed to find a material to suppress this. They were not able to completely stop the diffusion and gasket embrittlement, but only slow it down. The important result they obtained is that the Simon equation does not accurately describe the behavior of hydrogen. They used another empirical relationship to fit the data, after Kechin [14]. This approximation is a result of another Taylor expansion of the right hand side of the Clausius-Clapeyron equation with respect to pressure, this time, to second order. The resulting equation is:

$$T = T_0 \left(1 + \frac{\Delta P}{P_0}\right)^a \exp\left(-c\Delta P\right)$$

with T_0 = 14.025 K, P_0=0.0286 GPa, c=0.046 GPa^{-1} and a= 0.589 for hydrogen. It is interesting that Kechin in his paper published the fit for hydrogen based on Diatschenko's data. Extrapolation of the fit suggested presence of a maximum in the melting line at pressure at ~128 GPa.

The next advance was done by Gregoryanz *et al* 2003 [15]: the curve was extended to 44 GPa and 800 K. A new indirect detection method was used – there is an observed small positive discontinuity in the hydrogen vibron frequency (measured via Raman scattering) shift with respect to temperature which happens at melting. The magnitude of the discontinuity was decreasing as a function of pressure and eventually, at the pressure of 72 GPa it became too small to be reliably detected. Thus, the last (the highest) pressure point where the melting was measured was 44 GPa. New points were well fitted with the Kechin melting law, indicating that the melt line maximum is situated at the pressure lower than expected from extrapolation of Datchi *et al* data, namely ~100 GPa, but still outside the measurement range. In this experiment resistive heating of the whole cell was used, similar to Datchi et al. The progress

was enabled by the use of alumina diffusion barrier to inhibit diffusion into the gasket and use of fast automated measurement techniques allowing data collection before the diamonds failed. Measurement times were limited by hydrogen diffusion into the diamonds and their embrittlement and failure

The problem of diamond embrittlement was addressed in the works of Deemyad *et al* [16], Eremets *et al* [17] and Subramanian *et al* [18]. They are based on the laser heating of transparent hydrogen sample in contact with a metal absorber and detecting melting by various methods.

In the first work out of these three, Deemyad and Silvera, a short pulsed laser (~100 ns) was used to heat a platinum absorber embedded in the hydrogen sample. This time is small compared to the time required for heat to diffuse out to diamonds: only a thin layer of hydrogen adjacent to the absorber surface is heated with typical thickness of 1 micron. Averaged over the laser pulse, temperature can be measured by means of optical pyrometry and the melting is detected as a singular point in the curve relating this temperature and the energy of the incoming laser pulse. This technique is the basis of my thesis and will be discussed in greater detail. The melt line was extended to 80 GPa and the peak was detected at 64.7 GPa, 1055 K for the first time in the experimental history. The experiment was not terminated due to any inherent design problems, but rather due to pressure measurement problems due to diffusion of hydrogen into the ruby balls which quenched the fluorescence which is used as a pressure gauge. The measured melting line showed a sharp peak, with a sparse number of data points.

In the work of Eremets *et al* a continuous short duration (10s of seconds) laser was used; absorber material was platinum as well and the resistance of the absorber was monitored as a function of the absorber surface temperature. Melting was characterized by speckle motion and, in case of the highest pressure of 146 GPa, by a sudden drop in resistivity of the absorber. The authors suggested that hydrogen dissociation was the cause of this drop. This measurement advanced the melting line to a pressure of 146 GPa and showed general agreement with the earlier data on the presence of the maximum, but no measurements were made in the region 45 to 80 GPa. Thus the direct comparison with the Deemyad and Silvera work is difficult.

The appearance of a maximum in the melting curve is not a unique property of hydrogen; there are other materials that exhibit similar behavior. After Bonev [19], examples are open crystalline structures (water, graphite) and closed packed crystals where valence electrons are promoted to higher orbitals upon compression (i.e. 6s to 5d in cesium). A possible explanation is that in the liquid, structural or electronic phase transitions are taking place continuously as a function of pressure and sharp in the solid. In the case of hydrogen there is theoretical [8] evidence of appearance of a short range ordering in fluid after 100 GPa.

The work of Subramanian et *al* provides experimental evidence of the 'existence of a state of the fluid having significantly modified intramolecular bonding'. In this work hydrogen was laser heated using a continuous infrared (1.07 μm) fiber laser and a iridium absorber. The Raman signal of the vibron mode was measured (excited by argon ion laser). Local heating and use of additional Al_2O_3 diamond insulation allowed them to reach estimated temperatures about 2000 K on selected unreported pressures. This allowed data collection over a much broader temperature range compared with their previous work of 2003 [15] without early diamond breakage. Resulting spectra were spatially deconvoluted using input from finite element model for temperature distribution in the cell and known extrapolated vibron frequency shift temperature dependence, $\delta\nu(T)$. The analysis suggested that the known $\delta\nu(T)$ along with the modeled thermal gradient cannot describe the observed spectra accurately. The authors suggest two different heuristic models of $\delta\nu(T)$ which fit the data better. This, combined with observation of dynamics of roton spectra change, suggest a different nature of the low and high pressure liquids. The results need to be verified though because the authors quote presence of chemical reactions of hydrogen with the absorber and there is a strong disagreement with the earlier results of the same group concerning the amplitude of the discontinuity in $\delta\nu(T)$ [1]

Outside the realm of static compression, the warm dense hydrogen and its isotopes were studied by means of shock compression. There are two experimental results suggesting presence of the insulating

[1] Discontinuity of $\delta\nu(T)$ at 60 GPa in [18] is reported to be 80 cm^{-1} and less then 1cm^{-1} in [15].

liquid- conducting liquid crossover or a phase transition above the melting line. Nellis et al [20] using reverberating shock wave compression achieved a conductive state of hydrogen sample at 140 GPa and temperature calculated to be 2600 K. They reported a gradual change in conductivity of the sample up to the values comparable to the minimum metallic conductivity. The temperature of the transition was not measured directly, but calculated using the hydrogen equation of state as an input parameter. Since it is not known precisely in the region of interest, the authors estimate the uncertainty of temperature determination as 30%. The conductivity was measured directly, and thus can be interpreted as metallic state, but of unknown structure, presumably monatomic and possibly liquid [21]. This is an important point of the phase diagram which sets the limits of the region to be explored in static measurements.

Fortov *et al* [9] performed a shock compression study of deuterium and hydrogen where reverberating shocks produced with high explosives were used to ramp compress the liquid sample, presumably reaching temperatures in the range of 3–8 $\times$ 10^3 K. Using highly resolved flash X-ray diagnostics, they were able to measure the compressibility of the deuterium liquid and found a 20% increase in density, which is expected for a first order phase transition. In a separate experiment on hydrogen they reported that the conductivity increases sharply by approximately 5 orders of magnitude, compatible with the work of Nellis et al. It is important to note that in these experiments the temperature is estimated using a "confined atom" model whose accuracy is difficult to assess.

From the theoretical standpoint this behavior was most recently addressed by Bonev [19] (melting) Tamblyn Bonev [8], Morales *et al* [22] and Lorenzen *et al* [23]. They agree on the presence of liquid-to-liquid phase transition (LLT), while emphasizing limited capability of present theoretical techniques in the region where the LLT and melt lines meet. An extensive review on the subject was recently published [24].

2.1.2 Bibliography

[1] E. Wigner and H. B. Huntington, "On the Possibility of a Metallic Modification of Hydrogen," *J. Chem. Phys.,* vol. 3, no. 12, 1935.

[2] W. J. Nellis, A. L. Ruoff and I. F. Silvera, "Has Metallic Hydrogen Been Made in a Diamond Anvil Cell," *Preprint http://arxiv.org/abs/1201.0407,* 2012.

[3] I. Amato, "Metallic hydrogen: Hard pressed," *Nature,* vol. 486, no. 7402, p. 174–176, 2012.

[4] N. W. Ashcroft, "Metallic Hydrogen: A High-Temperature Superconductor," *Phys. Rev. Lett,* vol. 21, no. 26, p. 1748–1749, 1968.

[5] Cudazzo and e. al, "Ab Initio Description of High-Temperature Superconductivity in Dense Molecular Hydrogen," *Phys. Rev. Lett.,* vol. 100, no. 25, 2008.

[6] E. Babaev, A. Sudbo and N. W. Ashcroft, "A superconductor to superfluid phase transition in liquid metallic hydrogen," *Nature ,* vol. 431, 2004.

[7] I. F. Silvera, "The solid molecular hydrogens in the condensed phase: fundamentals and static properties," *Rev. Mod. Phys,* vol. 52, no. 2, 1980.

[8] I. Tamblyn and S. Bonev, "Structure and Phase Boundaries of Compressed Liquid Hydrogen," *Phys. Rev. Lett. ,* vol. 104 , no. 6, 2010.

[9] V. E. Fortov and e. al, "Phase Transition in a Strongly Nonideal Deuterium Plasma Generated by Quasi-Isentropical Compression at Megabar Pressures," *Phys. Rev. Lett.,* vol. 99, no. 18, 2007.

[10] H. Kamerlingh Onnes and W. v. Gulik, " The melting-curve of hydrogen to 55 kg/cm(2)," *Commun. Phys. Lab. Univ. Leiden,* vol. 184A, pp. 1-6, 1926.

[11] V. Diatschenko, C. W. Chu, D. H. Liebenberg, D. A. Young, M. Ross and R. L. Mills, "Melting curves of molecular hydrogen and molecular deuterium under high pressures between 20 and 373 K," *Phys. Rev. B,* vol. 32, no. 1, p. 381–389 , 1985.

[12] F. Simon and G. Glatzel, *Z. Anorg (Allg.) Chem,* vol. 178, pp. 309-312, 1929.

[13] F. Datchi, P. Loubeyre and R. LeToullec, "Extended and accurate determination of the melting curves of argon, helium, ice H2O,and hydrogen H2," *Phys. Rev. B,* vol. 61, no. 10, 2000.

[14] V. V. Kechin, "Thermodynamically based melting-curve equation," *Phys.: Condens. Matter,* vol. 7, no. 3, 1995.

[15] E. Gregoryanz, A. F. Goncharov, K. Mi, H. Mao and R. J. Hemley, "Raman Spectroscopy of Hot Dense Hydrogen," *Phys. Rev. Lett.,* vol. 90, no. 17, 2003.

[16] S. Deemyad and I. Silvera, "Melting Line of Hydrogen at High Pressures," *Phys. Rev. Lett.,* vol. 10, no. 15, 2008.

[17] M. Eremets and I. Troyan, "Evidence of maximum in the melting curve of hydrogen at megabar," *JETP Letters,* vol. 89, no. 4, pp. 174-179, 2009.

[18] N. Subramanian, A. Goncharov, V. Struzhkin, M. Somayazulu and a. R. J. Hemley, "Bonding changes in hot fluid hydrogen," *PNAS,* vol. 108 , no. 15, pp. 6014-6019, 2011.

[19] S. Bonev, E. Schwegler, T. Ogitsu and G. Galli, "A quantum fluid of metallic suggested by first-principles calculations," *Letters to Nature,* vol. 431, pp. 669-672 , 2004.

[20] W. J. Nellis, S. T. Weir and A. C. Mitchell, "Minimum metallic conductivity of fluid hydrogen at 140 GPa (1.4 Mbar)," *Phys. Rev. B,* vol. 59, no. 5, p. 3434–3449 , 1999.

[21] V. Labet, P. Gonzalez-Morelos, R. Hoffmann and N. Ashcroft, "A fresh look at dense hydrogen under

pressure. I. An introduction to the problem, and an index probing equalization of H--H distances," *The Journal of Chemical Physics,* vol. 136, p. 074501, 2012.

[22] M. Morales, C. Pierleoni, E. Schweglerd and D. M. Ceperley, "Evidence for a first-order liquid-liquid transition in high-pressure hydrogen from ab initio simulations," *PNAS,* vol. 107, no. 29, pp. 12799-12803, 2010.

[23] W. Lorenzen, B. Holst and R. Redmer, "First-order liquid-liquid phase transition in dense hydrogen," *Physical Review B,* vol. 82, p. 195107, 2010.

[24] J. M. McMahon, M. A. Morales, C. Pierleoni and D. M. Ceperley, "The properties of hydrogen and helium under extreme conditions," *Rev. Mod. Phys.,* vol. 84, no. 4, pp. 1607--1653, Nov 2012.

2. 2 Experimental Method

2.2.1 Diamond Anvil Cell for Hydrogen

High pressure spectroscopic studies were performed using a gasketed diamond anvil cell (DAC). A DAC generates pressure by squeezing a sample between two small (a fraction of millimeter) flat surfaces of diamond anvils (Fig. 2.1), called the culet flat. In order to prevent sideways escape of a sample, it is confined by a metal gasket. Gasketed DACs were first developed in 60s at National Bureau of Standards [1] as a safer and more accessible alternative to large hydraulic Bridgeman-type presses [2]. Many types of DACs were developed since then for different applications [3][4] . The history of diamond cell creation and an overview is thoroughly described by William Basset in [5].

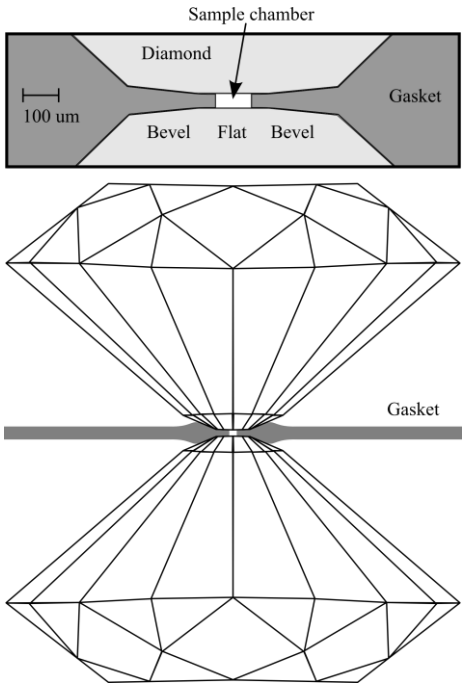

Fig. 2.1: An overall view and a close up of a gasket pressed between two diamonds with undeformed sample chamber. The latter is to scale.

A cylinder piston type cell was used in hydrogen experiments, schematically shown in Fig. 2.2. This design features high dimensional stability, which is required for achieving pressures exceeding one megabar. Both diamonds are mounted on metallic pistons (6L, 6R see Fig. 2.2). One piston (6R) is backed by a threaded insert, so it cannot move when loaded; another can be pushed by translating the cradle (4) which is connected to a pivoted pair of lever arms (3) on each side of the cell. Arms are rotated by advance of the wedge (2) and flexible enough to allow gradual load application and strain measurement. The wedge is driven by the lead screw (1) with total mechanical advantage of 67 microns of diamond travel per one revolution of the screw. For improved precision of motion of the piston there are four precision cylindrical rails (not shown) connected to the cylinder which slide in corresponding grooves. Two heaters and a calibrated silicon diode thermometer are mounted on the cell and allow for temperature control. A 350 ohm strain gauge (7) half-bridge mounted on a lever arm allows measurement

of the load applied to anvils with an accuracy of ~ 10N which is important during gasket preparation and a high pressure run.

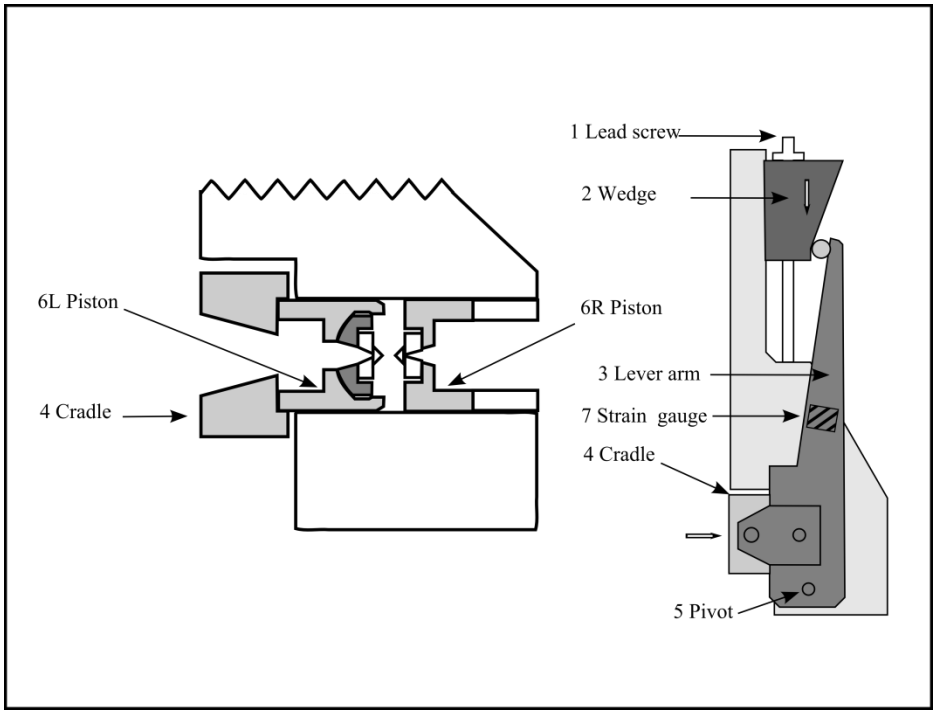

Fig. 2.2: Diamond anvil cell

The diamonds used were low fluorescence Type I, modified brilliant cut, approximately 0.25 carat, from Almax Industries. Modified brilliant cut is a brilliant cut with the table (the largest flat face perpendicular to symmetry axis) of a diamond partially polished down to increase the support area. In order to achieve our experimental goals a number of special techniques were developed or implemented and these will be described in the following paragraphs. Diamonds tips were polished to form a flat with diameter of 100 microns and then beveled at a small angle (6...8 degrees) with the diameter of the beveled area being 300 microns. Beveling is the standard way of diamond shaping of high pressure anvils; it allows reaching pressures above one megabar by counteracting diamond cupping of the culet flat at high pressures [6].

A major problem for studying hydrogen at high pressures is diffusion of hydrogen into the diamond and subsequent embrittlement and failure, in particular at room temperature and higher. Diamonds were treated to suppress destructive hydrogen diffusion. This treatment consisted of two

independent steps: reactive ion plasma etching (REI) and placement of a diffusion barrier on the diamonds by means of atomic layer deposition (ALD). REI work was performed by Evgeniya Zarechnaya and a detailed report is going to be published. The goal of REI etching is to remove the top layer of diamond (a few microns) which was subject to mechanical stress and damage on nanometer level during polishing, thus achieving two goals: (a) eliminating sub surface defects which present potential pathways for hydrogen to diffuse into the anvil and (b) smooth out the diamond surface so no damage is caused by flow of gasket material along the diamond surface. The etching was done using a combination of slow argon chlorine etch which tends to smooth out the surface and fast, essentially chemical, oxygen ion etch which does not maintain flatness of the diamond surface very well unless specific etching conditions are met. The total thickness of the removed diamond layer was estimated as 3 to 5 μm. [7]

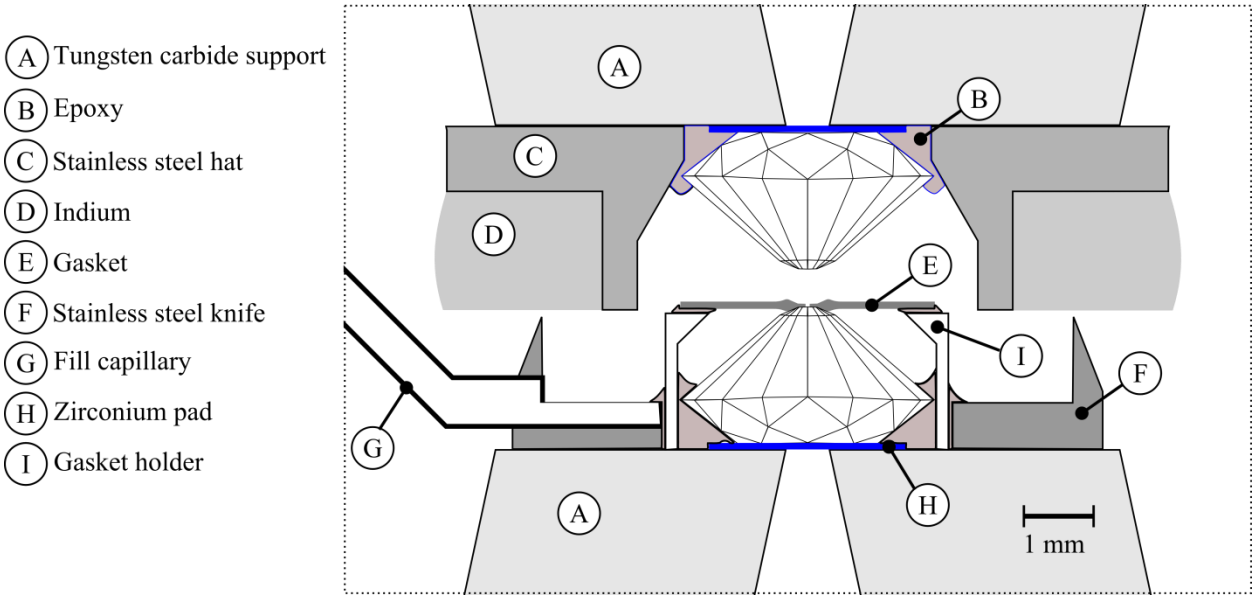

Fig. 2.3: Minichamber and diamonds

After the RIE step, diamonds were acid and oxygen plasma cleaned to remove an amorphous layer of carbon and the first layer (out of several) of alumina was deposited using the Savannah ALD reactor (Cambridge NanoTech at the Harvard Center of Nanoscale Sciences (CNS)). The precursors we used were water and trimethylaluminum and the process temperature was set at 100 degrees C. This first layer is fairly strong, but nevertheless can be mechanically removed from diamond. We chose to apply the ALD barrier at least twice per diamond: (a) right after REI etch and thorough cleaning when ALD has

the best chance of bonding to the uncontaminated diamond surface and (b) right before the run, after the gasket indentation, which could have damaged the first layer. Both barriers were either 10 or 15 nm thick, depending on the run (without any observable difference). By the time the second coating was applied the diamonds were already mounted on tungsten carbide seats with epoxy, therefore we were unable to perform a thorough acid cleaning, which made the second coating bonding not as good as the first one. An added benefit of the ALD coating is that even at thicknesses of tens of nanometers it works as an antireflection coating, increasing the amount of infrared signal that can be collected from the sample and reducing the reflection amplitude of lasers from the diamond back surface.

Each diamond was mounted on a tungsten carbide (WC) seat (Fig. 2.3, A) with a zirconium foil acting as a deformable cushion between a diamond and a seat. If no cushion is used, edges of the diamond anvil indent into the seat and it needs to be re-polished for every high pressure run. The purpose of a WC seat is to spread the load from a relatively small area of the diamond table (to a larger area), so the body of the DAC is not deformed. Diamonds are bonded to the WCs using Lord 320/322 epoxy under a load comparable to that of high pressure runs to ensure absence of plastic deformations later on. No epoxy goes under diamonds. The mini chamber was than assembled around the diamonds after mounting them on the WCs. It is described in greater detail in the corresponding section.

The DAC has provisions for precise diamond alignment, which is one of conditions for achieving high pressures [8]. The fundamental problem is that the opposing anvil geometry is subject to instability: when the sample shifts radially off axis by a distance above a certain threshold, there is no counteracting force and it will continue to drift until it reaches the edge of an anvil. This scenario is referred to as a gasket blow-out and is among the most frequent reasons for termination of high pressure runs, the other being failure of the diamonds at higher pressures. Clearly, if diamonds are misaligned at the start of a run, the radial symmetry is broken and there is an easy direction for blow-out. In our cell diamonds can be precisely aligned by

- Lateral translation of right (6R Fig. 2.2) WC seat in piston by four setscrews

- Rocking hemispherical mount of left WC seat in socket by four setscrews
- Use of precision stop to set angular position of R piston in the bore

This takes care of 5 degrees of freedom, the sixth is diamond separation. The first of the above mentioned two alignments is done when the cell is assembled without a gasket in it: the diamond culets are brought together and can be seen simultaneously through R diamond (defined in Fig. 2.2) table with an optical microscope providing visual feedback. The tilt is detected by observing interference fringes in reflected white light and corrected by adjusting until there are no fringes of white light, that is a single color is observed across the culet flat. From experience, relative tilt with slope 0.1% (one red to green transition or half a fringe across 100 micron flat diameter) is enough to enable(trigger) a blow-out.

To make gaskets, 10 mil thick rhenium stock was sputter coated with a 50 nm gold layer on both sides to decrease stress on the diamonds during indentation and cut into 5 mm diameter gasket blank disks using electrical discharge machining (EDM). A gasket was then indented to be 20 μm thick using a procedure described in the chapter 5. Care was taken to keep the gasket-diamond interface clean from contamination such as oil, because when the enough load is applied, trapped grease would indent into the rhenium and the resulting surface of the gasket will not be conformal to the diamond surface which prevents sealing of the liquid hydrogen sample during loading of the sample. If, however, no contamination is present, then the gasket conforms to the surface even if a rough rhenium stock used and the softer gold on the surface flows and fills any micro scratches on the gasket. The indented gasket was then abrasively cleaned in sonicator with 5 μm alumina water slurry to remove excess gold and increase the diamond-gasket friction. The friction is important as it stabilized the sample against a blow-out. We had multiple runs fail because of what was later identified as slippery gasket, a condition found if the gold was too thick (see History of Measurement Runs section of this chapter for details).

To drill a sample hole either EDM or focused ion beam (FIB) was used. Both methods can provide a micron level centering precision. For the hole sizes we used (50 μm diameter) EDM is slightly more practical, because of financial considerations; time wise these two methods are comparable if

overhead of making an EDM electrode is taken into account. As the hole size gets smaller, FIB is clearly preferable because FIB becomes faster and making smaller EDM electrodes gets more time consuming. In the case of EDM use, the gasket had to be abrasively cleaned after drilling to remove re-deposited rhenium from the edges of the gasket hole. If not, this material is pushed into the sample chamber and the clear aperture is reduced by 10% or more in radius or 20% in area which is not acceptable.

Diamonds then were plasma cleaned and a 10 nm layer of alumina diffusion barrier was deposited by means of ALD. As described above, we used atomic layer deposition with water and trimethylaluminum as precursors, process temperature was 80 degrees C. The lower process temperature compared to the first ALD layer was used to prevent thermal damage of the epoxy.

As a last step in the gasket preparation, the clean gasket was mounted in the DAC under load using Lord 320/322 epoxy. Epoxy was applied to the holder (Fig. 2.3I), the gasket was placed in the DAC and the cell was closed and a load was applied to diamonds. The load was chosen to be above the "visual sealing" load (defined ahead) and below the yield strength (YS) of a drilled gasket. By "visual sealing " load we mean the load when the diamond-gasket distance gets smaller than approximately 50 nm across the *whole* contact surface as indicated by interference fringes of white light. The yield strength of a gasket was determined independently as a load when the gasket starts yielding. For as-indented gasket YS is essentially the indentation load, for a drilled gasket it depends on geometry and is normally about 80% of the indentation load. This loading allows flattening of the gasket surface to remove any small protrusions and improve sealing when the actual sample is loaded. If the gasket would not visually seal before YS is reached it was discarded. Normally, visual sealing happened somewhere between 20 and 40% of the indentation load.

After the gasket is prepared and mounted on the diamond anvil, the absorber and ruby pressure markers were placed into the sample chamber. This was done using mechanical micromanipulator equipped with a tungsten needle.

2.2.2 Sample chamber and absorber design

A scale drawing of a sample chamber is show in Fig. 2.4. The absorber, ruby standoffs and rubies for pressure determination are shown. A microscope image of a cavity prepared for a run is shown in figure 2.4b.

The diameter of the sample hole was chosen to be less than $50\mu m$ to minimize to risk of blow-out due to the instability described in ref. [8]: if any part of the sample happens to get outside the critical radius then the increase in load will cause the sample hole to migrate radially outwards without significant increase in pressure until it hits the boundary of the culet and hydrogen escapes. In the case of the laser heating experiment, which requires an absorber present in the sample chamber, this hole creep is even more grave: the sample thins out and the absorber loses its shape and position, potentially making further measurements infeasible. An example of such a problem is when the sample thins out and the absorber gets into the vicinity of the diamond surface, which acts as a thermal anchor. Thus it is important to keep the hole shape stable during a high pressure run. To improve the sample chamber stability against blow-out, there was no soft gold coating applied to gasket after indentation and prior to sample loading for all the successful high pressure runs. Previously gold was used to increase the amount of hydrogen trapped in the sample chamber by facilitating the chamber sealing at low load.

For laser heating experiments, since hydrogen is transparent, an absorber is embedded in the hydrogen; this is heated by the laser which heats the hydrogen in contact with its surface. A platinum disk with radius $10\mu m$ and thickness $1.5\mu m$ was used as the absorber. The diameter was chosen so the absorber stays smaller then the sample hole when reaching one megabar. By this pressure most of the hydrogen compression is done and the sample hole size does not change much. Each absorber had a center hole of diameter $2\mu m$ for planned transmission measurements, but in both otherwise successful runs the hole closed down before arriving at the pressure range of interest. In all of our runs, the DAC was cryogenically loaded to 30-40 GPa. It was at low temperature that the hole closed so we believe that it was due to deformation of the gasket rather than hydrogen diffusion. The absorber was cut from a foil using a focused gallium ion beam (FIB) with energy 30 keV and current 6 or 13 nA (Zeiss NVision 40

dual FIB-SEM system). The beam was programmed to first burn a center hole and then follow a circular path to cut out the disk. When the disk is cut it does not fall out from foil but is weakly bonded to it and can be easily extracted. A typical time to cut out one disk was 6 minutes. Given the large time overhead of foil mounting starting and aligning the FIB, we made batches of disks, ten at a time.

After the disks were cut out they were individually separated from the foil and moved to a stable platinum surface. To do it, mechanical micro manipulators were used with butane flame sharpened tungsten tips: there is no need in gripping or gluing, for electrostatic forces are strong enough to lift an absorber of this size. A typical needle had a taper of $\sim 10\ deg$ and tip radius of $\sim 5\ \mu m$.

For the first run, using the same micro manipulators, three ruby spheres were positioned on a disk to be used as standoffs from the diamond culet. These rubies were secured in place using FIB assisted deposition of platinum. The resulting absorber (with standoffs) and extra ruby spheres were transferred to the diamond anvil and secured by depositing 10 nm of Al_2O_3 by means of ALD. The deposition was carried out under the same conditions as for the second diffusion barriers layer on diamonds.

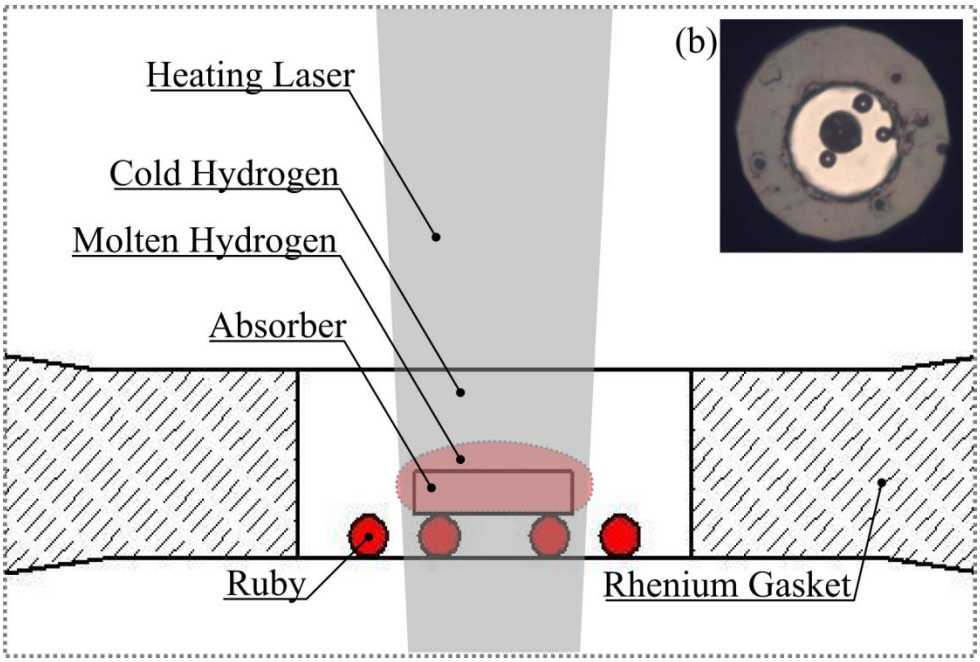

Figure 2.4: Sample chamber, scale drawing. The insert shows a photo of a sample cavity in the DAC ready for the loading.

For the second successful run, no ruby standoffs were used and no Al_2O_3 was applied to the absorber to make sure that the observed effect is not related to the alumina layer on the surface of the absorber. Instead the absorber was mounted using a thin (less than 100 nm) layer of silicon oil on its back surface which was not exposed to heating laser light and was not used for incandescent signal collection.

2.2.3 Mini chamber

There are two traditional ways of gas loading in high pressure: cryogenic loading, when the sample is loaded in the liquid or solid state and gas bomb loading, when room temperature gas is compressed to densities comparable to that of the liquid, which requires gas pressures of about 0.2 GPa. Both methods have their advantages and drawbacks; we use cryogenic loading.

To get to the condensation temperature of hydrogen a helium cryostat with two separate vacuum chambers was used: main compartment (OVC, outer vacuum chamber) and inner compartment (IVC, inner vacuum chamber), enabling the use of exchange gas cooling of the DAC in the IVC. This cryostat had optical windows in the cryostat tail so that the DAC could be observed during loading. The detailed cryostat construction is described elsewhere [9].

In order to minimize the amount of hydrogen gas used a separate chamber for liquid hydrogen was used; it is referred to as the mini chamber (MC). The total volume of MC is about 1cc. The main challenge for implementing the MC for our DAC is that the two diamonds should be capable of moving toward each other and a good seal is made. The implementation of the MC is shown in Fig. 2.3: a cylindrical stainless steel knife mounted on the same WC seat as one of the diamonds cuts into an indium metal cushion mounted on the opposing diamond WC seat. When the seal is made this small volume around the diamonds can be filled with liquid hydrogen through the capillary which is silver soldered through the knife.

Individual components of the MC – stainless steel knife (F) and hat (C) were attached to WC seats with ~100 μm layer of Lord 320/322 epoxy (not shown) which is thick enough to sustain thermal

cycling from room to helium temperatures: the thinner the layer is, more stressed it is under temperature cycling. If too thin the epoxy layer can't elastically absorb the mismatch of the thermal contraction of the knife and the WC seat and fails on thermal cycling. The indium cushion was melted on to the hat for every loading: the low melting point of indium (156.6 C) allows this without damaging the epoxy.

The knife needs to be designed according to the minimum pressure which is required by an experiment. Even though indium is relatively soft at helium temperatures, the load required to push the knife through it is higher at low temperature. As a result on warming of the DAC this extra load is released and is transferred to the sample, resulting in a pressure rise. The thicker the knife and deeper the penetration, the more pressure increases. In the design shown this pressure increase is about 30 GPa given 50 μm cold travel of the lower diamond.

2.2.4 Cryogenic loading

The cell loading procedure consisted of four major parts – cool down and temperature stabilization, condensing hydrogen into the MC, closing the DAC, and warm up. The most critical part is closing the cell, because the cell does not offer reversible diamond motion – it only pushes diamonds towards each other.

In order to monitor loading and the closing process we used white light interference: two closely spaced diamond flats make a Fabry Perot interferometer and the spectral transmission of this cavity can be used to calculate the diamond spacing. Specifically, in the case of low reflectivity of diamond faces, normal transmission of the cavity is:

$$T(\lambda) = \frac{1}{1 + Fsin^2(\frac{\delta}{2})} \sim 1 - Fsin^2\left(\frac{\delta}{2}\right) = 1 - Fsin^2\left(\frac{2\pi}{\lambda} nd\right)$$

where F is the coefficient of finesse [10], δ is a phase difference between each succeeding reflection for wavelength λ, given the index of refraction in cavity n and spacing d. Thus, if the spectral transmission is known, one can fit for nd. In our setup, which is shown in Fig. 2.5, the DAC was backlit with collimated white light, using a high brightness LED. The transmitted light was collected by the Wild microscope

objective and then part of it was refocused into an optical fiber input of a triplemate SPEX spectrometer equipped with thermoelectrically cooled Hamamatsu CCD. We used a 600 gr. /mm grating and the spectrum was collected around 700 nm so that observation of the ruby lines does not require rotating grating. Normally, with acquisition times of 300 ms there is plenty of signal through a 50 μm gasket hole. The spectrum was processed by a LabView program, which was written to fit for the strongest sine wave in the log of the spectrum (this turns multiplication into a sum and makes the amplitude of the sine nearly independent of wavelength). Each maximum can be indexed by its integral order, but the fitting routine did not assume zero phase at zero wave number which allowed for much easier implementation. Instead, the three parameter fit was used – frequency, phase and amplitude. Typical precision of the fit in determining diamond separation was better than 100 nm and accuracy we estimate as better than 1 μm. It was possible to observe live values for diamond separation (optical path), and the live change of phase of the wave. The latter is sensitive enough to tell if there is a vacuum or hydrogen gas in between the diamonds, but cannot measure the absolute value of the separation – only the slow change.

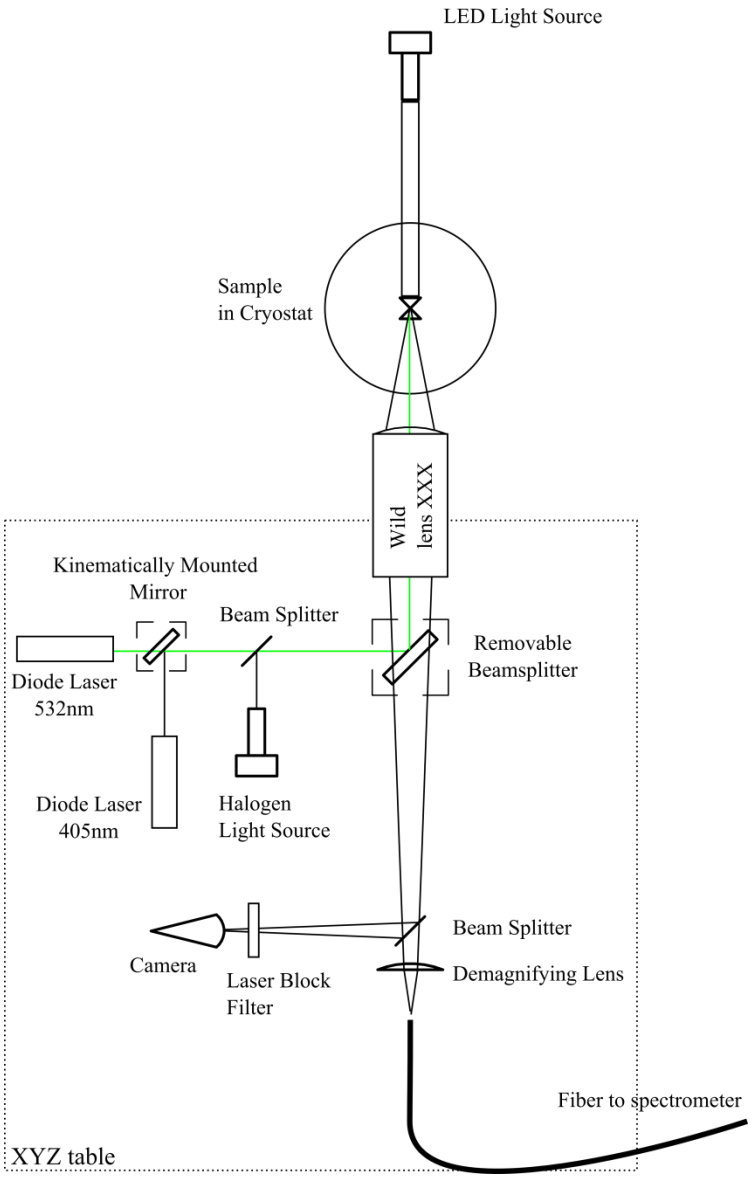

Figure 2.5: Hydrogen loading optical system

This system is used to detect when hydrogen is in the gasket hole: the refractive index of liquid hydrogen at ambient pressure is about 1.1. Therefore, if the real diamond separation is fixed, at the moment when the level of liquid hydrogen goes above the sample cavity, nd value suddenly changes up by 10% which is easily detectable. Alternatively, if at some point the nd value suddenly goes down by 10% without rotating the lead screw to advance the diamonds, it is interpreted as hydrogen level going below the sample chamber and sealing of the gasket should not be attempted until the hydrogen can be detected.

Other than white light spectrometry, the loading system included 532 and 405 nm 50 mW diode lasers to excite ruby fluorescence and a CMOS camera to visually monitor (and log) the sample loading. The cell temperature was controlled with Model 325 TI Lakeshore temperature controller. The load applied to sample was monitored with an Omega DP41-S strain gauge meter.

The detailed list of steps required to load the sample is described in the appendix.

2.2.5 Pressure measurement

The standard method of pressure determination in DAC was proposed by Piermarini et al [11]: one can embed a grain of ruby ($Al_2O_3:Cr^{3+}$) into the sample and monitor the position of the R1 fluorescence line, which experiences a red shift under pressure. Ruby is a good pressure sensor for its chemical stability and quality of the line. As such it the major method used in the high pressure field and was thoroughly studied for a broad range of pressures and temperatures. Syassen gives an in depth review of ruby under pressure in ref. [12]. For pressures exceeding one megabar using ruby becomes more difficult: first, the ruby fluorescence becomes weaker while overlapping diamond fluorescence goes up at the same time; second, the absorption bands of ruby experience significant blue shift thus requiring the use of a shorter wavelength laser, further increasing the fluorescent background coming from diamond. There are ways to overcome these difficulties, like mechanical chopping [13] (ruby has a very long lifetime of fluorescence ~1ms) or following the red line with a red tunable laser [14].

An alternative way to measure pressure which works well for pressures above one megabar or if the ruby signal becomes too weak or unobservable, is to measure a stress of the center of culet by means of Raman scattering on the $T_{2,\,g}$ phonon whose energy shifts with pressure [15]. It is not as accurate, because the whole body of the anvil is contributing to the signal whereas useful signal only comes from the very tip, but allows using lower laser radiation of lower energy. Furthermore, the calibration depends weakly on the diamond geometry [16].

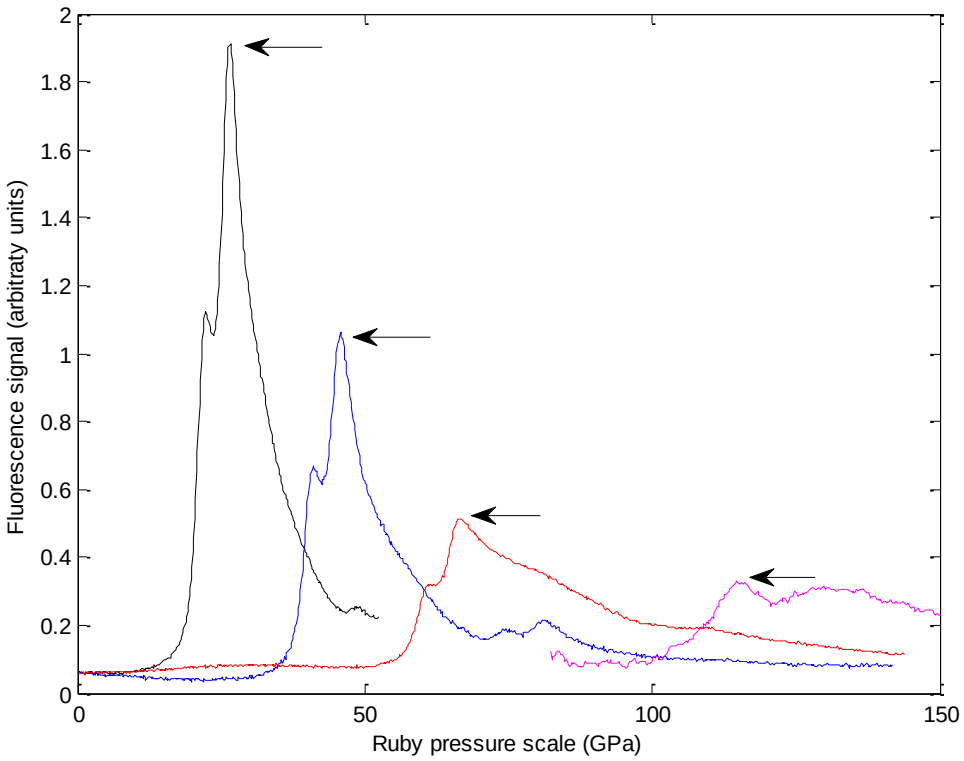

Figure 2.6: Typical ruby spectra plotted against ruby pressure scale P(λ). Y axis scaling is arbitrary. Broadening of the R1 line due to bridging can be observed. Arrows mark R1 line peaks.

We used both methods for pressure measurement. For the ruby fluorescence measurement, the beam of the argon ion (514.5 and 488 nm lines) or 405 nm diode laser was focused to a spot with a diameter of $\sim 30\,\mu m$ to excite a 5 μm diameter ruby ball [17] embedded in the sample. The power focused onto a ruby chip was estimated as 1 - 10 mW. The fluorescent light emitted by the ruby was collected at numerical aperture of 0.25 and focused onto the entrance slit of a Czerny-Turner grating spectrometer (Jobin-Yvon HR320, with 1200 $\frac{groove}{mm}$ 68-mm grating blazed at 500 nm in first order). Light was detected with an Andor iDus DU401A cooled CCD with a pixel size of 25μm. The system resolution was measured to be 0.16nm (full width at half height). A typical spectrum is shown in Fig. 2.6

For the pressure measurement using the diamond phonon, 1064 nm laser excitation was used. In fact the spectral data for diamond Raman was a byproduct when collecting the blackbody signal from the absorber: incandescent light was collected in the spectral region of ~900 to 1600 nm which includes the position of the diamond Raman Stokes peak at ~1250 nm. Then, as a part of data processing procedure,

linear with respect to laser power signal, including Raman, was separated from the incandescent blackbody signal in order to fit for temperature as described in the Data analysis (2.3.3) section of this chapter. Since total accumulation times for those measurements were large, of the order of several minutes, and heating laser power was high (>100 mW), the Raman spectra obtained had virtually no shot noise. A sample spectrum for pressure of 105 GPa is shown in Fig. 2.7: there is a clearly visible shoulder on the right of the main diamond Raman peak corresponding to signal from the culet. To measure the pressure the same routine as in ref. [15] was used: the relative position of the second minimum of derivative of the signal was taken as the value for the pressure induced shift.

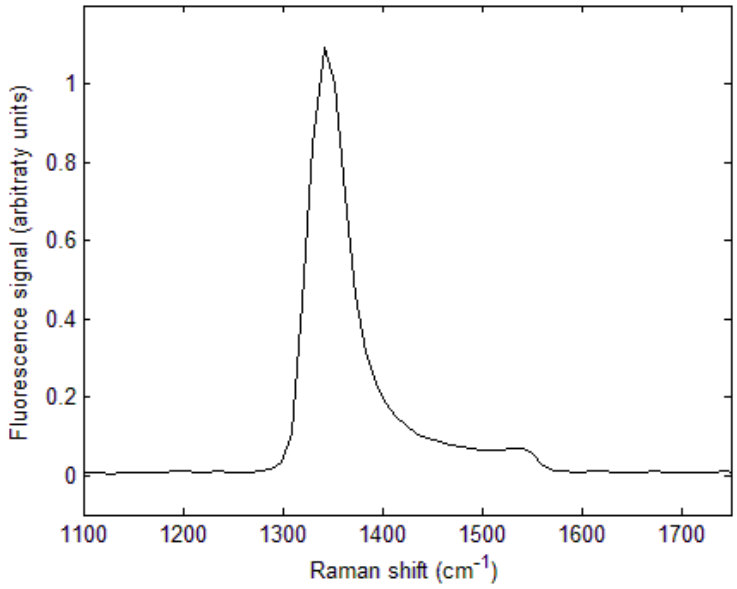

Figure 2.7: Diamond phonon Raman spectrum collected at 105 GPa. The strong peak in the spectrum is the scattering from the bulk of the diamond which is at lower stress than the culet.

The optical setup was the same as for the laser heating: the signal was collected from the diamond area immediately above the sample by a Schwarzschild objective with numerical aperture of 0.25, magnified by a factor of 11, then imaged onto a round spatial filter with diameter 200μm, de-magnified by a factor of 2, dispersed by a prism spectrometer and detected by a InGaAs diode array (Andor DU490A-1_7) with pixel width 25um. The spectral resolution of the system was 4nm (full width at half height). A detailed description of the setup is given the next section.

Comparison of the two methods shows that there is a small systematic discrepancy of the order of 5GPa (see Fig. 2.8). We attributed it to effects of size of the diamond culet on calibration: stress of the culet is not the direct measurement of the pressure in the sample chamber and the difference can weakly depend on the diamond geometry. Akahama used diamonds with the culet flat diameter of 35 μm. Since the observed discrepancy is relatively small we did not investigate it further.

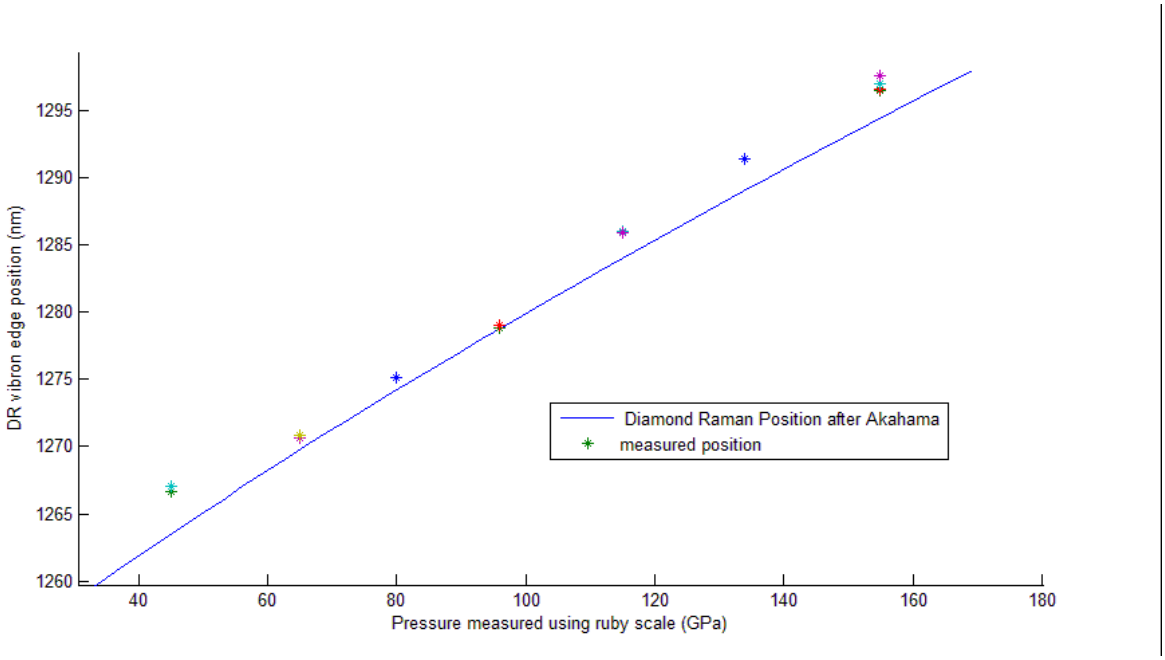

Figure 2.8: A comparison of pressures measured using the ruby scale and diamond Raman edge calibration by Akahama[15]

2.2.6 Laser heating and thermo reflectivity optical setup

The optical setup used for the hydrogen experiment is shown on Fig. 2.9. Light of 1064 nm pulsed Nd vanadate laser (Spectra Physics T40Y70 106Q) was expanded by a factor of 10 with a Gallilean beam expander and attenuated in two stages by a polarization rotator/polarizing cube beam splitter pair. The first stage polarization rotator was manually adjusted to set a maximum power and the second plate was rotated by means of computer controlled stepper motor. Usable stepper resolution was about 300 points from minimum to maximum power. After the attenuation stage, the beam was sampled with a 30% reflective dielectric beam splitter, passed through two alignment apertures and a computer

controlled shutter. Power of the sampled part of the beam was measured by a Gentech PS330WB power meter**.** To focus the light on the sample a 100 mm focal length (f/12) plano-convex lens mounted on motorized Oriel xyz stage was used. The same lens was used to focus the Argon Ion (Lexel model 95) laser on the sample, which joined the optical path at the second beam splitter cube.

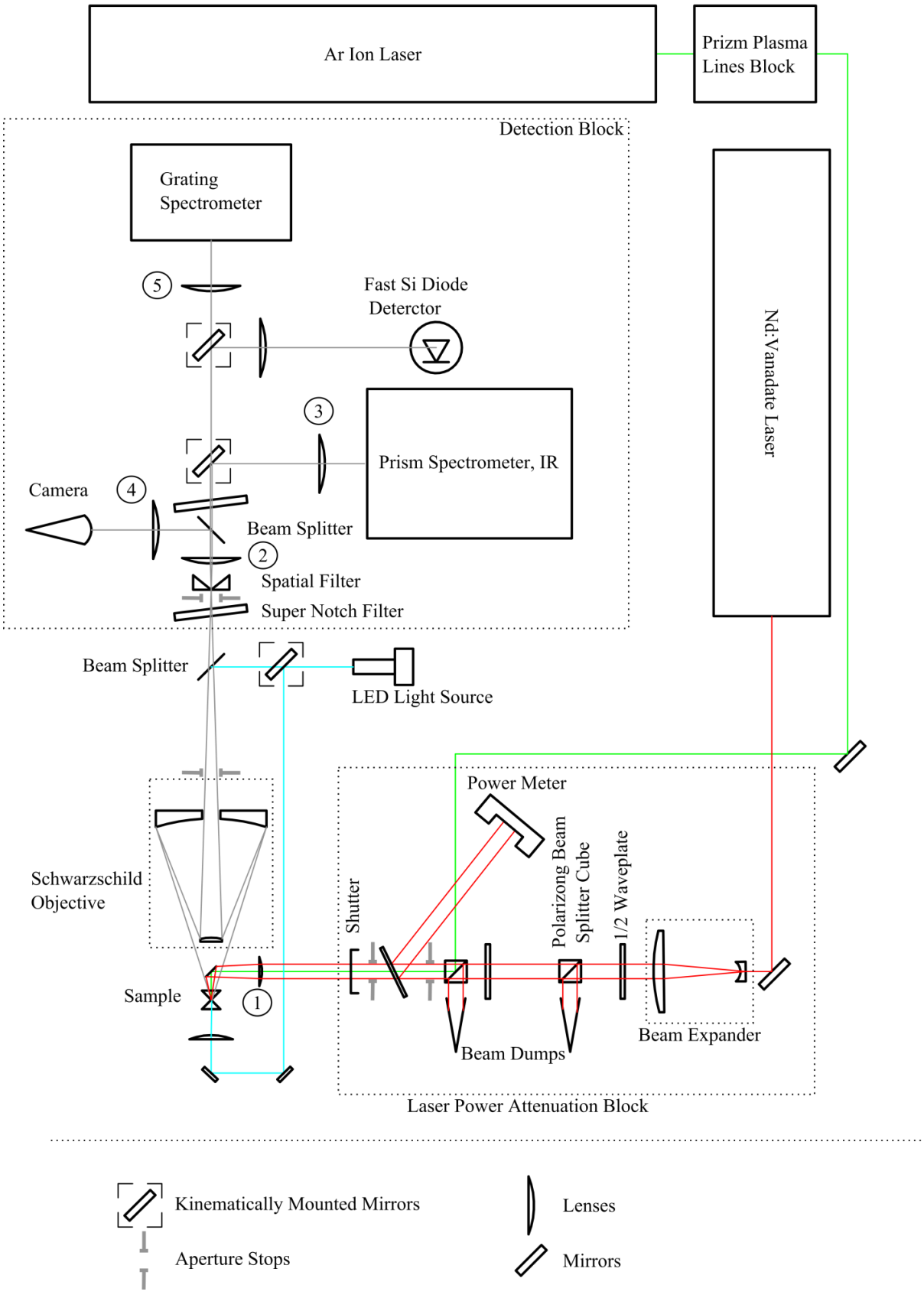

Figure 2.9: Laser heating optical setup, not to scale.

Light from the sample was collected with a custom built Schwarzschild objective (SO, 50 mm focal length, f/2, 130 mm working distance, magnification 11). By design the objective had an adjustment to compensate for spherical aberration introduced by the diamond anvil, as most commercial objectives do. The same objective was used to focus white light on the sample for visual observation in reflected light. Note that due to the presence of a small mirror in the SO this arrangement is essentially a dark field objective with respect to the laser illumination, which is important because it suppresses the amount of unwanted heating laser light falling into the detection system. Collected light was then passed though the first super-notch filter (Kaiser) and focused onto a kinematically mounted spatial filter, 200 μm diameter pinhole, which functioned as an entrance slit of the spectrometer downstream. After the pinhole the light was collimated by a 50 mm $CaFl_2$ lens. Eight percent of the light then was sampled by a pellicle beam splitter and directed onto a CMOS camera (Logitech Quickcam Pro 9000) to observe the sample. The rest passed though the second super notch filter and was directed by a kinematically mounted mirror into the 25 mm $CaFl_2$ lens, which imaged it onto slit plane of a prism spectrometer equipped with an InGaAs diode array sensitive out to 1.7 μm (Andor technologies, DU490A-1.7) The dispersing prism was chosen such that light from 900 to 1700 nm was imaged onto the diode array. The resolution of the spectrometer was limited by the diameter of the spatial filter, matched to the size of the absorber image, 4 pixels on the diode array. If the kinematic mirror was removed, light would be directed into grating spectrometer for ruby fluorescence pressure measurement or a fast Si diode based detector for thermoreflectance measurements. Amplified output of the fast detector was digitized by Tektronics TDS 2004B digital storage oscilloscope.

For illumination (back or front) a high power white LED was used (Luxeon Rebel, 1A current, ~1mm^2 emitting area) collimated by 30 mm f/2 lens. It is a very bright source which is flat and nearly Lambertian, and therefore is convenient for the microscopic illumination. The same setup was capable of accepting the light from the DAC mounted in the GM cryostat. The ~130 mm working distance of SO accommodates room temperature and low temperature studies.

The data acquisition system was partially automated. The diode array, the shutter and the motor rotating the quarter wavelength plate were controlled by the single script from the computer written in ANDOR Basic, the language specific to cameras manufactured by ANDOR instruments. The script communicated with the camera and ARDUINO USB board which provided physical input/output ports. One of the ports was used to control the shutter and two (direction, step) to communicate to EasyDriver step motor driver which generated stepping sequences for the motor windings. The laser power was manually entered in to the program after each half wave plate rotation. The factor limiting the measurement time in this setup was an unidentified instability in collection part of the system which led to a slow drift of the sample at the speeds of ~ up to 5 μm per hour.

To measure time (or temperature) dependence of the reflectivity of the absorber, the same optical path for the laser heating was used and both infrared and argon ion laser beams were operating at the same time. The reflected/diffused light was then folded after two super notch filters by means of a kinematically mounted mirror and directed towards fast Si diode based detector (New Focus Model 1801). The signal from the Si detector was recorded by a digital storage oscilloscope (Tektronix TDS 2004B) controlled by a computer and further processed in Matlab. In the optical setup only mirrors as opposed to band pass filters, were used. Thus only one detector could be used at a time – either thermoreflectance or pyrometry.

2.2.7 Transfer function measurement

In our experiments it is important to determine the true shape of the blackbody irradiance of a heated material. Since the optical system used to measure the spectrum distorts it, one needs to determine the transfer function, a function that accounts for the losses, chromatic aberrations, detector quantum efficiency, etc.

To measure the system transfer function, a resistively heated platinum radiator, a 50 μm thick foil disk about 1 mm diameter mounted on a K type thermocouple junction was placed in sample position and the spectrum of incandescent radiation was recorded. The resulting spectrum then was normalized by the

blackbody function with corresponding temperature and individual pixel bandwidth calculated as the derivative of the dispersion relation for the prism spectrometer.

$$\mathbb{TF}_i = S_i \left(\frac{C}{\lambda_i^4} \frac{BW_i}{e^{\frac{hc}{\lambda_i kT}} - 1} \right)^{-1}, \qquad i = 1 \dots 512 \tag{1}$$

where S_i is the signal at pixel number i in counts per second and C is a constant absorbing prefactor of Planck's formula, collection area and solid angle of collection. The transfer function was measured at ~800 K. Defined in this way, the transfer function absorbs the nontrivial wavelength dependence of platinum emissivity, quantum efficiency of the detector and individual pixel sensitivity variation [18]. The nominal difference from the work of Deemyad *et al* [18] is the presence of pixel bandwidth, which is defined as

$$BW_i = \lambda_{i+1} - \lambda_i, \qquad i = 1 \dots 511$$
$$BW_{512} = BW_{511} \tag{1.5}$$

where λ_i is the wavelength of light corresponding to the pixel number i. The specific value of BW does not have any effect on the measurement procedure because later, when calculating the photon flux density for an unknown temperature, the signal is in fact divided by bandwidth again and it cancels. The reason this definition was used is purely aesthetical: defined this way it is more similar to a traditional transfer function, which is just a percentage of the light going through the system.

2.2.8 Detector linearization and shuttering

The diode array response had to be linearized because it had shown saturation behavior before the maximum analog to digital converter(ADC) count was reached. This was accomplished by measuring same stable signal with varying exposures, 10 or 100 different exposures per series. The resulting data was used to determine the usable ADC count values (7 to 77% of full scale) and reconstruct a true linear counts from ADC reading within the interval. All the detector pixels showed similar universal behavior

near the saturation which was corrected. After the correction, the deviation from the linearity decreased from 300 to 40 counts.

The detector's dark current was subject to fluctuations despite controlled temperature. This put the limit on the time between background collection at ~ 5 minutes given the goal is to maintain accuracy of measurement better than 1 count per second Because of this a background frame was collected once per spectra with matching exposure with no exposure longer than 60 seconds. Additionally a region of the diode array was intentionally left as a control, meaning that under normal operation no counts should be observed. The control pixels were used to correct for offset caused by dark current fluctuations during a measurement. During each background frame collection the laser beam was blocked by automated shutter positioned after attenuation system so most of the laser light scattered off the beam dumps would be included in it.

2.2.9 History of Measurement Runs

Before the first successful run, which failed at 165 GPa, seven unsuccessful attempts were carried out as listed in Table 1 - runs history. Analysis of the failed attempts led to changes to the experimental system.

One of the problems being solved is hydrogen containment, i.e. how to protect diamonds from harmful diffusion of hydrogen. We started with the idea that keeping the diamonds at low temperature would be sufficient to keep the diffusion down – historically higher pressures were achieved with the low temperature approach, as described in the "Experimental history" (2.1.1) section of this chapter. The existing cryostats had too long of a working distances for efficient use of mirror optics. Therefore we decided to use a cryogen free cryostat based on a Gifford –McMahon type cooler. Additional advantage of using a cryogen free cryostat is that it should have better long term stability, because there is no moving level of the cryogen and there is no need for frequent cryogen transfers (refills). The very first test (run 1) showed that confinement of hot hydrogen is indeed possible; we estimate peak temperatures we got to as >2500 K by the fact that we were able to melt the platinum absorber embedded into the

hydrogen at a pressure of ~ 70 GPa without any harm to diamonds. However, the vibration caused by the operation of the cooler was prohibitively large and prevented us from collecting useful data. We redesigned the cryostat to mechanically decouple the DAC from the cooling head. The design of the new cryostat is described in the chapter 6. As the cryostat was rebuilt we were testing ways to increase the amount of hydrogen trapped in cavity by using two-stage compression (see appendix) and developing ways to fabricate the absorber assembly in a controllable and robust way. Exploring these two directions resulted in two more failed runs: run No 2 where the absorber was washed away by liquid hydrogen and run No 3 where the absorber was fixed to the diamond by FIB assisted deposition and a two-stage compression was used. In run No 3 the absorber stayed in place, but the two stage compression did not work, resulting in too little hydrogen being confined. We discarded the two-stage compression for run No 4 in which one diamond anvil failed catastrophically at a pressure that we estimate as <50PGa. We speculate that the cause of the failure was deep FIB damage to the diamond culet, which facilitated hydrogen diffusion. There are two pieces of indirect evidence suggesting this scenario: only the exposed-to-FIB diamond failed showing characteristic deep hydrogen cracks, and this happened on warm up. We decided to eliminate diamond exposure to FIB from that point on.

Table 1 - runs history

N	Date	Description
1	12/08..12/31/2009	Cryostat vibration prevented data acquisition (Pt black) P>70GPa
2	05/18/2010	Absorber fell off
3	06/23..07/12 2010	First FIB, pre compression chamber, not enough hydrogen trapped, 12 GPa
4	9/22/2011	Second FIB – Catastrophic diamond failure on warm up P~50GPa
5	12/1/2011	Blowout on warm up – suspected grain problems, 200um, P~50GPa
6	1/19/2012	Blowout on warm up – gasket was pushing against MC, P~50GPa
7	3/2/2012	Blowout on warm up – figured out gold, residual tilt, P~50GPa
8	4/1..5/28/2012	Data collected to 155 GPa
9	7/1..8/1/2012	Data collected to 125 GPa

By the time run No 4 was over, a new technique to guard diamonds against hydrogen diffusion was developed: a combination of diamond surface etching and a diffusion barrier coating as described above. The rebuilt GM cryostat with vibration suppression was ready as well, so we made a choice which

route to follow. We decided to postpone work in the direction of cryogenic containment and test how far in pressure/temperature can diamonds get with the help of the surface treatment. Another improvement was to substitute FIB assisted deposition, used to fix the absorber on an anvil, with a 10 nm thick layer of ALD alumina. ALD worked exceptionally well for securing ruby balls on the surface of an anvil – there were no rubies lost that otherwise could occur as liquid hydrogen flowed in during loading.

It took three more failed runs (No 5, 6 and 7) to fine-tune this new procedure. They all failed in the same way – a sample blowout on warm up. For these runs an existing liquid helium based cryostat was used for loading. To transfer the cell to the laser heating setup it had to be brought to the room temperature first. Due to the design of the mini chamber, based on the indium seal, there is an increase in pressure during the warm up of about 30 to 40 GPa. After a few such failures we guessed that the gold coating on the gasket was providing a slippery contact to the diamond anvil, facilitating blow out at a low pressure. The problem was solved by not depositing a gold layer on the gasket, which increases diamond to gasket friction. This was also confirmed by significant change in indentation behavior of gold coated gaskets: it takes about 20% less load to indent a gold plated rhenium gasket to a specific thickness compared to a similar bare gasket [See Fig. 2.10 – effect of gold on gasket indentation]. This figure shows three curves – two for bare rhenium gaskets of different thickness which converge to similar behavior as gaskets become thin and one for a gold plated gasket which yields more for the same load and exhibits a different thin regime behavior. We speculate that for thin gaskets friction is an important factor defining gasket compressive strength along with the shear strength of gasket material.

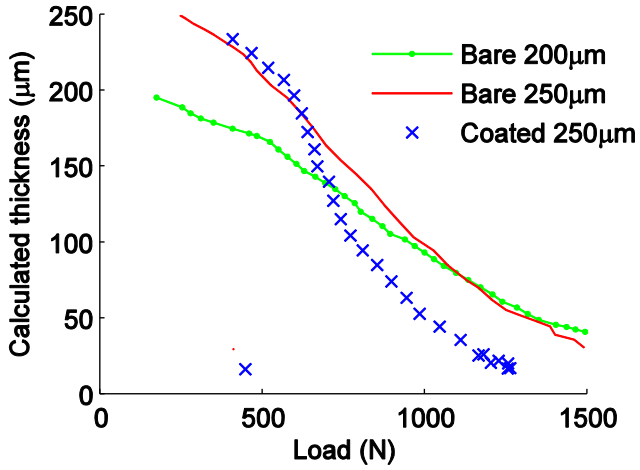

Figure 2.10: an example of indentation curves for bare and gold coated rhenium gasket blanks

The sealing did not appear to suffer from the absence of the gold layer, likely due to use of gold before the gasket indentation as described above. We speculate that this layer of gold was pushed into the rhenium surface where otherwise micro-cracks and terraces would occur (see Fig. 2.11 for an image of example of rhenium surface terraces due to slippage).

The diamond treatment approach eventually resulted in successful high pressure and temperature runs with no diamond failure. The first successful run (No 8) terminated at 165 GPa because of failure of tungsten carbide diamond support plate leading to catastrophic diamond cell failure. The second one (No 9) was terminated because while increasing the pressure above 125 GPa the absorber was substantially deformed by a ruby and we were not able to achieve uniform heating. Stress testing showed that the sample survived pulsed heating to about 2000K without damage to the diamonds anvils, but the transparency of the hydrogen sample gradually deteriorated, likely to due to formation of rhenium hydride. Diamonds failed during the release of the load, which is typical for runs above 1 megabar.

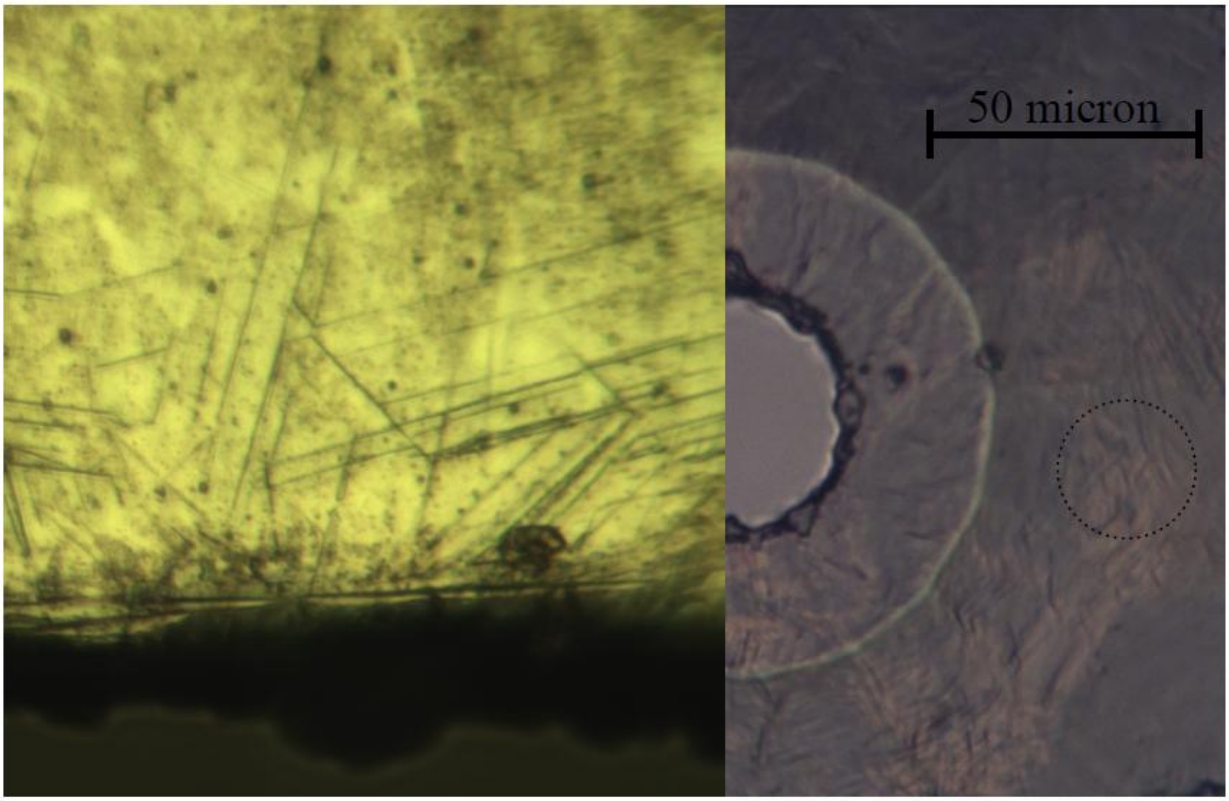

Figure 2.11. A microphotographs of rhenium plastic failure via slip bands. The left image shows a piece of rhenium cut by a shear, the defects can be clearly seen on the lower part of the image with lines forming angle of 120 degrees characteristic of hcp rhenium structure. The right image shows a preindented gasket: the slip bands are not as evident, but can be distinguished in, say, highlighted area. We believe that hydrogen escaping along these defects is responsible for the increased load required to seal liquid hydrogen in a bare rhenium gasket compared to sealing in a gold plated gasket.

2.2.10 Bibliography

[1] A. V. Valkenburg, "Visual Observations of High Pressure Transitions," *Rev. Sci. Instrum.33, 1462,* 1962.

[2] P. Bridgman, Physics of high pressure, New York: Dover Publications, 1971.

[3] M. Eremets, High Pressure Experimental Methods, Oxford Science Publication , 1996.

[4] A. Jayaraman, "Diamond anvil cell and high-pressure physical investigations," *Rev. Mod. Phys.,* vol.

55, no. 1, 1983.

[5] W. A. Bassett, "Diamond Anvil Cell, 50th Birthday," *High Pressure Research,* vol. 29, no. 2, pp. 163-186, 2009.

[6] W. Moss, "US4776223".

[7] E. Zarechnaya and I. Silvera, "to be published".

[8] J. Orloff, C. Narayana and A. L. Ruoff, "Use of focused ion beams for making tiny sample holes in gaskets for diamond anvil cells," *Rev. Sci. Instrum. 71, 216,* 2000.

[9] I. Silvera and R. Wijngaarden., "Diamond anvil cell and cryostat for lowtemperature optical studies," *Rev. Sci. Instrum.,* vol. 56, no. 121, 1985.

[10] S. Lipson, H. Lipson and D. Tannhauser, Optical Physics (3rd ed.), London: Cambridge U.P, 1995.

[11] G. Piermarini, S. Block, J. Barnett and R. Forman, "Calibration of the pressure dependence of the R1 ruby fluorescence line to 195 kbar," *J Appl Phys ,* vol. 46, no. 6, 1975.

[12] K. Syassen, "Ruby under pressure," *High Pressure Research ,* vol. Vol. 28, no. Iss. 2, 2008.

[13] J. H. Eggert, K. A. Goettel and I. F. Silvera, "Elimination of pressure-induced fluorescence in diamond anvils," *Appl. Phys. Lett,* vol. 53, no. 25, 1988.

[14] N. Chen and I. Silvera, "Excitation of ruby fluorescence at multimegabar pressures," *Rev. Sci. Instrum.,* vol. 67, no. 4275, 1996.

[15] K. Akahama, "Pressure calibration of diamond anvil Raman gauge to 310 GPa," *J. Appl. Phys. 100, 043516,* 2006.

[16] B. J. Baer, M. E. Chang and a. W. J. Evans, "Raman shift of stressed diamond anvils: Pressure calibration and culet geometry dependence," *J. Appl. Phys,* vol. 104, no. 3, 2008.

[17] Chervin et al., "Ruby-spheres as pressure gauge for optically transparent high pressure cells," *High Pressure Research,* vol. 21, pp. 305-314, 2001.

[18] S. Deemyad, A. N. Papathanassiou and I. F. Silvera, "Strategy and enhanced temperature determination in a laser heated diamond anvil cell," *Journal of Applied Physics,* vol. 105, pp. 093543--093543, 2009.

2.3 Pulsed laser heating and pyrometry

Laser heating in a diamond anvil cell significantly expanded the range of physical conditions attainable in a laboratory, and is a technique responsible for knowledge about most high pressure melting phenomena. Laser heating takes advantage of diamond transparency for radiation and it allows local high temperature conditions in the sample region while keeping the body of the cell at reasonably low temperatures. Typical problems are chemical reactions between the sample and diamond anvils or auxiliary materials, difficulties in temperature determination and, in case of melting studies, identifying the melting transition is not always straightforward (see *Platinum surface reconstruction upon pulsed laser heating* chapter).

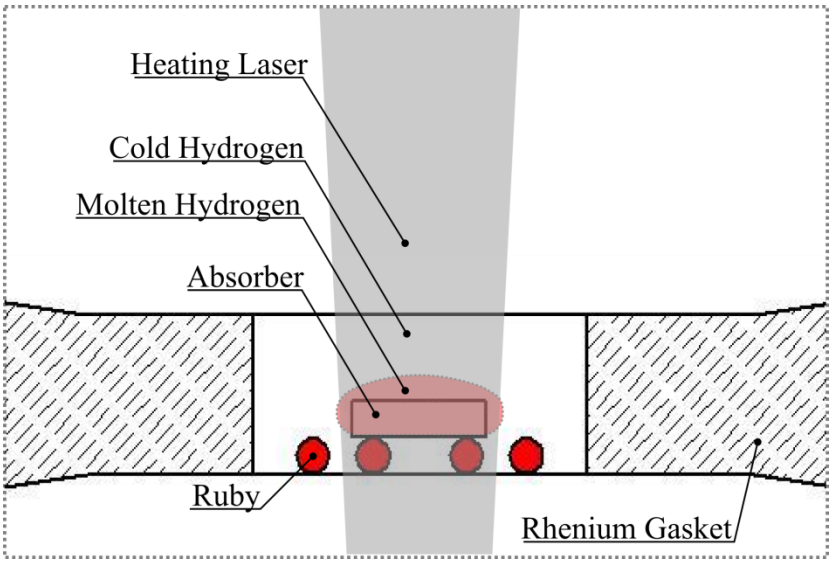

Figure 2.12: Schematic geometry of the experiment.

In case of a hydrogen sample, which is very reactive and diffusive, these problems can be partially mitigated by using pulsed laser heating to further decrease the hot zone size. For example, for CW laser heating the power dissipated in the sample/cell is of order 50 Watts, whereas in pulsed heating 1 milliJoule in 100 nanoseconds can dissipate 10 kWatts, locally. The heating is localized to the sample and the thermal excursions are very short so that there is little time for diffusion or thermally activated chemical reactions. Thus, pulsed laser heating can enable localized higher temperatures compared to static laser heating, at the expense of uniformity, both temporal and spatial. In pulsed laser heating we are

interested in the peak temperature during the pulse. There are two ways of determining this: time resolved spectroscopy using a gated detector to measure the temperature at each interval in the pulse, or time averaged spectroscopy, in which the average spectral irradiance is measured with a continuous detector and the peak temperature is extracted by analysis. We use the latter approach. The possibility of reliable temperature determination using time unresolved pyrometry was demonstrated experimentally in a series of works by Rekhi et al [1], Deemyad et al [2], Deemyad and Silvera [3] and Deemyad , Papathanassiou, and Silvera [4]. Interpretation of the results, after the peak temperature is known, is not straightforward and is a source of controversy; the most recent theoretical papers on the subject are Geballe and Jeanloz [5] and Montoya and Goncharov [6]. In this chapter this approach will be reviewed, with some original contributions regarding the estimation of the peak temperature, given time averaged incandescent spectra.

The basic idea behind the laser heating experiment is that if one can measure the peak temperature of the sample as a function of incoming laser pulse energy, then this dependence will be sensitive to phase transitions in the sample which can abruptly change reflectivity, heat conductivity or have significant latent heat. Fig. 2.12 schematically shows the geometry for a typical laser heating in our experiment. A pulsed IR laser is focused on the absorber and infrared radiation emitted by the absorber is collected by the optical system, to be analyzed. To keep the potentially hot absorber back side away from the diamond anvil surface, ruby balls were used as standoffs in one of the two successful runs.

2.3.1 Temperature measurement and Planckian averages

In this section we describe the procedure used to reconstruct an absolute value of the peak temperature of a metallic absorber given the time averaged spectrum of incandescent light emitted by it and the information about the shape of the temporal temperature profile. In general, the time for local thermalization is tens of picoseconds, while our heat pulses are hundreds of nanoseconds, so that the system is in local thermal equilibrium. In this case it is important to determine the peak temperature due to a laser pulse when determining the temperature of a phase change, such as melting.

The information about the temperature pulse shape can be obtained either by using finite element modeling of heat transfer in the cell or experimentally, by measuring the time dependent reflectivity of the metal surface by assuming

$$\epsilon(T) - \epsilon(T_0) \sim A\,(T - T_0) \tag{2.3.1}$$

where ϵ is emissivity and A is a proportionality constant, which holds for platinum at ambient conditions. The temperature estimated in this way (up to an unknown multiplier) is referred to as the thermoreflectance temperature. It is notan accurate measurement of the temperature profile, but rather an estimate. The fact that platinum emissivity in the visible, at least at ambient conditions is a good linear function of the temperature up to melting (refs. [7], [8]) adds confidence to this estimation. Our analysis (ahead) shows that the temperature determination in the region of interest is only weakly affected by the specific shape of the pulse. We do not distinguish between reflectivity and emissivity variations because optically thick, non transparent absorbers are used in our experiments. In the absence of transmission, reflectivity and emissivity sum to unity because of conservation of energy.

The instantaneous spectral radiance $\mathbb{F}_\lambda$ (watt per steradian per area per unit of wavelength), of the absorber at temperature T and wavelength λ can be approximated by Planck's law with varying emissivity:

$$\mathbb{F}_\lambda d\lambda = \frac{2hc^2}{\lambda^5} \frac{1}{e^{\frac{hc}{\lambda k_B T}} - 1}\ \epsilon(\lambda, T) d\lambda \tag{2.3.2}$$

where h is Planck's constant, c the speed of light, k_B is the Boltzmann constant and $\epsilon(\lambda, T)$ is the emissivity of the absorber, which accounts for deviations of the radiance from ideal blackbody behavior. Emissivity and a related property emittance (which is a name used for surface roughness or shape dependent emissivity) for pure platinum are weakly dependent on temperature, surface grain structure, pressure, and even surface gas interface [8], etc. Works of Deemyad and Silvera [9], Madjid et al [8] and Aksyutov [10] suggest that the temperature dependence $\epsilon(\lambda, T)$ is rather weak compared to the exponential term in Eq. 2.3.2 outside the T- λ range of our measurements (which is 1000 to 2000 K and

1.3 to 1.8 μm) which justifies the use of the emissivity concept. Furthermore, we performed additional work on platinum melting (See *Platinum surface reconstruction upon pulsed laser heating* chapter) which suggests that emissivity of Pt is indeed well-behaved and an accurate value of the platinum melting temperature was measured.

The radiation can be spectrally dispersed and then the time averaged intensity can be measured as a function of wavelength. The resulting photon flux (photons per second) at a detector can be described as:

$$S(\lambda) = C\ \mathbb{TF}(\lambda)\frac{1}{h\nu}\frac{1}{\Delta t}\int_0^{\Delta t}\mathbb{F}_\lambda\big(T(t)\big)dt \tag{2.3.3}$$

where Δt is the measurement or integration time, $\mathbb{TF}(\lambda)$ is the system transfer function, that is the percentage of the light emitted at the absorber that gets to the detector for the specific wavelength, C is a geometric factor which is a product of the absorber area and the effective solid angle of light collection accounting for the cosine angular distribution of original light intensity. To convert this flux to counts two more factors are needed – detector quantum efficiency and an individual pixel bandwidth defined by the spectrometer dispersion curve, both being wavelength dependent, but not important for the present analysis. The system transfer function measurement was described in the "*Experimental method" (2.2)* section of this chapter.

The idea, simplifying the measurement, published by Deemyad et al [4] is to approximate emissivity by its low temperature value, pull it outside from under the integration and absorb it into the transfer function. This introduces some error into the temperature determination, but, as mentioned above, given measured emissivity and successful temperature determination on the melting of platinum, the error is believed to be small. The benefit is that the measurements of the system transfer function, detector response and absorber emissivity can be combined into one step, removing potential errors due to extra steps and a need of a calibrated spectral source. In case the data on temperature dependence of platinum spectral emissivity will become available, it can be incorporated into the existing analysis (at the stage of

calculating the relationship between the peak temperature and time averaged temperature, details below) without much effort.

It is important that in the limit $\frac{hc}{\lambda kT} >> 1$, where the measurements are performed and which corresponds to photon energy larger than the temperature of interest, the dependence $\mathbb{F}_\lambda(T)$ is a steep exponential. Applied to the situation where the sample is heated by a laser pulse, it means that the largest contribution to $S(\lambda)$ comes from the time when the absorber is the hottest and the colder tail has less of an effect. This can be demonstrated by Taylor expanding $-\frac{1}{T(t)}$ in the exponent of Eq. 2.3.2 around its maximum up to second order and integrating across a single pulse (all the temperature independent factors are omitted for clarity):

$$\int \frac{dt}{e^{\frac{hc}{\lambda kT}} - 1} \sim \int \exp\left(-\frac{C_2}{\lambda T(t)}\right) dt \sim \int \exp\left(-\frac{C_2}{\lambda}\left(\frac{1}{T_{peak}} + \frac{T``}{{T_{peak}}^2} t^2\right)\right) dt$$
$$= \left(\frac{\pi \lambda {T_{peak}}^2}{T``C_2}\right)^{1/2} \exp\left(-\frac{C_2}{\lambda T_{peak}}\right) \tag{2.3.4}$$

The approximation by Taylor expansion apparently works best for low temperatures and short wavelengths where the exponential dependence is steep. In this case, the resulting spectrum $S(\lambda)$ has a clear dependence on the peak temperature which can be in principle extracted by fitting.

Another limiting case of long wavelength is illustrative as well. If one tries to carry out the integration in the region $\frac{hc}{\lambda kT} \ll 1$, it is easy to see that the integrated spectrum does not have a strong dependence on the peak temperature, but rather it yields the average temperature:

$$\frac{1}{\Delta t}\int \frac{dt}{e^{\frac{hc}{\lambda kT}} - 1} \sim \frac{1}{\Delta t}\int \frac{\lambda kT}{hc} dt = \frac{\lambda k < T >}{hc} \tag{2.3.5}$$

This is beneficial for constant temperature pyrometry and is in fact the range used for infrared thermometers and imagers, because it allows usage of a detector with small dynamic range to cover a large range of temperatures. However, determining the peak temperature using this information is not practical in case of pulsed heating, because the result is affected by overall change of signal strength due to, say, varying thermal conductivity of the sample (to changes in geometry) or ill-defined area of the absorber and there is no way to discriminate variations in these parameters from variation in temperature.

Generally, in the case of pulsed laser heating the spectral irradiance is fit to some functional form and the resulting temperature is called the Planckian temperature, T_{planck} after [1]. We will consider two subcases – fitting to the Wien's approximation of the Planck law and to the form of Eq. 2.3.4, which differs from Wien's approximation by the $\lambda^{1/2}$ factor and will be referred to as the Laplace approximation:

$$S(\lambda, T) \sim \epsilon \exp\left(-\frac{C_2}{\lambda T}\right) \lambda^{-4+a} \tag{2.3.6}$$

$a = 0, \frac{1}{2}$ for Wien and Laplace parameterizations, respectively.

The choice of these two parameterizations is somewhat arbitrary. A reason to consider the Wien approximation is that it has a straightforward physical meaning of approximating the observed time averaged radiation spectrum of a sample heated by the pulsed laser with the black body spectrum of some unknown temperature. Plus, this approximation was used in earlier works [4] [2] [1]. The reason to consider the Laplace approximation is in the limit of low λT and Gaussian pulses it becomes a precise relationship rather than an approximation, as can be seen from Eq. 2.3.4 and will be confirmed by numerical analysis.

The temperatures resulting from the fits T_{planck} will be referred to as **Wien** and **Laplace (aggregate) temperatures**. In both cases the value of fitted temperature does not have to match T_{peak}, the actual maximum value of $T(t)$. The procedure of calculating T_{planck} for a given $T(t)$ is similar to

taking a (weird) *average* value of the temperature pulse. This analogy is the most straightforward for the case of Wien fit, because:

- the inferred temperature is always less than the maximum value of the temperature pulse.
- for the special case when the sample temperature is a constant, fitting to the Wien approximation will yield that temperature[2] as any proper average would do.

In the case of the Laplace fit it is not clear if the fit has to be lower than the maximum, but for all the simulations it was. A final clarifying note: both Wien and Laplace temperatures are specific cases of Planckian temperature. The names are assigned to indicate what functions the irradiance is fitted to.

The goal of the further analysis is to relate T_{planck} and T_{peak} for different fitting procedures and real T(t) pulse shapes. From the Eq. 2.3.4 it should be clear that the best agreement between the aggregate and true temperatures is achieved when the exponent $\frac{hc}{\lambda kT}$ is large or when the shape of the T(t) is parabolic.

To relate the true peak temperature and the Planckian temperature for Wien and Laplace aggregates, the numeric modeling was used with a number of temperature profiles. The way the Planckian aggregate is defined, the functional relation between the aggregate for a given fitting procedure and the peak temperature of a pulse is unique for a given temperature pulse shape. Since we strictly speaking do not know the shape of the temperature pulse we can try to estimate what is the uncertainty on the peak temperature, when the pulse shape changes. The candidate pulse shapes were measured thermoreflectance curve from Eq. 2.3.1 and a set of curves generated by COMSOL finite element analysis software package using the measured laser pulse temporal profile and realistic thermodynamic properties of the cell materials. Time-dependent temperature pulses $T(t)$ characterized by a specific value of the peak

[2] a bit different in fact, due to the sacrificed -1 in the denominator of the Planck law, but this is a minor change for the region of interest

temperature were used to generate time averaged incandescent spectra $\widetilde{S}$, performing integration of Eq. 2.3.3 assuming temperature independent emissivity

$$\tilde{S}\left(\lambda,\, T_{peak}\right) = A(\lambda)\,\frac{1}{\Delta t}\int_{0}^{\Delta t}\frac{dt}{e^{\frac{hc}{\lambda k T(t)}}-1}\,dt \tag{2.3.7}$$

where $A(\lambda)$ absorbed all the wavelength dependent factors. The resulting spectra with different values of peak temperature were fitted to Wien and Laplace forms:

$$T_{planck} = \underset{T,\epsilon}{\operatorname{argmin}}\left(\left\| \frac{\tilde{S}\left(\lambda,\, T_{peak}\right)}{A(\lambda)} - \epsilon \exp\left(-\frac{hc}{\lambda k T_{planck}}\right)\lambda^{a}\right\|\right) \tag{2.3.8}$$

$a = 0, \frac{1}{2}$ for Wien and Laplace parameterizations, respectively.

To perform the fit, linear regression can be used to fit $\log\left(\frac{\tilde{S}\left(\lambda.\, T_{peak}\right)}{A(\lambda)}\lambda^{-a}\right)$ versus $\frac{1}{\lambda}$. Disregarding '-1' in the denominator of Eq. 2.3.2 does not lead to error, since the exponent is essentially a way to analytically parameterize $\tilde{S}$, however it makes a small ($\delta T = 20$ K at $T_{peak} = 2000$ K) contribution to the correction discussed below.

The resulting relationship between T_{peak} and T_{planck} was used to produce a table correlating the real peak temperature and the result of fitting, the Planckian temperature. This work is similar to the work of Rekhi et al [1]. A difference is that we considered the sample geometry specific to the DAC as opposed to a semi infinite half space filled with metal. We also tried to examine the effect of varying thermal conductivity of hydrogen on the results due to lack of information about it, and the effect of using different spectral regions, corresponding to different available detectors. The last difference is that we introduce and justify the use of the Laplace approximation which approximates the measured spectra much better and in fact turns into the exact relationship in the region of low λT.

The results of this study agree qualitatively with the intuitive picture. The discrepancy (or correction) $\delta T = T_{peak} - T_{plankian}$ increases with the increase of temperature, and with increased wavelength as expected from the analysis of Eq. 2.3.4.

Increasing the thermal conductivity of hydrogen makes the temperature pulse sharper and more symmetric (up to a certain limit), thereby decreasing the correction. However, if the conductivity is such that the time constant of the cell is shorter than the typical rise time of the laser pulse, the temperature profile essentially repeats the laser pulse shape and a further increase of the conductivity does not affect the temperature pulse shape and therefore averaging.

Figure 2.13 shows comparison of $\delta T \; vs \; T_{peak}$ dependencies for Wien and Laplace aggregates for different FEA models used: model of the cell with nominal hydrogen thermal conductivity (conductivity k=10), thermal conductivity increased by a factor of 10 (conductivity k=100), and a cell model with an intermediate hydrogen thermal conductivity, but using a Gaussian laser pulse shape rather than the one measured. The important difference between the Gaussian pulse and the real laser pulse shape is the presence of a tail in the real laser pulse (see Fig. 2.14, insert) which leads to slower temperature decay and can increase the δT. Additionally plotted is a curve which used the thermoreflectance data as the information about the temperature profile during a heating cycle. Figures 2.13c and 2.13d show the result of varying the wavelength range over which the fitting is done with three intervals of interest –near infrared (700 to 900 nm), accessible by conventional CCD cameras, 1.5 to 1.8 μm covered by InGaAs diode array, and 2 to 3 μm used by Deemyad et al and detected by an InSb detector. The thermoreflectance temperature pulse shape was used to generate these curves. An interesting observation from this is that the results for the melting line of hydrogen of Deemyad et al should be shifted up in temperature by ~60 K, since they used the correction computed for the visible region in their work.

An immediate conclusion from looking at Figure 2.13 is that varying the temperature pulse shape translates to modest variation of the correction. The case of nominal thermal conductivity of hydrogen can

be excluded because the temperature pulse generated by the FEA for this value of thermal conductivity is clearly different from the observed evolution of the time resolved reflectivity (Fig. 2.14). It is shown, however to illustrate that a strong error in the shape of the pulse would only result in an error of the order of 100 K at 1800 K, which is the spread between the curves in Fig. 2.13 upper row.

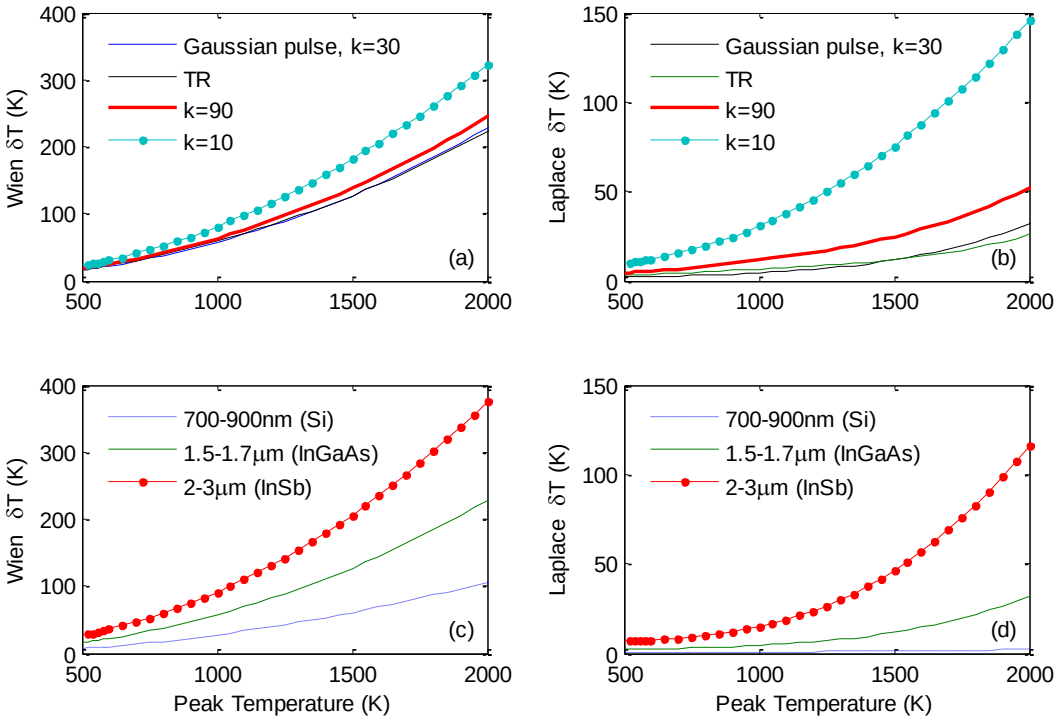

Figure 2.13: *δT*, deviations of the peak temperature from Wien (left) and Laplace (right) aggregates. The upper row demonstrates the effect of different temperature pulse shapes on the *δT* with specific details discussed in text. The bottom row shows the effect of using different spectral ranges to perform the fit. TR stands for thermoreflectance, k for the model hydrogen thermal conductivity. The Gaussian pulse, as described in the text, is a simulation where the laser pulse had a Gaussian temporal profile without the long tail of the real pulse.

As expected, the aggregates can be used for peak temperature estimation. Namely, in this work, when applied to real data on hydrogen both methods resulted in similar results. Wien and Laplace fits after correcting by the corresponding *δT*, based on thermoreflectance T(t), yielded less than 20 K difference, which is less than other sources of error. In the more general case, where thermoreflectance data is not available, using the Laplace averaging is probably more desirable because it fits the spectra

better. An interesting observation is that both fits have very similar sensitivity to temperature pulse shape variations. The temperature pulse shape needs to be determined independently which might be problematic with FEA simulations due to lack of knowledge about thermodynamic properties of materials at these conditions. An illustration of the lack of knowledge about the subject are two publications from the same group [6] and [11] where values of 5 and 65 W/(mK) are used for thermal conductivity of hydrogen under the same conditions. In the case of our FEA model this problem occurred as well: the FEA predicted temperature pulse tail did not agree with the thermoreflectance data at the tail of the pulse for any value of hydrogen thermal conductivity. The most likely cause of this is the use of a 1D FEA model as opposed the more realistic 3D geometry where the temperatue decay will be faster in the tail, once lateral heat transfer becomes important. We did not investigate this matter thoroughly because of the potential error in the temperature determination would be smaller than other sources of errors.

Figure 2.14 shows comparison of the temperature profiles for thermo reflectance and results of the FEA model with different inputs – Gaussian laser pulse shape and models with the measured laser pulse shape and different values of hydrogen thermal conductivity (10 and 99 W/mK). The insert shows the measured laser pulse shape with the tail which does not appear on thermoreflectance data indicating that the platinum reflectivity may vary more strongly with temperature at elevated temperatures. As can be seen from Figure 2.13 this uncertainty may result in temperature determination error of ~ 25 K.

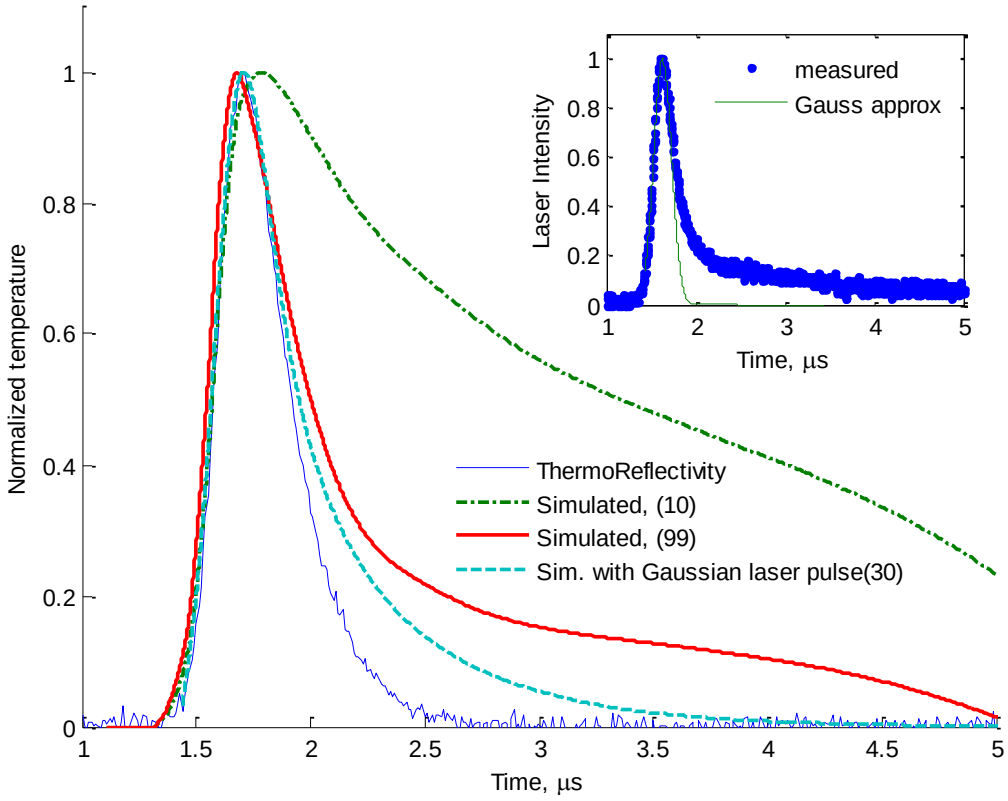

Figure 2.14: Comparison of FEA based and Thermoreflectance temperature profiles. Values in parenthesis are the model hydrogen thermal conductivity in W/mK. Inset shows the measured laser pulse intensity profile along with its Gaussian approximation.

2.3.2 Data analysis

We chose to use an InGaAs diode array as the detector sensitive to radiation with wavelength in the range 1 to 1.8 μm. Compared to conventional visible detectors, this provides significant improvement in signal, especially at lower temperatures. For example, when doubling the wavelength from 900 to 1800 nm, the blackbody signal increases ~200 times if the radiating object has a temperature of 1000 K and ~35000 times at 600 K. When going further in wavelength this advantage is compromised by decreasing discrimination ability of the temperature pulse averaging resulting in larger differences between Plankian aggregates and corresponding uncertainties and the increasing noise of room temperature radiation background, the so called background limited photo detection (BLIP).

The detector choice introduces one problem which is not present in the case of silicon based detectors: the energy of the heating laser photons becomes larger than the BB radiation in the detection range, resulting in fluorescence and Raman scattering signals overlapping the detection spectral region. Both Raman and fluorescence signals intensities are fairly linear with respect to the intensity of the excitation laser; this allows separating them from the incandescent signal whose intensity is highly nonlinear with respect to laser power. This will be discussed in more detail.

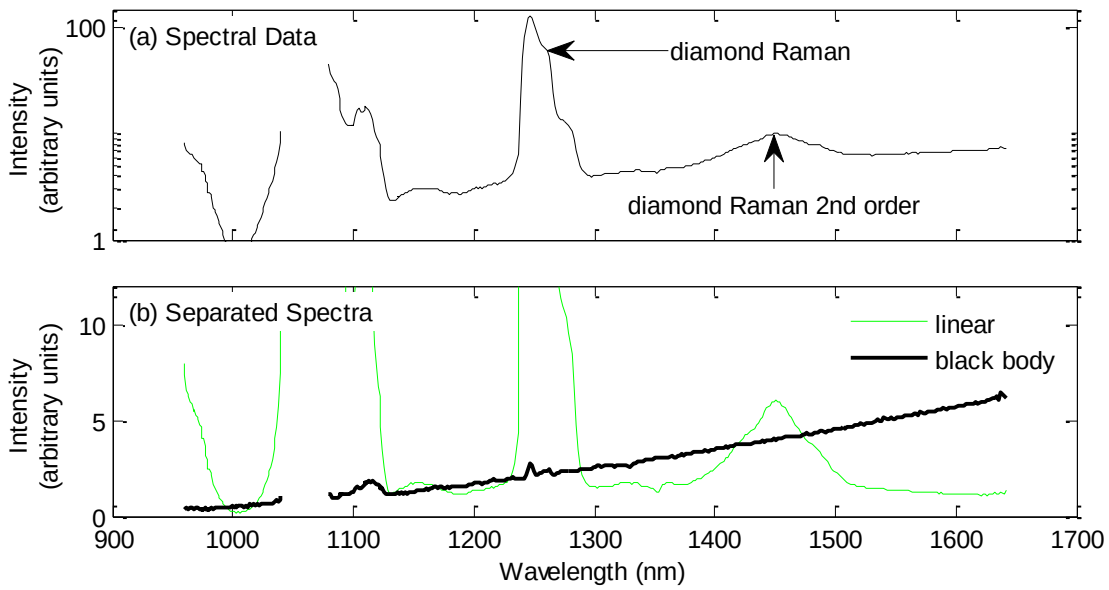

Figure 2.15: The spectral corrected by the spectral transfer function during heating and separation of the BB component from the background. The peak temperature was estimated as 1440 K.

Figure 2.3.4a shows a typical low resolution spectrum collected from a laser heated sample divided by the system transfer function. The features include: (a) heating laser spectrum at ~1064 nm, (b) parasitic lines from the heating laser gain media around 900 nm and 1100 nm, (c) strong diamond Raman signal at 1230…1295 nm with a low energy shoulder due to the stressed culet region, (d) second order diamond Raman band at 1400..1500 nm, (e) broad band alumina and diamond fluorescence in the 1100 to 1600 nm region (hard to see, but it is there), (f) and finally, the overall positive slope is due to the Planckian incandescent signal for the temperature ~1440 K. The signals (a) to (e) will be referred to as linear background and (f) as blackbody or the incandescent signal. Figure 2.15b shows the result of separating the linear and blackbody parts of the signal. The separation is not perfect – the blackbody curve is not completely smooth, but note that the residuals of diamond Raman peak at 1248 nm has an amplitude 0.5 while the peak itself has an amplitude of 128, which provides an estimate of the quality of the separation.

Our objective is to determine the BB radiation signal as a function of wavelength, and then fit this to determine the temperature. The various contributions to the curve in Fig. 2.15a indicate that this will be

quite challenging, but successful as demonstrated in Fig. 2.15. We developed a successful procedure for separating out the BB signal from the other contributions and this will now be described in detail.

The dependence of the peak temperature on the heating laser power will be referred as a heating curve. For every pressure several heating curves were measured as. The raw data used to produce an individual heating curve consisted of a series of pairs {average laser power, spectrum collected}; the InGaAs detector had 512 pixels; the average laser power was measured with an power meter. To separate the incandescent signal from the linear signal, the following model was assumed for the signal *I*:

$$I_i = c_i + \alpha_i \tilde{P}(P) + BB_i(T_{planck}(P)), i = 1..512 \tag{2.3.9}$$

where i enumerates pixels, c_i is a 'persistent background', α_i is a spectrum of the 'linear background', $\tilde{P}(P)$ is some function of laser power and $BB_i(T_{planck}(P))$ is an incandescent signal

$$BB_i(T_{planck}(P)) = Tf_i \epsilon(P) {\lambda_i}^{-4+a} BW_i \, exp\left(-\frac{C_2}{\lambda_i T_{planck}(P)}\right) \tag{2.3.10}$$

$\epsilon(P)$ is a (temperature-dependent) effective emissivity, $\mathbb{TF}_i$ is a transfer function, λ_i is the wavelength of light corresponding to the pixel number i, $a = 0, \frac{1}{2}$ stands for Wien and Laplace fits, BW_i is an individual pixel bandwidth and $C_2 = 14389 \, K\mu m$ is the second radiation constant. 'Persistent background' is a non-polarized triplet of unidentified nature which was emitted by the laser. Since it was unpolarized, its amplitude was not changed by the laser attenuation system. Because of the narrow spectral footprint and small amplitude, it did not affect the temperature determination, but it was used a marker for wavelength calibration.

The data was processed during acquisition to be aware of the maximum peak temperature and not to overheat the absorber. First, the c_i was measured by a long, ~60 s exposure with laser attenuated all the way down, to less than the power meter limit of detection (<2 mW). During the next stage, the laser power was increased in steps while monitoring the deviation from linearity of I_i versus measured average laser power: the deviation from the linear extrapolation based on previous spectra was monitored. As the

deviation exceeded a threshold (based on readout noise) the values of α_i were frozen based on the spectra for lower average powers and for the rest of the points $BB_i(T_{peak}(P))$ was calculated as

$$BB_i\left(T_{planck}(P)\right) = I_i - c_i - \alpha_i(P + \delta P(P)) \tag{2.3.11}$$

where $\delta P(P)$ was chosen to minimize the area under diamond Raman peak in BB_i. Specifically, a coarse second derivative, $dd(f)_i \equiv 2 < f >_i - < f >_{i+a} - < f >_{i-a}$, where brackets stand for averaging around central value, can be calculated for the Eq. 2.3.11, giving

$$0 = dd(I_i) - dd(\alpha_i)(P + \delta P(P)) \tag{2.3.12}$$

which defines δP. This operation makes the determination of BB_i insensitive to errors in measuring P ($P = P + error$) and errors of scaling of the form $\alpha_i = \alpha_i * (1 + error)$. Scaling of α_i has the physical meaning of changing the reflectivity of the absorber i.e. change with temperature.

The temperature was than estimated fitting $BB_i\left(T_{planck}(P)\right)$ to the form of Eq. 2.3.10. The two unknowns are $\epsilon(P)$ and $T(P)$, which makes it possible to estimate them as intercept and slope after simple manipulation with Eq. 2.3.10:

$$\log\left(\frac{BB_i}{TF_i{\lambda_i}^{-4+a}BW_i}\right) = \log(\epsilon) - \frac{1}{\lambda_i}\frac{C_2}{T_{planck}} \tag{2.3.13}$$

The resulting T_{planck} was used to calculate the peak temperature $T_{peak} = T_{plank} + \delta T(T_{plank})$ where the correction δT is the result of simulations described in the previous section. The specific calculation which produced the reported results used the Wien fit and the thermoreflectance pulse shape.

To control the quality of the fit, the temperature was estimated using two different, but overlapping pixel sets, both corresponding to wavelengths longer than 1200 nm where laser background junk was absent. In the case that these two values disagreed the data was discarded. The difference was progressively decreasing with increase in temperature and in the plateau region (~1600 K) was less than 40 K (see Fig. 2.16). Identified cases of failed measurements were attributed to mechanical drift of the

measurement setup, when the absorber moves in the field of view. Occasionally the first heating after a pressure change would also produce inconsistent results, if it was done too soon without allowing some time for the pressure to relax – it would normally took ~1h after increasing the pressure for pressure to stabilize, likely due to slow flow of the indium in the seal.

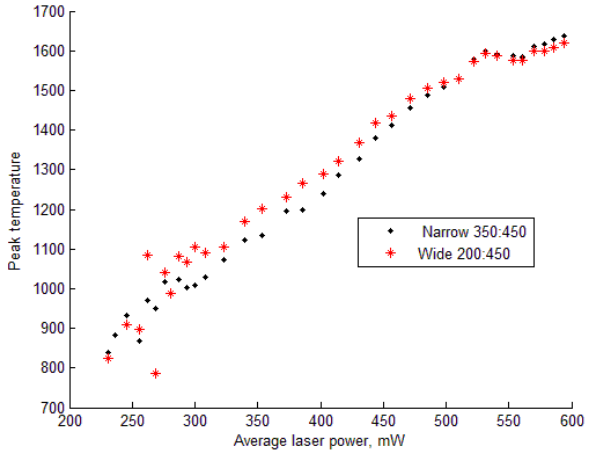

Figure 2.16: Heating curves to show the effect of varying the fit support on a good day. This means that the two heating curves are produced from the same data using two different subsets of detector pixels to estimate the temperature.

The key assumption behind the Eq. 2.3.9 is that the shape of the 'linear background' does not change with laser pulse energy so the spectral and the power dependence can be factored. This is a less strict requirement then linearity in power, which may fail due to nonlinear thermoreflectance of the absorber. The physical reasoning behind it is that because of the short pulse duration the temperature of the cell regions responsible for the radiation (diamond and alumina passivation barrier) does not change and thus the radiation spectrum will be defined by intensity of the laser radiation in the sample region. The laser radiation intensity is the sum of incoming and reflected intensities, the former is linearly related to the laser average power and the latter weakly depends on the temperature of the platinum absorber via reflectivity which may or may not break the linear dependence on the average laser power. Literature data on the temperature dependence of platinum reflectivity is scarce and does not cover the region of interest: the reflectivity in visible is fairly linear with temperature (Madjid 1973 [8], Cagran 2002 [7]) and reflectivity for longer wavelengths is reported to be temperature independent [9]. A potential problem

with this explanation is the case when some of the radiation mechanisms (fluorescence) will saturate earlier than others (Raman) but it appears not to be happening according to the data we have.

Experimentally there are two arguments in support of this assumption, apart from the fact that it yields a good fit to data. First, in the temperature region where the incandescent signal was undetectable (below 700 K), the signal was described by the linear relation $I_i = c_i + \alpha_i P$ within the measurement error. Extrapolating this behavior up in power could introduce progressively increasing error, but the exponential growth of incandescent radiation intensity with temperature effectively makes the fit insensitive to this variation. Second, the response of the system was measured under both pulsed and continuous laser radiation with similar average powers. Given the width of the pulse this corresponds to variation of instantaneous laser power by a factor of the order of$\sim 10^3$. The result is that the variation of the α_i was less than 3% across the region used for fit. If the values of α_i measured with CW laser are used to estimate temperatures, which is quite an extreme case, this ruins the fit at low temperatures, where the relative contribution of fluorescence is large and affects the high temperature region weakly – see Fig. 2.17 for example.

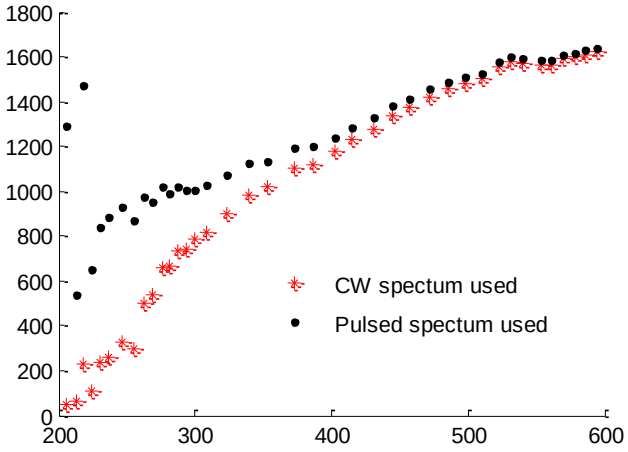

Figure 2.17: The effect on the peak temperature determination of using different estimates of linear spectra to separate BB signal. Three orders of magnitude change of instantaneous laser power does not affect temperature estimation in the plateau region. However, in the lower temperature region the discrepancy is very large. This suggests that the proper linear spectrum should be used if the melting temperature needs to be determined accurately.

2.3.3 Origin of plateau

In the absence of phase transitions a heating curve should be a monotonically increasing curve of temperature vs average laser power without any singularities. The slope of the curve can slowly vary due to temperature dependent emissivity. However, one can expect a singularity in the curve when the sample undergoes a phase transition. Experimentally, for the pulsed laser heating, plateaus were observed for some materials at melting (platinum and stainless steel [1], iron [2], hydrogen [3]) with the plateau temperature matching the melting temperature of the substance.

There are many possible reasons for a plateau (or a discontinuity) to occur: this can be latent heat of melting, abrupt change of reflectivity on melting (measured in [7]), sudden change in thermal conductivity, hydrodynamic effects leading to change of laser coupling efficiency etc. Some of them were analyzed in [5] and [6]. A brief conclusion from these works is that the latent heat of melting alone is not sufficient to explain the observed plateaus and one needs to look for alternative explanations.

Another interesting point discussed in these papers is that the plateau occurrence is conditional on the rate of heating. If one chooses a way to quantify the strength of a plateau, than the amplitude of the effect has a strong dependence on the rate of heating: there is a material and geometry dependent time constant (about 1 μs for the case of our geometry) which maximizes it. Intuitively this is an expected result. In the limit of slow or CW heating, the equilibrium temperature for a given laser power is determined by the thermal conductivity of the system, not the thermal capacity which is related to the latent heat of melting. Thus the latent heat of fusion should have no effect on the temperature dynamics on melting. The plateaus experimentally measured under these conditions (say for Sn [12], Xe [ref], Mo [13], FeC [14]) apparently have a different physical nature. In the other limit, when heating becomes faster, a strong spatial temperature gradient arises. This causes large conduction heat flux and progressively larger portion of the laser energy to be lost to conduction as opposed to be used for melting which can use only a fixed amount of energy ~ mass of the sample multiplied by the latent heat. An ideal case would be adiabatic in a sense that all of the laser energy is absorbed uniformly by the sample and none is lost to the thermal insulation.

In our experiment a physical property related to temperature was measured: time resolved change in platinum reflectivity at 488 nm. Since the reflectivity of platinum for this wavelength is continuous and nearly a linear function of the temperature this enables the measurement of the shape of a temperature pulse *T(t)*, but does not give information on its amplitude. The results do not indicate a strong change in pulse shape across a plateau region but the data quality is not sufficient to rule out the shape change unambiguously. This is important because as it was discussed in the "*Temperature measurement and Planckian average"(2.3.1)* section of this chapter, the value of the peak temperature that can be extracted from a time averaged BB spectrum depends on the shape of temporal temperature profile and one can expect errors in T_{peak} if the temperature pulse shape changes dramatically.

2.3.4 Heating curves

Figures 2.18, 2.19 and 2.20 show all the heating curves having a high temperature plateau. For clarity different curves are offset by the values indicated in parentheses. For the "155 GPa May 26" series the presence of the plateau is not clear because of the coarse stepping in laser power, but the curve is shown for completeness. For these pressures no other curves were measured reaching these temperatures. In the second run there were more high temperature curves with no plateau behavior, but this was associated with the absorber being deformed by a ruby with pressure increase past 125 GPa resulting in inhomogeneous heating that averages out any underlying plateau. Spatially resolved incandescent images confirmed this. (Fig. 2.21)

It is worth noting that even at the same pressure the laser coupling to the absorber varied, from curve to curve as the DAC was removed from its mount for other measurements and then the laser was refocused. The result is different peak temperature values for the same laser power for different curves. However the plateau stayed at the same temperatures, which increased our confidence in the physical origin of the plateau as opposed to say drift of the cell or accidental thermal shorting of the absorber. The key differences between runs one and two is that in run one the absorber had alumina coating separating it from hydrogen and in the run two it did not.

Some curves, where the signal-to-noise ratio is sufficient, show the second anomaly – change of slope at lower temperatures: second curve of Fig. 2.18, second and third curves on Fig. 2.19 and second curve on Fig. 2.20. The temperatures of these anomalies are in agreement with earlier measured melting temperatures of hydrogen for the corresponding pressure, but the random noise is high. Systematic error due to possible errors in linear background subtraction can in principle lead to similar behavior, (in the case of systematic overcorrection) however this is unlikely. To unambiguously determine the nature of these anomalies additional data or improvements in hardware, discussed later is required. However, in the present range of pressures, the melting line was already measured by Eremets and Troyan [15], so spending much more resources on these improvements would be impractical.

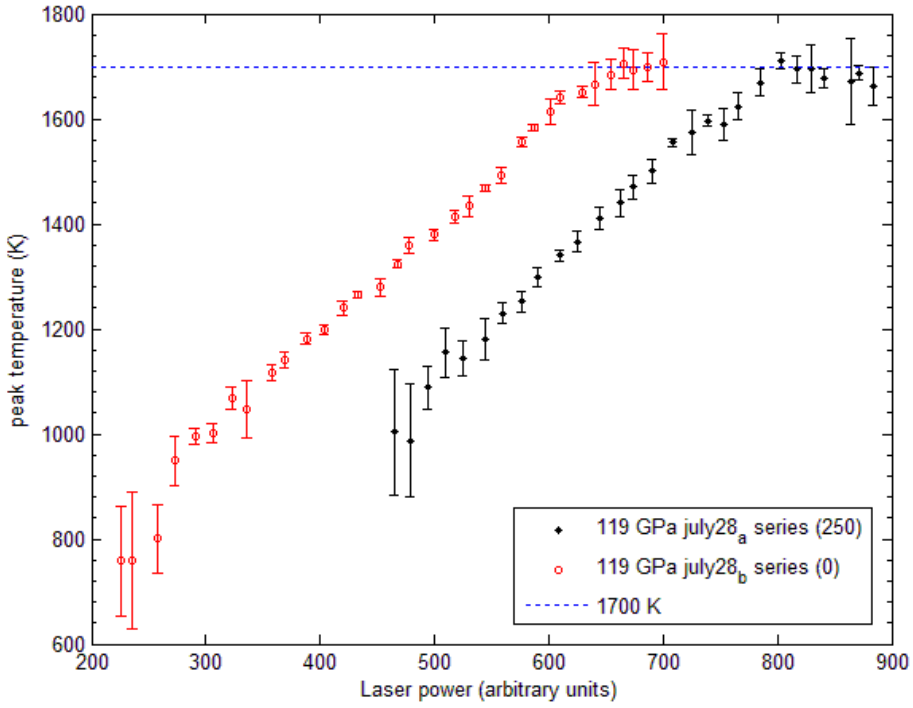

Figure 2.18: The peak temperature versus average laser power for pressure of 119 GPa

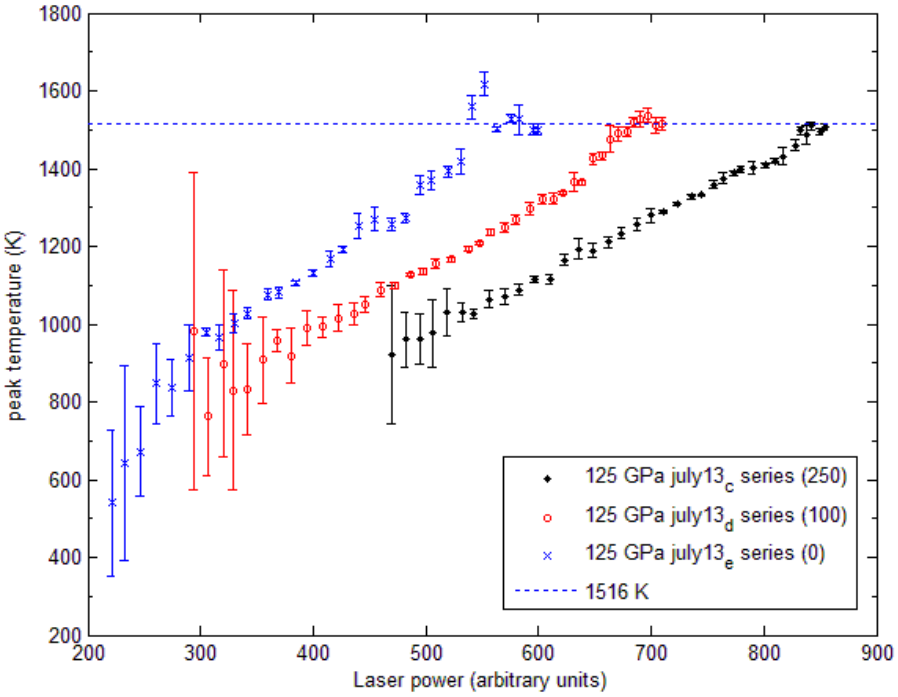

Figure 2.19: The peak temperature versus average laser power for pressure of 125 GPa

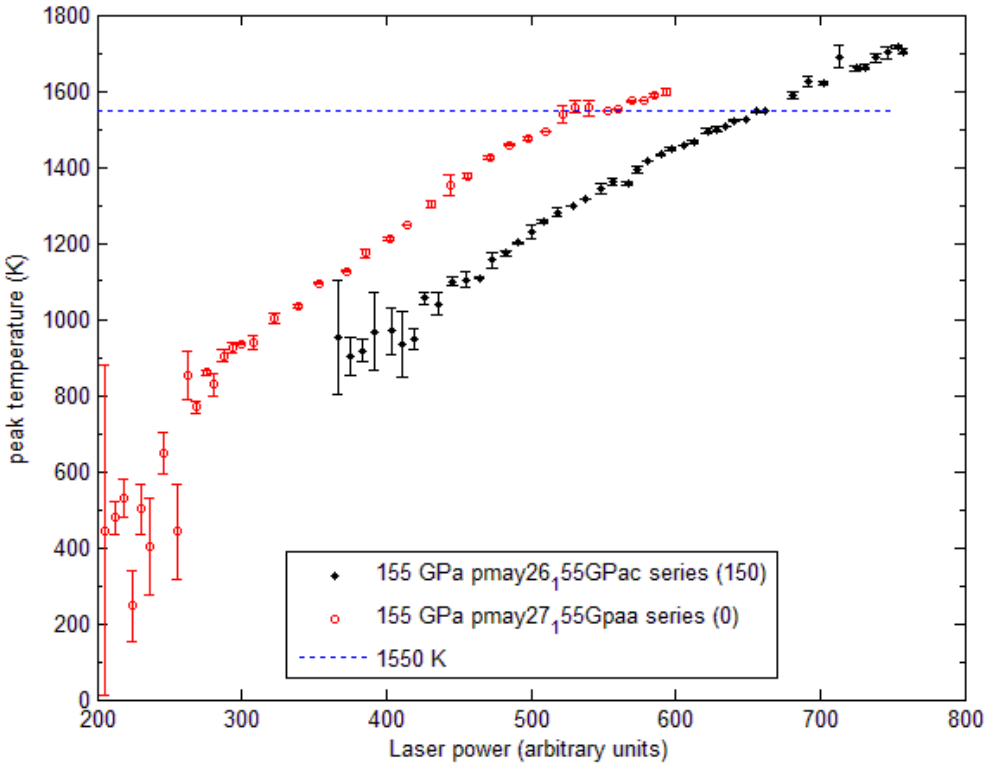

Figure 2.20: The peak temperature versus average laser power for pressure of 155 GPa

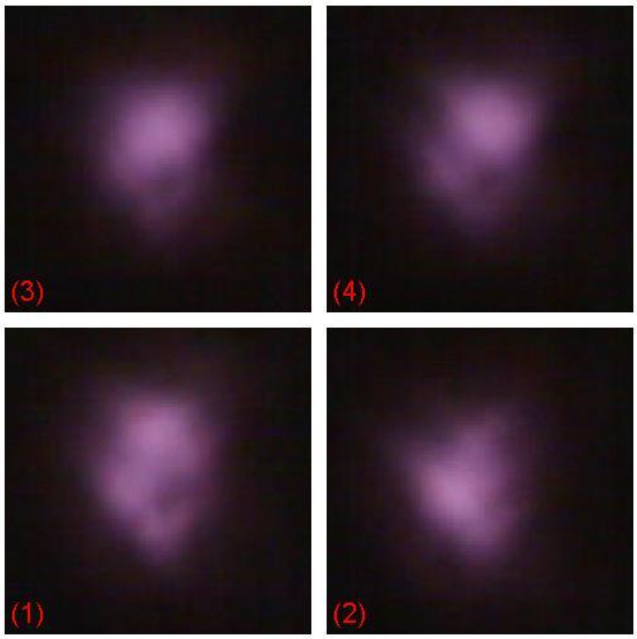

Figure 2.21: Four selected video frames of the incandescent image if the hot absorber at a pressure of ~150 GPa in run2. The glowing part is about 20 microns in linear dimension. In our measurement of a heating curve this nonuniformity would average out plateaus.

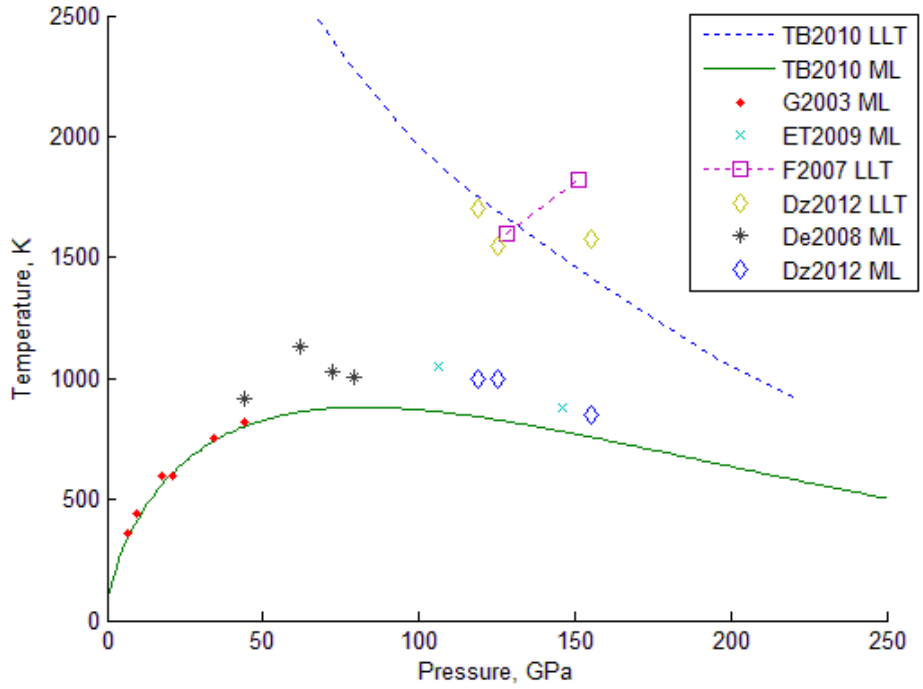

Figure 2.22: Warm hydrogen phase diagram. The plotted data correspond to works of: TB2010 [16], G2003 [17], ET2009 [15], F2007 [18], Dz2012 (this work), De2008 [3]. ML and LLT tags correspond to melting and liquid-liquid transition data. Dashed line for F2007 data indicates that the phase transition line should intersect the purple line somewhere.

2.3.5 Proposed phase diagram discussion.

The high temperature anomalies in the heating curves occur in the region where the LL phase transition was predicted to take place [19] [20] [21] [16] . The phase diagram showing our data along with predictions and previous data is shown on the Figure 2.22. Data of [3] is altered towards higher temperatures because of matters discussed above. Note that in Fortov [18] experiment two points show different phases, not the transition, which happens somewhere in-between.

A secondary measurement is the reflectivity of the absorber/sample. Whereas one expects a sharp change in transmission of hot hydrogen at the PPT, reflection is less sensitive. The challenge here is the following. First of all, if metallic hydrogen is a reasonable liquid metal, it will have a reasonably high

reflectivity and a small penetration depth for light, so that for T greater than the transition temperature to the PPT, hydrogen, not the absorber, will dominate the reflection. However, platinum hydride is a reasonably good metal [22] so that the change of reflectivity at the PPT may be small. This problem is exacerbated because the reflectivity of most metals is temperature dependent, so one must observe a small change on a large slope with changing temperature or a change of slope corresponding to different temperature dependencies of hydrogen and platinum hydride reflectivities. We did not perform systematic measurements on reflectance vs. temperature due to mechanical stability problems for all pressure points. Our preliminary data shows a change in intensity of reflected light in the plateau region (Fig. 2.23), consistent with either darkening of the sample or change in the diffuse/specular ratio towards weaker diffuse and stronger specular reflection.

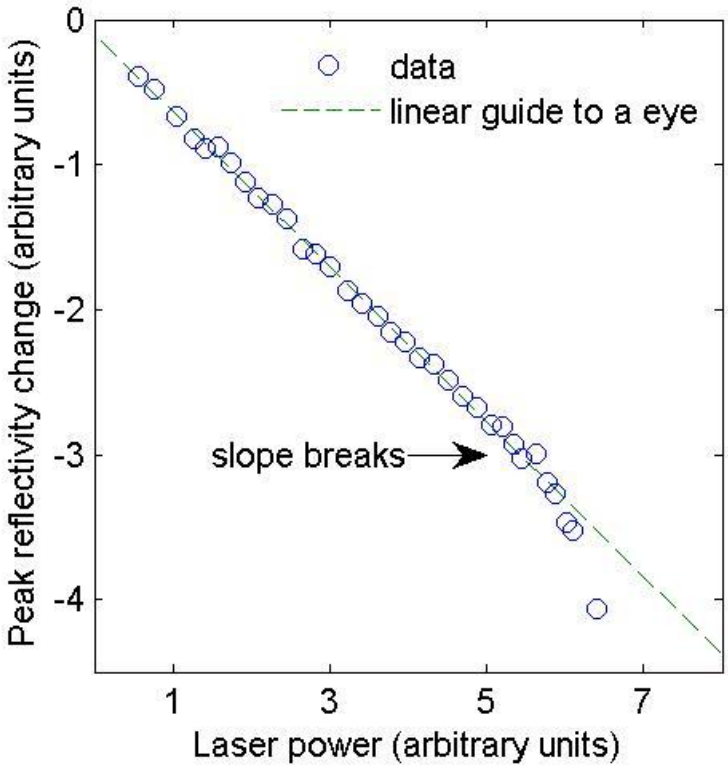

Figure 2.23 The change in reflectivity in a heating curve. Each point represents a different laser power and plotted is the maximum amplitude of the reflectivity change for this laser power. There is a break in the curve at the power where the plateau occurs in the heating curve. This data is for a pressure of 125 GPa.

There is an argument which can be made which suggests that the observed behavior is indeed inherent to hydrogen and not due to any chemical changes in the platinum absorber. Based on our data we

cannot strictly exclude the possibility that plateaus correspond to a phase transition in platinum hydrate absorber material. We believe that the two successful runs where the LLT pressure and temperature conditions were realized used different absorbers: platinum hydride and platinum. For the first run the absorber was covered with a layer of ALD alumina and in the second run the absorber was bare platinum. The alumina was shown to inhibit hydrogen [17] and helium [23] [24] diffusion into metal gaskets and diamonds earlier. Furthermore, in our runs we do not see the quenching of the ruby fluorescence when a ALD coated ruby is heated in hydrogen media and a bare ruby does show quenching under the same conditions which slowly reverses when a ruby is brought back to zero pressure and taken out of the DAC [3] Thus we believe that in the first run we observed the plateau with the platinum absorber and in the second run the absorber was converted into platinum hydride [25].

The plateau at 155 GPa with the ALD coating must be corrected down, due to the large thermal impedance of the alumina layer, as the hydrogen will not be as hot as the absorber. We estimate this correction to be as large as 70 K, which brings the data of the two runs in better agreement with the expected behavior for the PPT.

The method described in this chapter is marginally suitable for determination of the hydrogen melting temperature in the sense that it is capable of providing reasonable signal-to-noise at low temperatures (see the curve for 155 GPa) but in the second run where the most data was collected we had to limit exposure time to avoid cell drift due to an unidentified mechanical instability related to climate control of the experimental room which rendered low temperature data extremely noisy and unsuitable for determination of the melting. A possible extension is to use the additional spectral region of 1.8 to 2.2 μm which is available in commercial InGaAs diode arrays, but in the case of the camera used for this experiment it was limited in-camera to lower the noise due to room temperature blackbody radiation. The benefit of the extended spectral range is that it would increase the sensitivity in the low temperature range, since the BB signal intensity grows exponentially towards longer wavelength and the linear background does not. Thus the temperature where the contribution of BB signal is distinguishable in the presence of the linear fluorescent background is lower.

Another avenue for expansion of the range of the measurable temperatures is to correlate the results of simultaneous thermoreflectance and pyrometry measurements. The advantage of the thermoreflectance method is that, although it cannot give absolute value of temperature, the useful signal is nearly linear in temperature as opposed to the exponential BB signal, which allows probing lower temperatures given a calibration obtained by correlating the results of both method at higher temperatures where pyrometry provides absolute measurement of the temperature.

In conclusion we have demonstrated that with our new techniques hydrogen at high static pressures can be studied in the high temperature region of the PPT. At the current time all evidence of the PPT is indirect: Weir et al [26] demonstrate conductivity, but no phase transition; Fortov et al [18] show a density change for deuterium, but do not measure conductivity in their deuterium sample; their data, as ours, presents evidence of a phase transition. Our current measurement demonstrates a close correlation between a plateau demonstrative of a phase transition and theoretical predictions for the PPT. Our static pressure method has great promise to provide rigorous evidence of metallization from optical properties of the sample, complementing our present observations. There are some uncertainties that accrue in this challenging experimental region. We believe that the absorbers in run1 and run2 were platinum and platinum hydride, respectively. New experiments are being developed with different absorber materials and to measure the transmission of the hot dense hydrogen.

2.3.6 Bibliography

[1] S. Rekhi, J. Tempere and I. F. Silvera, "Temperature determination for nanosecond pulsed laser heating," *Review of Scientific Instruments,* vol. 74, pp. 3820-3825, 2003.

[2] S. Deemyad, E. Sterer, C. Barthel, S. Rekhi, J. Tempere and I. F. Silvera, "Pulsed laser heating and temperature determination in a diamond anvil cell," *Review of Scientific Instruments,* vol. 76, p. 125104, 2005.

[3] S. Deemyad and I. Silvera, "Melting Line of Hydrogen at High Pressures," *Phys. Rev. Lett.,* vol. 10, no. 15, 2008.

[4] S. Deemyad, A. N. Papathanassiou and I. F. Silvera, "Strategy and enhanced temperature determination in a laser heated diamond anvil cell," *Journal of Applied Physics,* vol. 105, pp. 093543--093543, 2009.

[5] Z. M. Geballe and R. Jeanloz, "Origin of temperature plateaus in laser-heated diamond anvil cell experiments," *J. Appl. Phys,* vol. 111, no. 12, p. 123518 , 2012.

[6] J. A. Montoya and A. F. Goncharov, "Finite element calculations of the time dependent thermal fluxes in the laser-heated diamond anvil cell," *J. Appl. Phys.,* vol. 111, no. 11, p. 112617 , 2012.

[7] C. Cagran, B. Wilthan and G. Pottlacher, "Optical properties (at 684.5 nm) and radiance temperatures at the melting point of group VIIIb transition metals cobalt, nickel, palladium, and platinum," *High Temperatures - High Pressures,* vol. 35/36, no. 6, p. 667 – 675, 2003/2007.

[8] A. Madjid, R. Stover, J. Martinez and G. Grimvall, "Normal spectral emissivity of platinum in the red and in the green in vacuum and helium," *Zeitschrift fur Physik B Condensed Matter,* vol. 17, pp. 125--134, 1974.

[9] S. Deemyad and I. F. Silvera, "Temperature dependence of the emissivity of platinum in the IR,"

Review of scientific instruments, vol. 79, pp. 086105--086105, 2008.

[10] L. Aksyutov, "Normal spectral emissivity of gold, platinum, and tungsten," *Journal of Engineering Physics and Thermophysics,* vol. 27, pp. 913--917, 1974.

[11] N. Subramanian, A. Goncharov, V. Struzhkin, M. Somayazulu and a. R. J. Hemley, "Bonding changes in hot fluid hydrogen," *PNAS,* vol. 108 , no. 15, pp. 6014-6019, 2011.

[12] R. Briggs, D. Daisenberger, A. Salamat, G. Garbarino, M. Mezouar, M. Wilson and P. McMillan, "Melting of Sn to 1 Mbar," 2012.

[13] D. Santamaria-Perez, M. Ross, D. Errandonea, G. Mukherjee, M. Mezouar and R. Boehler, "X-ray diffraction measurements of Mo melting to 119 GPa and the high pressure phase diagram," *The Journal of chemical physics,* vol. 130, p. 124509, 2009.

[14] O. Lord, M. Walter, R. Dasgupta, D. Walker and S. Clark, "Melting in the Feâ€“C system to 70Â GPa," *Earth and Planetary Science Letters,* vol. 284, pp. 157 - 167, 2009.

[15] M. Eremets and I. Troyan, "Evidence of maximum in the melting curve of hydrogen at megabar," *JETP Letters,* vol. 89, no. 4, pp. 174-179, 2009.

[16] I. Tamblyn and S. Bonev, "Structure and Phase Boundaries of Compressed Liquid Hydrogen," *Phys. Rev. Lett. ,* vol. 104 , no. 6, 2010.

[17] E. Gregoryanz, A. F. Goncharov, K. Mi, H. Mao and R. J. Hemley, "Raman Spectroscopy of Hot Dense Hydrogen," *Phys. Rev. Lett.,* vol. 90, no. 17, 2003.

[18] V. E. Fortov and e. al, "Phase Transition in a Strongly Nonideal Deuterium Plasma Generated by Quasi-Isentropical Compression at Megabar Pressures," *Phys. Rev. Lett.,* vol. 99, no. 18, 2007.

[19] S. Bonev, E. Schwegler, T. Ogitsu and G. Galli, "A quantum fluid of metallic suggested by first-principles calculations," *Letters to Nature,* vol. 431, pp. 669-672 , 2004.

[20] W. Lorenzen, B. Holst and R. Redmer, "First-order liquid-liquid phase transition in dense hydrogen,"

Physical Review B, vol. 82, p. 195107, 2010.

[21] M. Morales, C. Pierleoni, E. Schweglerd and D. M. Ceperley, "Evidence for a first-order liquid-liquid transition in high-pressure hydrogen from ab initio simulations," *PNAS,* vol. 107, no. 29, pp. 12799-12803, 2010.

[22] K. Ohta, *Private communication with I. Silvera.*

[23] G. D. Mukherjee, *private communication.*

[24] D. Santamaria-Perez, G. D. Mukherjee, B. Schwager and R. Boehler, "High-pressure melting curve of helium and neon: Deviations from corresponding states theory," *Phys. Rev. B,* vol. 81, no. 21, p. 214101, Jun 2010.

[25] T. Scheler, O. Degtyareva, M. Marquas, C. L. Guillaume, J. E. Proctor, S. Evans and E. Gregoryanz, "Synthesis and properties of platinum hydride," *Phys. Rev. B,* vol. 83, no. 21, p. 214106, Jun 2011.

[26] W. J. Nellis, S. T. Weir and A. C. Mitchell, "Minimum metallic conductivity of fluid hydrogen at 140 GPa (1.4 Mbar)," *Phys. Rev. B,* vol. 59, no. 5, p. 3434–3449 , 1999.

3 Platinum surface reconstruction upon pulsed laser heating

3.1 Introduction

This chapter describes work which was performed as a byproduct in the process of development for the pulsed laser heating hydrogen experiment. In the temperature and wavelength range where the measurements on hydrogen were performed there was no prior data on platinum emissivity which can be crucial for the temperature determination. A potential problem is if the spectral emissivity has a strong dependency on temperature. This can introduce significant errors in temperature determination with the effect being stronger at higher temperatures around the peak of the Planck curve, where small changes of slope due to unaccounted changes in the emissivity are more noticeable compared to the decreased slope of the BB curve. We decided to investigate if our temperature determination technique yields correct results for the known melting point of platinum. It turned out the method described in The Chapter 2 works satisfactorily for melting temperature determination; however we encountered some interesting behavior which potentially carries practical consequences for the high pressure community. The surface of the laser heated sample undergoes reconstruction at temperatures well below melting (more than 200 K) substantially changing coupling of the laser power to the sample. Using the methodology of published works [1], this surface modification can be easily be mistaken for melting, resulting in erroneous determination of the melting temperature.

3.2 Importance

A significant part of high pressure research revolves around determination of phase diagrams of materials at high pressures, with melting being one of the interests. Because of the specifics of the high pressure setting, even if the thermodynamic conditions corresponding to a phase transition are realizable, detection of the transition is not straightforward. A typical linear sample size can be of the order of several microns for multi megabar experiments making detection more difficult. Experimental measurement times can often be limited due to uncontrollable condition such as chemical reactions ([2] , ets) or fast sample out diffusion at elevated temperatures [3].

Robust analytic methods to detect melting at high pressure include X ray diffraction, resistivity measurements and spectroscopy for transparent samples but they all have their limitations. Particularly, in the case of transition metals like tantalum and iron, which quickly form carbides at elevated temperatures, using these methods is troublesome and faster techniques are desirable. Because of the simplicity, surface morphology change on heating is used as well, despite some controversy [2]. A related indicator of melting, onset of speckle motion is used for determination of melting in the case of transparent samples [4], [5] . A phenomenon which can disturb both measurements is surface melting at lower temperatures then bulk melting. Under certain conditions surface melting does not behave as a phase transition, but rather a crossover with thickness of the melt gradually increasing with temperature [6]. This effect, however, can be suppressed in a typical high pressure setting by presence of a solid-solid interface stabilizing the surface [6].

3.3 Experimental

The setup described in the "Experimental method" (2.2) section of the chapter 2 was used to investigate platinum melting. The platinum sample was 250 μm thick [thicker than in [7], so no puncturing occurs] foil silver soldered to a copper heat sink to ensure thermal stability. No noticeable heating of the heat sink was detected during an experiment. The sample surface was polished with diamond lapping paper down to 1 μm grit size.

The sample was exposed to the laser for a fixed duration of about 5 seconds before the spectrum measurement was taken. For every laser power, several spectra, 4 to 100, were taken with individual temperatures providing a measure of temperature fluctuations. No drift in temperature was detected except possibly for a single laser power value per series, corresponding to the onset of the surface restructuring.

Temperature was determined using a similar routine as in the case of hydrogen, with the difference being nearly absent fluorescent/linear background. When the fluorescence was corrected, the effect on the temperature determination at platinum melting was about 1 K, significantly below other error sources. However, below 1200 K, disregarding the correction would produce unphysical results. With the correction the detection range could be extended down to 800 K with the limiting factor being the exposure length. Random uncertainty of temperature determination in the range of interest was mostly due to fluctuation of temperature itself rather than an instrument or photon shot noise.

The heating laser power was varied from nearly zero to a large value corresponding to peak temperatures above the melting point. For a single spot on the sample normally three curves were measured – the first for increasing laser power, when sample surface reconstruction happened, then lowering the laser power to almost zero and then raising the power again to observe heating of the reconstructed surface.

The spectral emittance of the restructured surface, averaged over acceptance angle (aperture) of the optical system was measured relative to that of the original surface by resistively heating the sample

to a specific temperature, about 780 K, collecting incandescent radiation spectra from both modified and flat regions of the sample and dividing one by another.

Thermoreflectance (TR) was not thoroughly studied above the reconstruction point because of the strong surface changes: above the reconstruction point the measured intensity of the reflected beam is no longer indicative of surface temperature, but rather of surface shape evolution. Wien and Laplace corrections calculated based on the TR temperature pulse profile (measured below the reconstruction temperature with descending laser power) were used. Using Wien versus Laplace fitting results in a spread of less than two degrees.

3.4 Results on surface reconstruction

Under conditions of pulsed laser heating platinum surface undergoes restructuring at temperatures well below melting point of the bulk. The process of restructuring is unstable: once a small local change to the surface happens, emittance of the region goes up, thereby increasing the coupling between the laser and the surface, increasing the heat influx and prompting further surface restructuring in adjacent areas.

There are two factors contributing to the instability, firstly platinum emissivity goes up with temperature introducing a positive feedback; secondly it was reported in ref [8] that in a similar temperature regime, but using shorter pulse (tens of nanoseconds pulse width as opposed to hundreds in our case), platinum can fail plastically after a single pulse, presumably due to large temperature gradients prompting large strains. The regions of plastic failure will have higher emittance supporting the positive feedback cycle. We observed a slow growth of the modified region at the critical laser power: damage always starts in a single point and then propagates from it reaching the equilibrium size in the course of roughly 10^5 laser pulses.

The instability was observed as a discontinuous change of incandescent signal intensity with increase of pulse energy. Figure 3.1 shows typical raw data: signal binned at pixels around $\lambda = 1.5\ \mu m$ as a function of average laser power for a typical cycle. With initial increase of laser power the signal is below the detection limit until the threshold (it is about 155 mW for this run) where the surface modification happens. At the surface reconstruction, signal strength increases roughly 3 orders of magnitude after a minor increase of the laser power. This corresponds to an increase of temperature from about 800 K to 1700 K as a result of increased coupling of the laser energy to the platinum; the higher temperature was measured by pyrometry and lower was estimated from the change of the signal strength.

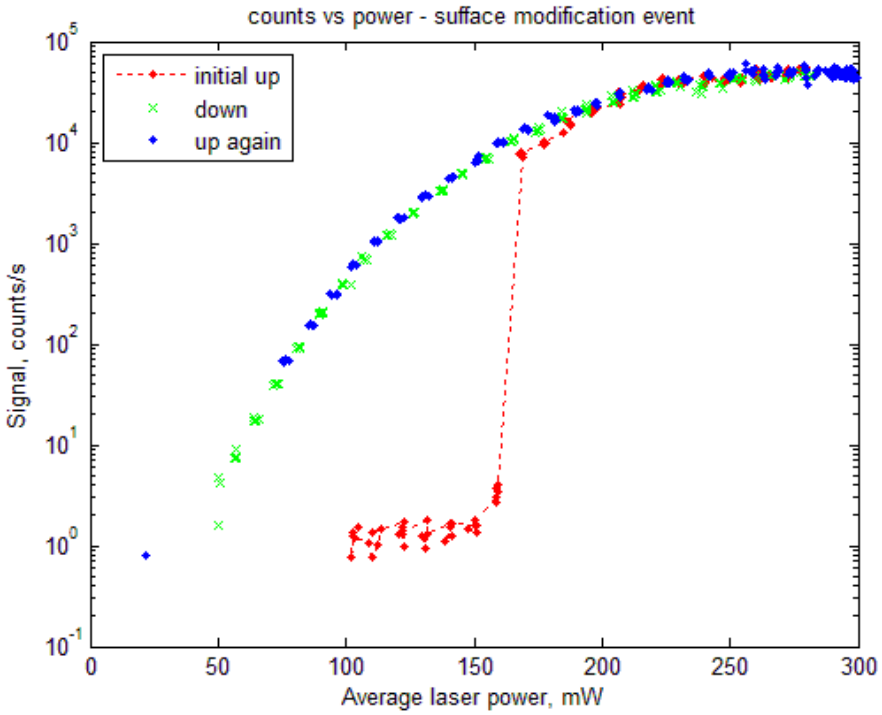

Figure 3.1 Incandescent radiation intensity as a function of average laser power: surface modification shows up as a discontinuity during the initial heating cycle

The peak temperature where the surface modification starts can be estimated in two different ways. The first way is based on the measured emissivity change of the surface and the measurement of the just-after transition temperature. The emissivity change is nearly wavelength independent in the range of measurement (1100 to 1600 nm) and was measured as described above to be a 2.43(0.02) times increase. Assuming temperature independent properties of platinum translates into the statement that the increase of the emissivity results in a proportional increase in T_{peak}-$T_{ambient}$ for each laser pulse. Given that after 2.43 times increase of absorbed energy a laser pulse brings the surface temperature to 1700 (100) K , yields the critical temperature ~880(40) K (including the dependence of thermodynamic variables in the analysis will increase the value, while including temperature variation of the emissivity drives it down). The second way to estimate is the amplitude of the discontinuity in the single channel incandescent signal. The measured ratio of signals before and after the transition is ~2000. This corresponds to the low temperature of 780(25) K, if the emissivity change is taken into account. [Uncertainty is indicated for

nominal variation of the lowest post reconstruction temperature of 100 K.] It is worth noting that if resistive (up to ~900 K) or continuous wave laser (up to 2000 K) heating is used, platinum in this temperature region does not show any special changes in emissivity. Figure 3.2 shows the morphology of the surface after the reconstruction as seen with a scanning electron microscope – the changes compared to the original surface are clearly evident.

Once the surface is modified, it stays rough, even though there is a constant evolution reflected in gradual changes, 'motion' of the speckle of the heating laser. When the laser power increased so that the bulk melting is realized, the surface does not smoothen: Figure 3.3 shows an image of a sample which was heated above the melting point. A clear distinction is the presence of the deep cracks.

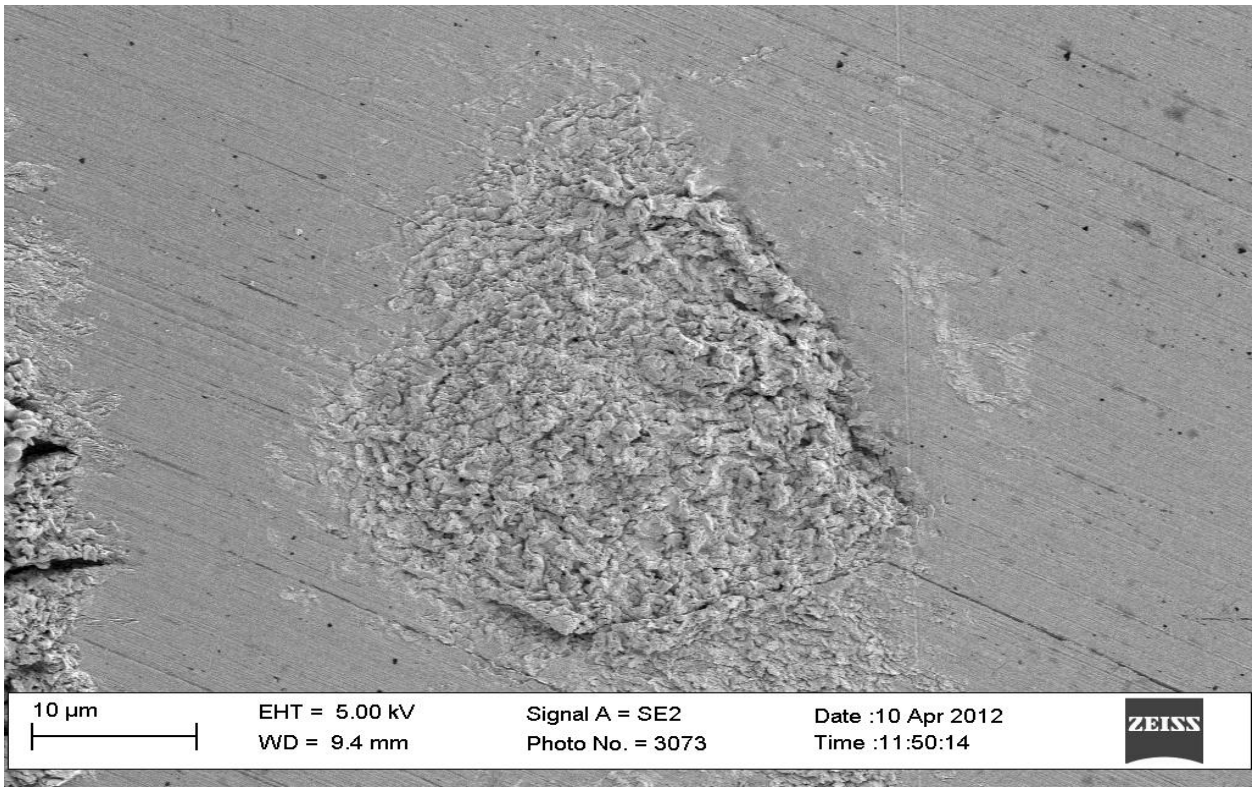

Figure 3.2 SEM image of a modified platinum surface

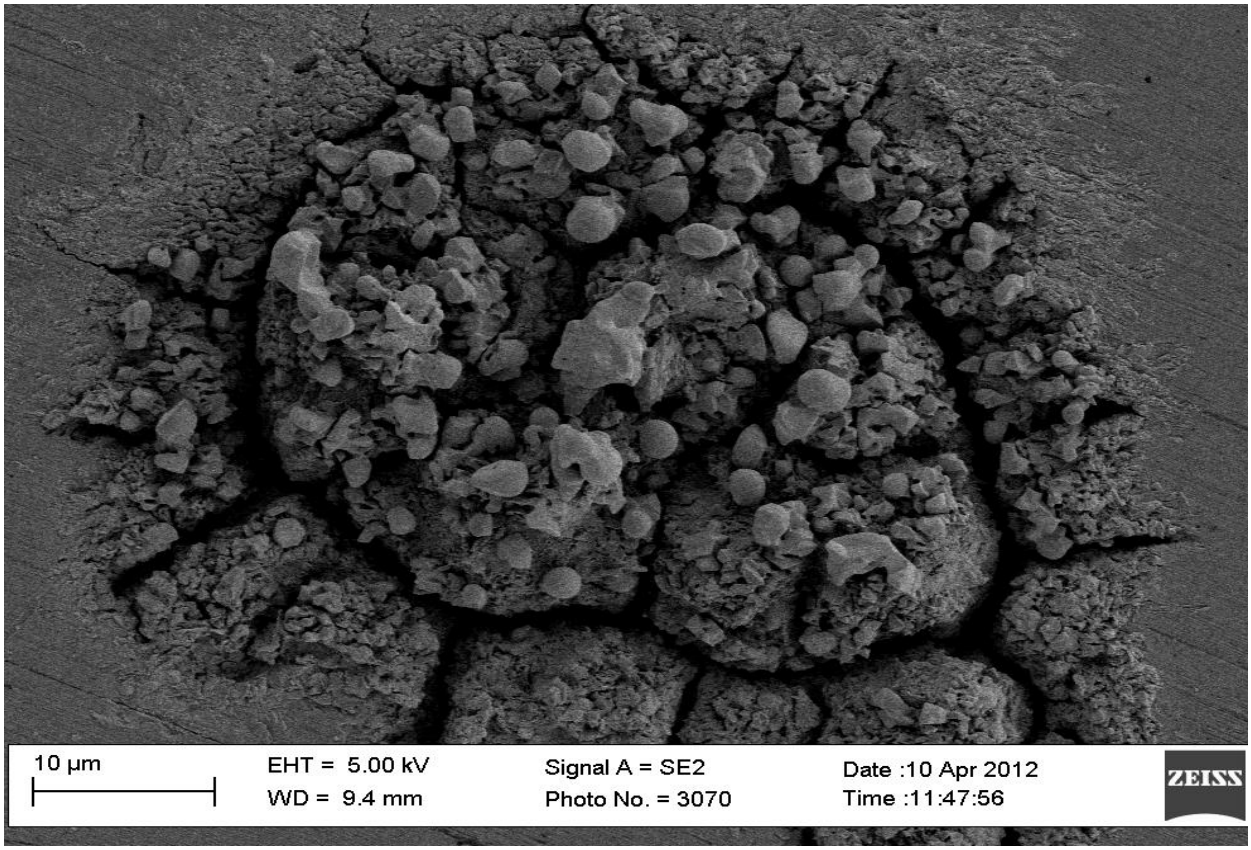

Figure 3.3 SEM image of the platinum heated above melting

3.5 Melting and Results for the metrology

As the laser pulse energy is increased above the surface reconstruction point, the peak temperature changes linearly until bulk melting occurs. At melting, the slope $T_{peak}(P)$ breaks and a knee in the curve is observed. Figure 3.4 shows three successive traces on a single spot of platinum. The curves are offset along power axis for clarity. Black dashed lines are linear fits before the break and after the break. Numbers are the temperature values at the intersection of these. Thermoreflectance measurements do not indicate either surface flattening during a pulse nor a cool down solidification plateau – this suggests that during a short time in liquid state the surface does not have enough time to flatten out and non uniform heating takes place. Strong fluctuations of the measured temperature above the plateau are consistent with the observed dynamics of the speckle motion: slow gradual change before the slope break is succeeded by fast fluctuations after the break.

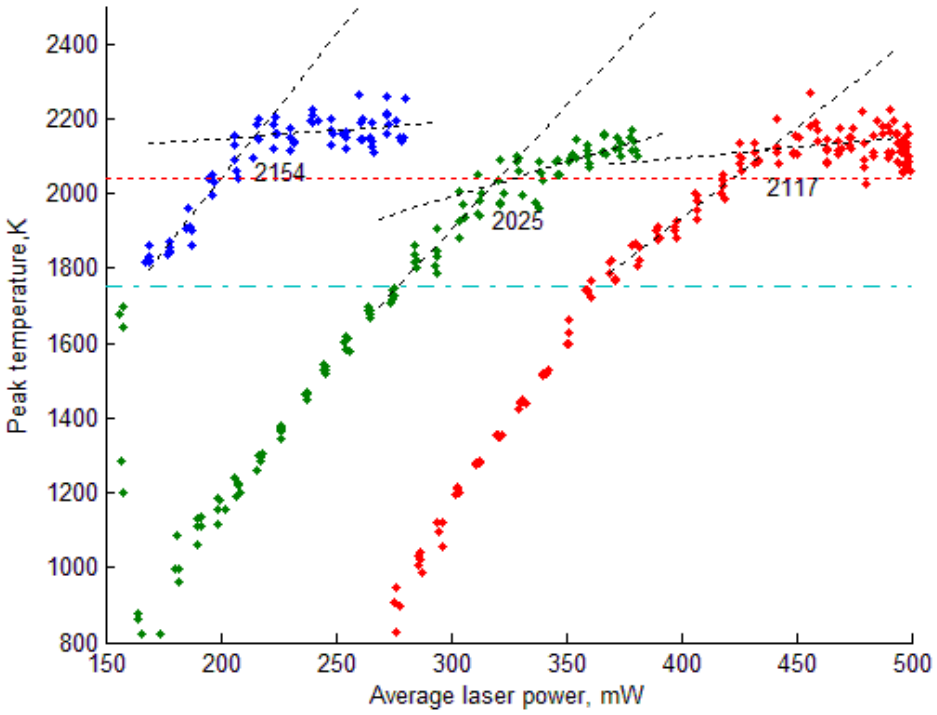

Figure 3.4 The peak temperature as a function of average laser power for three successive cycles of heating at the same spot. Melting plateaus are clearly observed. Dashed lines are linear fits to the data. Curves are offset along x axis for clarity. Numbers indicate intersections of the linear trends.

At ambient pressure platinum has a positive, 12% discontinuity of emissivity at the melting [9]. The increased emissivity has a competing effect with latent heat of melting: increase of emissivity causes corresponding positive change in the slope of the heating curve for these timescales [10], while the latent heat should decrease the slope after melting by 50% according to finite element analysis. These two contributions should partially cancel each other. We observe a much more dramatic change, averaging to 75(11) % reduction of the slope. This indicates that surface reconstruction and dynamics of the melt define the behavior in this regime (rather than effects considered in [10] and [11]). One of the possible explanations is the feedback caused by laser light interference due to scatter off deformed surface [12]. In the case of large uniform laser beams this mechanism will cause formation of periodic ripples on the surface of metal.

Despite strong morphology changes and non uniform heating, the temperature determined is within 100 K of the platinum melting point in the worst case, and is much better on cool down when

simultaneous growth of the modified region does not affect the temperature determination. The sign of error is expected – the melting temperature was overestimated likely due to the presence of hot spots – individual globules as seen on the SEM image would not have as good thermal anchoring as the bulk of platinum and can offset to higher temperature at the time bulk melting occurs.

Since hydrogen experiments are performed at lower temperatures and no irreversible changes are observed in the absorber at heating, we conclude that platinum is a suitable absorber material for the wavelength and temperature range of the hydrogen experiment. This does not rule out hydride formation which might have a different emissivity evolution, but given that it is a reasonably good metal [13], its emissivity can be described by the Hagen Rubens relation for emissivity: $\epsilon = 2\sqrt{2\omega\epsilon_0\rho}$, where ω is the angular frequency of light, ϵ_0 - dielectric constant of vacuum and ρ is the electrical resistivity. For this functional dependence we do not expect dramatic changes in $d(\log(\epsilon))\Big/_{d(\lambda^{-1})}$ with temperature, which is the error source for the type of fitting we do.

3.6 Conclusion

In this chapter we report an observation of the surface reconstruction effect for platinum significantly below the melting temperature. An effect like this can be detrimental for accurate melting temperature estimation if speckle motion or change in sample surface morphology are used as criteria of the transition. The proposed mechanism of the surface reconstruction is the optical feedback increasing laser absorption due to damage of the platinum surface.

We show that platinum can be used as an absorber for the region of temperatures of the interest for the hydrogen liquid-liquid phase transition. Specifically, platinum spectral emissivity temperature change is uniform enough to allow accurate pyrometric temperature determination.

We demonstrate that the method we used for the determination of LLT in hydrogen works at least on one system other then hydrogen. Furthermore the method is robust enough so the strongly modified surface does not significantly affect the determination of the bulk melting temperature.

Even though the temperature of the surface reconstruction is comparable with the measured temperature of the hydrogen LLT, we do not expect that a similar effect took place in our hydrogen laser heating experiment. The evidence for this claim is that we do not observe strong irreversible changes in the sample emissivity. Possible reasons for the absence of the reconstruction in the cell are (a) the melting temperature of platinum is substantially higher at this pressures (more than 1000 K increase compared to ambient pressure value, according to [14]) and (b) hydrogen can hydrodynamically stabilize the fluctuations of the molten surface shape which probably lead to the optical feedback and observed surface reconstruction.

3.7 Bibliography

[1] D. Errandonea, B. Schwager, R. Ditz, C. Gessmann, R. Boehler and M. Ross, "Systematics of transition-metal melting," *Phys. Rev. B,* vol. 63, no. 13, p. 132104, Mar 2001.

[2] A. Dewaele, M. Mezouar, N. Guignot and P. Loubeyre, "High Melting Points of Tantalum in a Laser-Heated Diamond Anvil Cell," *Phys. Rev. Lett.,* vol. 104, no. 25, p. 255701, Jun 2010.

[3] F. Datchi, P. Loubeyre and R. LeToullec, "Extended and accurate determination of the melting curves of argon, helium, ice H2O,and hydrogen H2," *Phys. Rev. B,* vol. 61, no. 10, 2000.

[4] M. Eremets and I. Troyan, "Evidence of maximum in the melting curve of hydrogen at megabar," *JETP Letters,* vol. 89, no. 4, pp. 174-179, 2009.

[5] D. Santamaria-Perez, G. D. Mukherjee, B. Schwager and R. Boehler, "High-pressure melting curve of helium and neon: Deviations from corresponding states theory," *Phys. Rev. B,* vol. 81, no. 21, p. 214101, Jun 2010.

[6] E. A. Murphy, *Experimental Studies of Surface Melting and Time-Resolved Superheating of Metal Surfaces, thesis,* 1993 .

[7] S. Rekhi, J. Tempere and I. F. Silvera, "Temperature determination for nanosecond pulsed laser heating," *Review of Scientific Instruments,* vol. 74, pp. 3820-3825, 2003.

[8] J. Frohh, J. Reynolds and T. Engel, "Surface morphology changes upon laser heating of Pt(111)," *Surface Science,* vol. 320, no. 1, p. 93–104, 1994.

[9] C. Cagran, B. Wilthan and G. Pottlacher, "Optical properties (at 684.5 nm) and radiance temperatures at the melting point of group VIIIb transition metals cobalt, nickel, palladium, and platinum," *High Temperatures - High Pressures,* vol. 35/36, no. 6, p. 667 – 675, 2003/2007.

[10] Z. M. Geballe and R. Jeanloz, "Origin of temperature plateaus in laser-heated diamond anvil cell

experiments," *J. Appl. Phys,* vol. 111, no. 12, p. 123518 , 2012.

[11] J. A. Montoya and A. F. Goncharov, "Finite element calculations of the time dependent thermal fluxes in the laser-heated diamond anvil cell," *J. Appl. Phys.,* vol. 111, no. 11, p. 112617 , 2012.

[12] Z. Guosheng, P. M. Fauchet and A. E. Siegman, "Growth of spontaneous periodic surface structures on solids during laser illumination," *Phys. Rev. B,* vol. 26, no. 10, p. 5366–5381, 1982.

[13] K. Ohta, *Private communication with I. Silvera.*

[14] A. Kavner and R. Jeanloz, "High-pressure melting curve of platinum," *Journal of Applied Physics,* vol. 83, pp. 7553-7559, 1998.

[15] J. Ruiz-Fuertes, A. Karandikar, R. Boehler and D. Errandonea, "Microscopic evidence of a flat melting curve of tantalum," *Physics of the Earth and Planetary Interiors,* vol. 181, pp. 69 - 72, 2010.

[16] R. Boehler, "Laser heating in the diamond cell: techniques and applications," *Hyperfine Interactions,* vol. 128, no. 1-3, pp. 307-321, 2000.

4 Gasket Indentation for Diamond Anvil Cells

4.1 Introduction

The diamond anvil cell (DAC) revolutionized high pressure physics and it was the gasketed DAC that enabled great advances. In a structurally high quality DAC with well-aligned defect free diamonds, the design and fabrication of the gasket is crucial for achieving the highest pressures. An example of a gasket between two diamond anvils is shown in Fig. 4.1. The diamond anvils generally have a small diameter flat ranging from ~30 to 200 μm at the culet with a small bevel angle of several degrees to a radius of a few hundred microns, then a steep angle at the pavilion of the diamond. A gasket must be a hard tough material with a high yield strength, yet ductile enough to undergo large plastic deformation without fracture. For the pressure to increase with increasing force (load) between the diamonds the volume of the hole must decrease when the diamonds are loaded. If the gasket is softer than the material being pressurized it will expand. In principle, for a uniformly loaded gasket infinite in two dimensions, the hole diameter will decrease with increasing load. However, the situation in a DAC is far different as the loading surface is comparable to the gasket hole size, and as the gasket is deformed under load, material flows radially both in and out. A general rule of thumb for the gasket hole to close under load and thus increase the sample pressure, derived from experience or finite element analysis [1] [2], is that the hole diameter in the gasket should be no more than half the diameter of the culet flat and the thickness should be about half the diameter of the hole or less. These conditions are important for achieving high pressures, in particular if the sample or pressurization medium is highly compressible such as helium or hydrogen for which the molar volume changes by around an order of magnitude at a megabar. Furthermore it is important that the gasket hole is well centered on the culet flat indentation, or it will most likely blow out as pressure is increased. Thus, in particular for achieving extreme conditions, the gasket must be well designed.

The general procedure in preparing a high pressure run is to mount and align the diamonds in a DAC, pre-indent the gasket by squeezing between the two anvils, and bore a hole in the gasket centered at the indentation of the culet flat (for example, this can be done either by electric discharge machining,

laser drilling, mechanical rotary drilling or focused ion beam; we shall call this drilling). One then mounts the gasket, loads the cell, and proceeds with the measurements of the sample under pressure. A crucial and vital part of this procedure is the preparation of the gasket, which eventually has the form shown in Fig. 4.1. For high pressure runs one might start with a gasket blank that is a few hundred microns thick and aim for a final thickness of 10-20 microns.

Usually, pre-indentation is a blind procedure, as one has a goal of pre-indented gasket thickness (at the culet flat) and generally this is only accurately determined after pressing by drilling a hole and measuring the thickness. There are other methods of estimating the gasket thickness before drilling the hole, but most of these depend upon a database founded on experience: number of turns of a screw, load, etc. The database needs to cover all the combinations of the gasket material and initial thickness, diamond culet dimensions, etc. It is worth noting that the number of indentation attempts should be minimized – diamonds can fail during this step, because the radial extrusion of the gasket material puts maximum tensile stress on the anvil tips [3]. Additionally, the usual approaches of predicting the gasket thickness do not work satisfactorily when the gasket is indented in more than one step - e.g. a composite gasket.

In this paper a method is presented to accurately (to within a micron) determine the thickness of the gasket under load while indenting it, independent of the gasket nature. It allows indentation of a gasket to a desired thickness without risky trial and error or prior experience with the specific gasket material. Information about the current gasket thickness is also useful for diagnosing different fault conditions (gasket cracking, friction or partitioning of applied load between the gasket and other regions, etc). During the indentation two variables are monitored - the load applied to the DAC and the drive that translates the diamonds towards each other, as if the gasket was absent. If a lead screw is used to generate the load in the DAC then the latter variable is simply the lead screw angle of rotation. The separation of the diamonds is then calculated using a simple mechanical model of the cell.

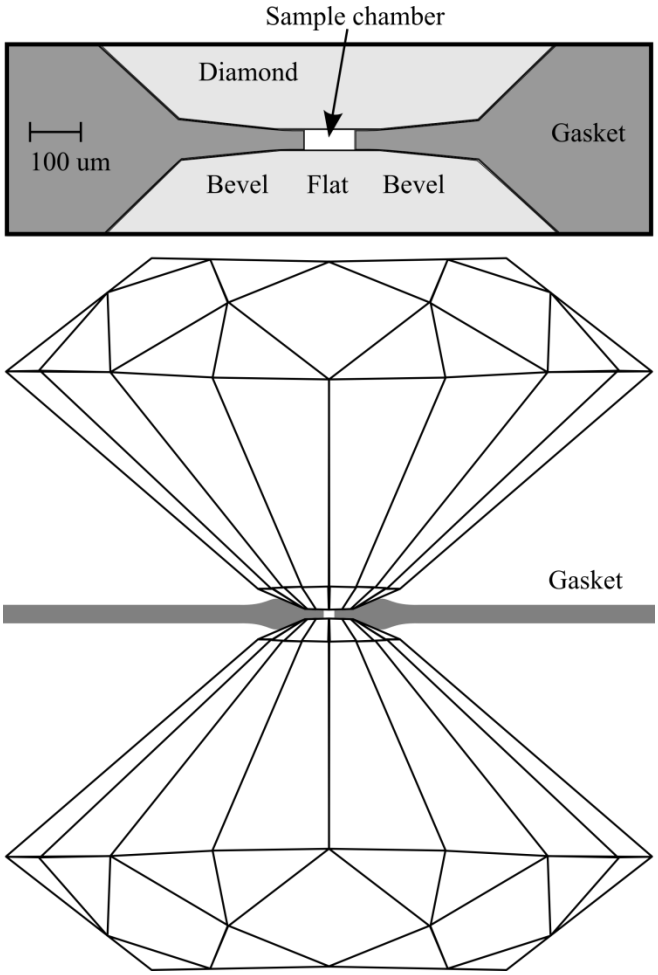

Figure 4.1 A overall view and a close up of a gasket pressed between two diamonds with an unreformed sample chamber. The latter is to scale.

A DAC is similar to a micrometer in that a coarse, easily measurable rotation of a lead screw results in a fine motion of the anvils[3]. Thus, monitoring the turns of the lead screw should be a precise way to measure inter-diamond separation when there is no load applied to the diamonds. An important distinction between a micrometer and a DAC is that while the former is rigidly built so that yield of the micrometer under load does not affect the measurement, the latter cannot be assumed rigid in the load range of interest. Therefore to use a cell as a micrometer one needs to know the load applied to the sample and mechanical properties of the DAC, so that the yield of the cell is known and can be used to correct the

[3] Even though in a typical DAC diamond flat tips are as small as hundreds of microns a significant load is required to achieve megabar range pressures. In the case of diamonds with 100 μm flats and 300 μm bevels the load to get to one megabar is ~ 4 kN. Since most cells can be hand operated one needs a good mechanical advantage to generate this range of loads.

"micrometer reading" indicated by the lead screw advance. In Fig. 4.2 we show a micrometer and the type of cell that we shall use to demonstrate our technique.

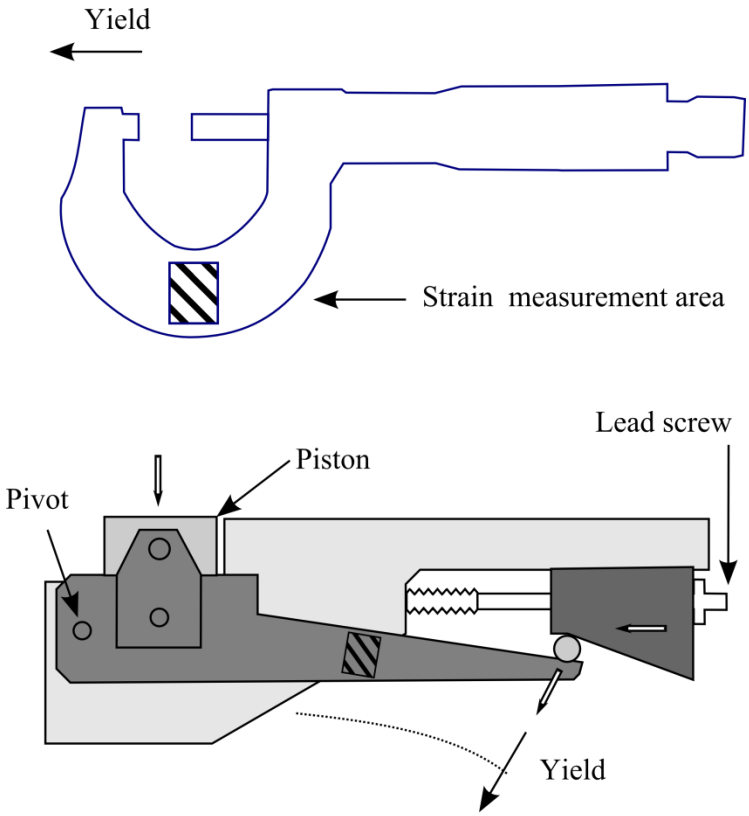

Figure 4.2. Schematic drawing of a micrometer and a diamond anvil cell. Hollow arrows indicate direction of motion when the cell is closed. Hatched area is where the strain measurement is done. The diamond anvils, as shown in Fig. 4.1, are inside the cell below the piston whose downward motion translates them together.

4.2 Implementation and test

The DAC that we shall use to demonstrate the technique is a piston cylinder type with a lead screw and elastic lever arm for load generation, made of unhardened vascomax steel, shown in Fig. 4.2. One rotation of the lead screw translates the lower diamond a distance of 67 microns, which is equivalent to ~300 turns per inch (compare to 50 TPI thread for most micrometers). Because of this ratio a standard 10 turns electronic potentiometer rotator with a hundred divisions per revolution can easily be attached to the lead screw and used for measuring the rotation. A precision of 0.67 μm is achieved for translation and is adequate for system accuracy.

To measure the load a Wheatstone Bridge is utilized: a half-bridge configuration of 350 ohm strain gauges was used on one of the cell arms with one gauge under compressive load and the other stretching (tensile). Given the flexibility of the lever arm, 1 μStrain corresponded to about 1.6 μm effective yield of the DAC, on average.

The DAC stiffness/compliance curve was determined. This required knowing the inter-diamond separation for a range of loads and lead screw positions. Since the diamonds are aligned with parallel culet flats, they form a Fabry-Perot interferometer. A transmission spectrum can be measured to provide a precise measurement of the diamond separation down to a spacing of several microns. Given that the diamonds are usually mounted on tungsten carbide (WC) seats, one can use a hollow steel or brass cylinder that presses against the seats, rather than the diamonds. We calibrated the following simple model:

$$d = d(L, \alpha) = d_0 - A\alpha - c(L) \tag{4.1}$$

where d is the inter-diamond separation, α - lead screw angle, A and d_0 are constants and $c(L)$ is the DAC yield as a function of load, L. The constant A is an a measure of the diamond advance per a unit of lead screw rotation angle and d_0 is the initial diamond separation for no load and lead screw at 'zero' angle. We chose to parameterize $c(L)$ as a polynomial of 5th order

$$c = \sum_{n=1}^{5} c_n L^n \tag{4.2}$$

and use a ordinary least squares fit to estimate all 7 parameters of the model. The polynomial is a property of the DAC and once measured can be used reliably for future pre-indentations.

To obtain micron level precision one must take into account the yield of the diamond anvils, which is not insignificant and is a fairly linear function of the load in this regime, as confirmed with finite element analysis (FEA). In order to determine this we used a drilled gasket so we could measure the diamond separation while loading by observing fringes. This resulted in just one cycle of diamond loading every time the diamonds were changed. Experience shows that different sets of diamonds with the

same flat/bevel sizes deform in the same way. Later it is described how this step was handled in our implementation.

The calibrated DAC was tested on different pre drilled gaskets and spacers and found to behave satisfactorily over a wide range of thicknesses and loads. The main sources of uncertainty were identified: temperature stability of the cell/ strain gauge, possible contamination of mating flat surfaces the cell which shifts diamonds and the long term (weeks) drift of the cylinder-piston friction.

All three of the above result in variation of the d_0 term with time. It is possible to control all of these factors independently, but what we have found to be an easier solution is to use a 'dummy gasket' before the actual indentation to measure the current value of d_0. The dummy gasket is a gasket of some thickness around the target value with a hole in it (these are generated more often than one would want as a result of errors in sample preparation downstream from indentation, say off center hole). It is used as follows: before indenting the actual gasket, a dummy gasket is placed in the cell, loaded, and the $\{d, \alpha, L\}$ triplet is measured to determine the current value of d_0. The precise value of the dummy gasket thickness or load does not matter. It is convenient to keep this load to a fraction of the actual indentation load, so the dummy gasket hole does not collapse and the gasket can be reused. Offsets we were getting were of the order of couple microns and when taken into account brought the total uncertainty of gasket thickness down to under 1.5 micron.

For multi-megabar studies, where diamonds normally only survive one loading, this step can be combined with the above mentioned calibration of diamond elastic deformation. To do this one measures the $\{d, \alpha, L\}$ triplet for several values of load and updates values of d_0 and c_1. In the implementation used in our lab, this step was handled by manually entering corrections δd_0 and δc_1 into a spreadsheet while visually observing the results on a deviation plot $\delta d = d_{Fabry-Perot} - d(L, \dots)$.

It is worth noting that in this configuration cylinder/piston friction does not significantly affect the estimation of the gasket thickness because it is absorbed into the DAC model as a constant term

(compression of cylinder because of the constant extra load). However in the case of change of friction over time this constant can change as well, but our experience is that under normal operation cell friction does not change much.

A gold layer of ~20 nm thickness sputtered on a rhenium gasket blank reduced the indentation load by ~20% to get the desired final thickness (Fig. 4.3). A major benefit of reduced friction on the diamond - rhenium interface is that diamond anvils are not subject to aggressive tensile loading which is thought [3] to be a contributing factor to early diamond failure. It may be even more important for experiments on hydrogen because of the belief that hydrogen embrittlement of the diamond anvils is caused by hydrogen diffusing into anvils through surface and sub-surface defects.

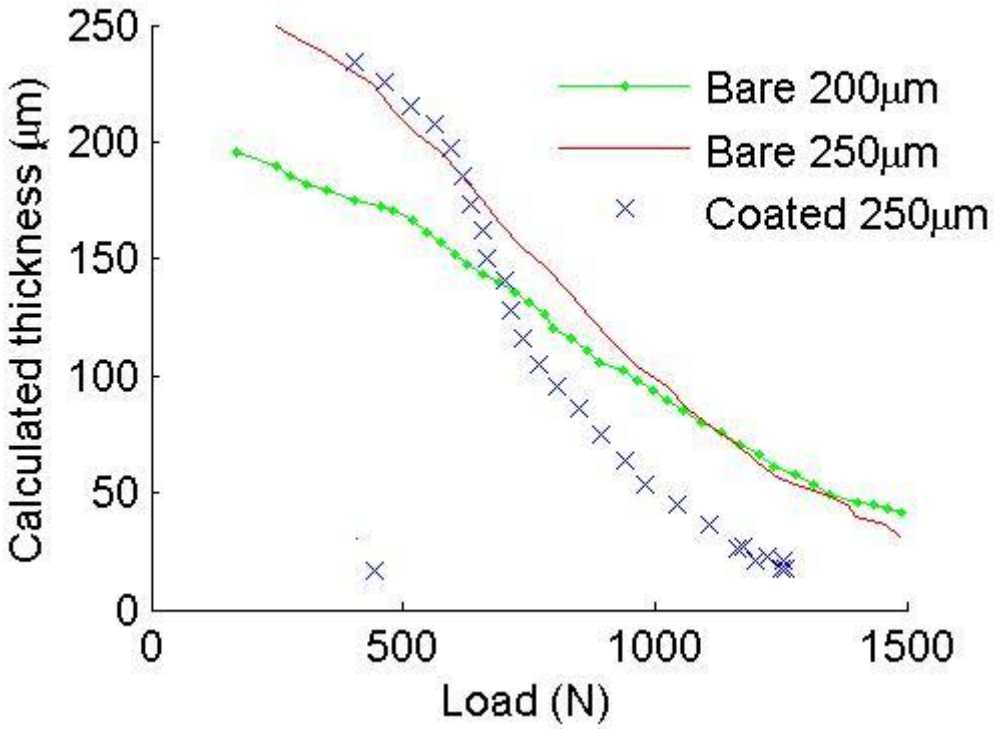

Figure 4.3 Three typical load vs gasket thickness curves. Two curves for bare rhenium gasket blank show convergence to universal behavior at higher load. The curve for gold plated gasket with initial thickness of 250 micron shows rapid indentation.

The gold layer which is helpful during indentation can be detrimental during the run because of its "lubricating" qualities. In a high pressure run it is desirable to have a no-slip condition between the

gasket and the diamond; slippage can lead to gasket blow-out. In order to increase stability against blow-out of the sample we removed gold residuals from gasket by sonicating it with 5 μm alumina powder in water. When a gold coating was reapplied to an indented gasket we had systematic hydrogen sample blowout for pressures under 1 megabar; without extra gold pressures exceeding 1.6 megabars were achieved without a sign of instability.

4.3 Conclusion

We present a simple method of controlled indentation of a gasket for use in DAC. It allows using uncalibrated gasket stock material, indentation of composite gaskets or gaskets with slippery surfaces whose load-indentation depth curve can vary. We tested this method on cells of a specific design used in our laboratory, but it can be applied to a wide variety of cells where the load can be measured. Using this method we successfully indented multiple gaskets to thicknesses in the range 15 to 25 um within 1.5 μm of target thickness using different gasket stock materials.

4.4 Acknowledgment

We thank Evgeniya Zarechnaya and Goutam Dev Mukherjee for useful discussions and encouragement.

4.5 Bibliography

[1] K. S. Chan, T. L. Huang, T. A. Grzybowski, T. J. Whetten and A. L. Ruoff, "Pressure concentrations due to plastic deformation of thin films or gaskets between anvils," *Journal of Applied Physics,* vol. 53, pp. 6607-6612, 1982.

[2] J. Orloff, C. Narayana and A. L. Ruoff, "Use of focused ion beams for making tiny sample holes in gaskets for diamond anvil cells," *Review of Scientific Instruments,* vol. 71, pp. 216-219, 2000.

[3] R. Miletich, D. R. Allan and W. F. Kuhs, "High-Pressure Single-Crystal Techniques," *Reviews in Mineralogy and Geochemistry,* vol. 41, pp. 445-519, 2000.

5 Pressure-Induced Metallization in GeO

5.1 Introduction

Divalence of chalcogens in IV-VI compounds gives rise to the electronic configuration called the lone pair defined as a valence electron pair without bonding or sharing with other atoms. It makes these compounds favorable candidates for insulator to metal transition [1] [2]. These materials have been studied extensively with the exception of SiO and GeO which are both metastable amorphous solids at ambient pressure. SiO was recently shown to undergo an insulating to metal transition at the modest pressure of 12 GPa. In this chapter we report that GeO undergoes the transition as well and remains an amorphous metal after the pressure was released.

5.2 Experimental

Temperature dependant electrical resistance measurements and X-ray scattering on GeO were carried out using a diamond anvil cell (DAC) with 600 μm culets. We used a T301 stainless steel gasket, indented to 60 μm thickness and a sample cavity of 200 μm diameter. The ruby fluorescence method was used to measure the pressure. Conductivity measurements were carried out using a sandwiched gasket [3]. We bonded two back-to-back preindented 125 μm thick T301 steel gaskets separated by 25 μm mica sheet using Lord 320 epoxy. A scale drawing of the gasket is shown in Fig. 5.1. A cavity was drilled through the gasket, and copper electrodes were welded to the upper and lower layers in a two point probe configuration. The GeO powder sample was obtained from Chemical and Technical Developments Ltd.

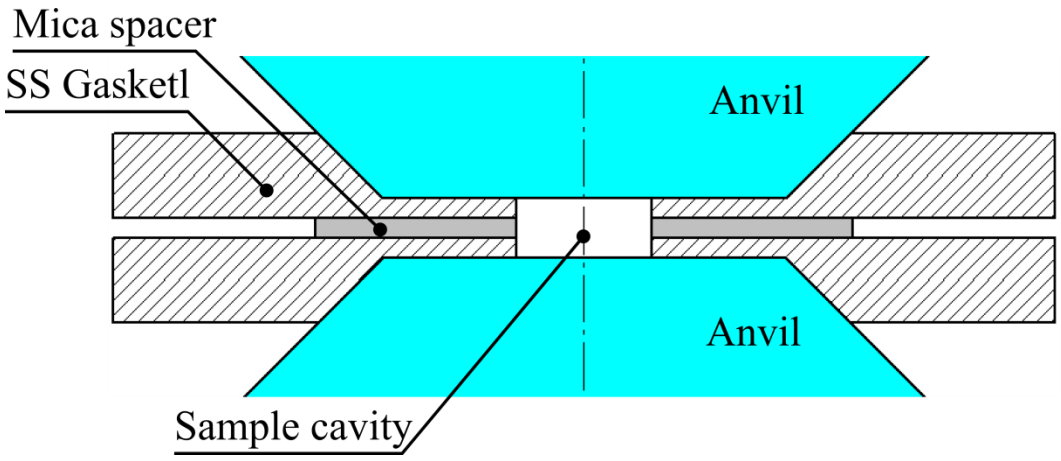

Figure 5.1 Laminated gasket geometry. Scale drawing.

The DAC was mounted in a liquid nitrogen cooled cryostat that enabled the temperature range 80 to 300 K to be spanned for each isobar. Resistance was measured with a Keithley source-measurement unit Model 617 applying constant voltage of alternating polarity and measuring current. In the high resistance region typical voltage values were 500mV.

A dramatic drop in resistance from 100 GOhm to less than 1 ohm in the pressure range 0 to 12.5 GPa was observed. Over this range there is a change in temperature dependence of resistance from steep, exponential thermally activated behavior $\frac{dR}{dT} < 0$ to shallow, $\frac{dR}{dT} > 0$ shown in the Fig. 5.2. Once the transition happens it does not reverse after removal of pressure, at least within a couple of months, thus it is metastable. Measurements were carried out using both an ethanol- methanol pressure medium and no pressure medium; the behavior is not affected. The absolute value of resistivity is not reported because it difficult to estimate due to the unknown cell geometric constant. Furthermore, the cell constant changes with pressure as the sample is deformed. Absolute values of room temperature resistance are roughly 100G, 30M 200K and 500 ohm for 0.5, 4.2 7.7 and 11 GPa correspondingly; see Fig. 5.3.

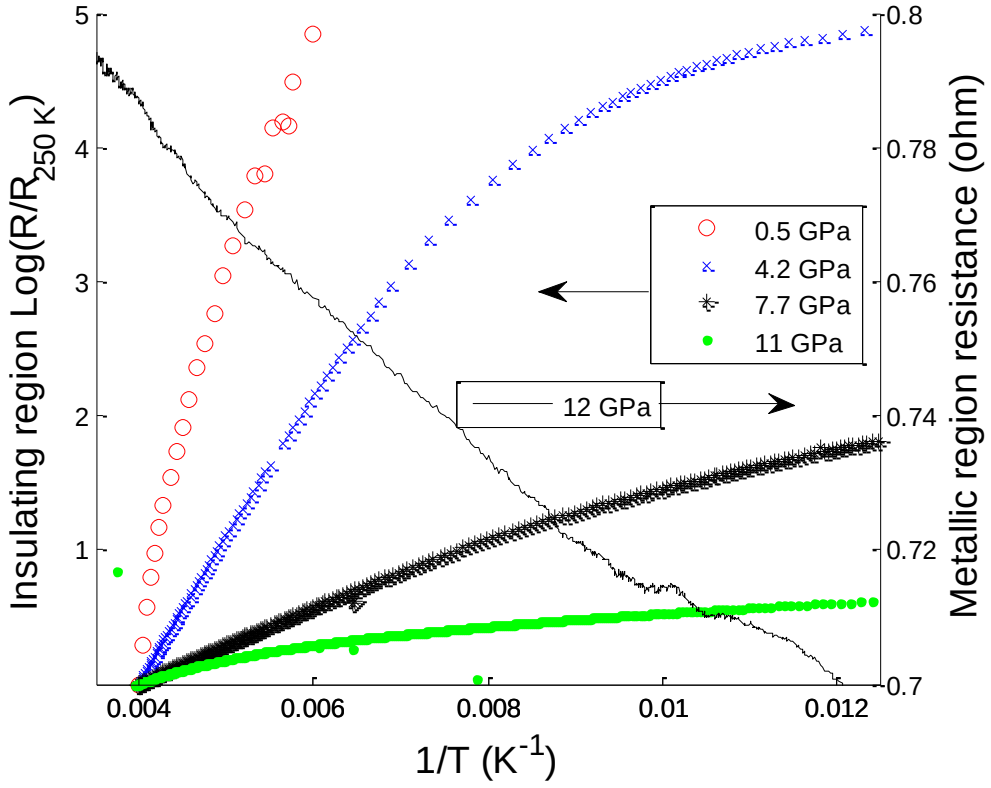

Figure 5.2 Temperature dependence of GeO electrical resistance normalized at 250 K. The 11 GPa curve is scaled by x10. The continuous black thin line corresponds to the metallic state.

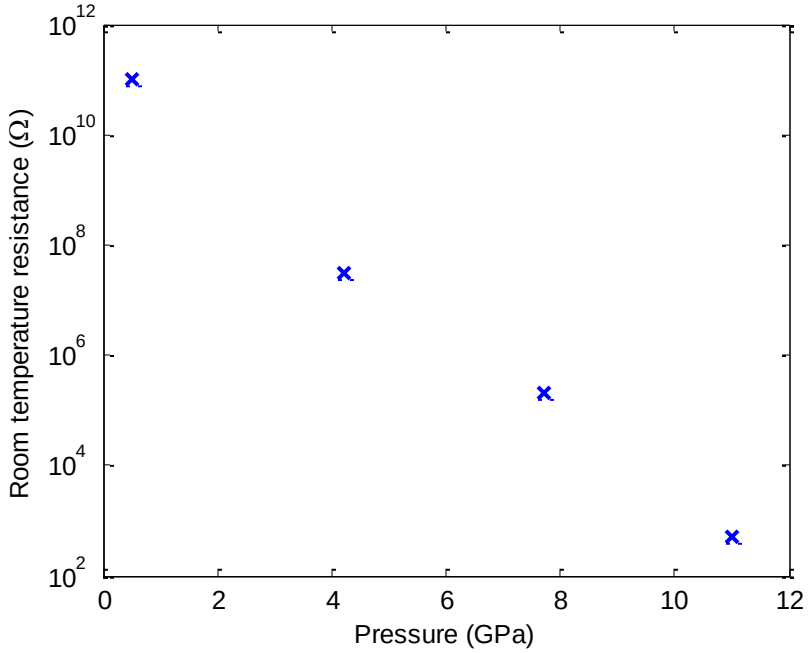

Fig 5.3 Pressure dependence of the sample resistance

The resistance measurements were carried out using a 2-probe method, thus stainless steel gasket resistance might dominate the sample resistance in the metallic phase. We did not observe saturation of resistance at temperatures less than 100 K, which is typical for stainless steel; instead the resistance keeps decreasing below 100 K. We conclude that the observed metallic type temperature dependence is characteristic of the GeO sample, rather than an artifact caused by gasket shorting or gasket resistance itself.

After one of the runs the GeO sample was recovered and removed from the gasket. The high conductivity was confirmed, with absolute resistance of a couple of ohms which is strikingly different from the pre – pressurization value, on the scale of hundreds of mega ohms. This rules out possible gasket short as the explanation of the hysteresis.

X-ray data were collected at 23 GPa. Zero pressure data is from [4]. XRD in a DAC is done with a molybdenum anode, monochromatic at 0.7106 A [5]. For easier comparison with the zero pressure data, the 23 GPa data was converted to be read as if the XRD was taken with a copper anode, monochromatic at 1.5405. As typical for non crystalline materials, continuous scattering patterns with no diffraction peaks were obtained for both pressures. The scattered intensity versus scattering angle curves are shown in Figure. 5.4

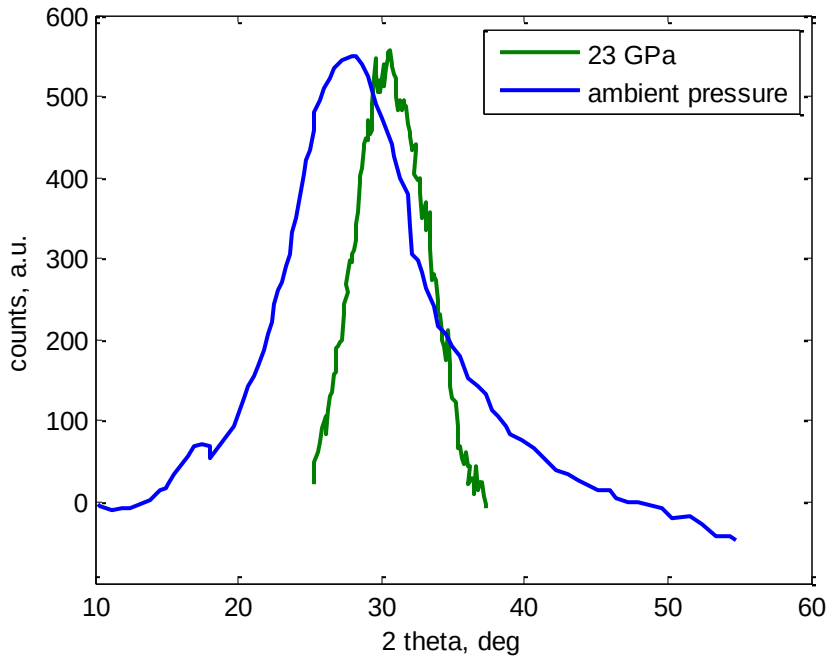

Figure 5.4 X ray scattering patterns for GeO at ambient pressure and 23 GPa

5.3 Discussion

A gradual change in the temperature dependence of GeO resistance is observed, which is different from SiO [2] where essentially no change in the exponent can be observed from 5 to 10 GPa. Figures 5.2 and 5.5 show the variation of the temperature dependence of resistance with pressure for GeO and SiO to illustrate this. No thermoresistance data is available for SnO. However the evolution of the electron band structure with gradual band gap closure described in [6] would yield a behavior similar to that observed in GeO. Furthermore, on pressure cycling SnO exhibits hysteresis in resistance and structure [7]

Although the electron band structure argument of [6] is not applicable to GeO because of the amorphous state of GeO, the similar gradual crossover of the resistance exponent suggests that hybridization of germanium 4s2 lone pair and oxygen 2p states might take place which is different from the metallization mechanism of SiO proposed in ref. [2]

In conclusion we report the observation of an insulator to metastable metal transition in GeO which has characteristics similar to the IM transitions in SnO and SiO yet not identical to either. Further measurements covering lower temperatures and using different sample geometry (4-probe) are needed to

characterize the region near the transition and the metallic phase. This will allow the measurement of the resistance of the metallic GeO rather than gasket and determine the resistance exponents near the transition, potentially clarifying conduction mechanisms.

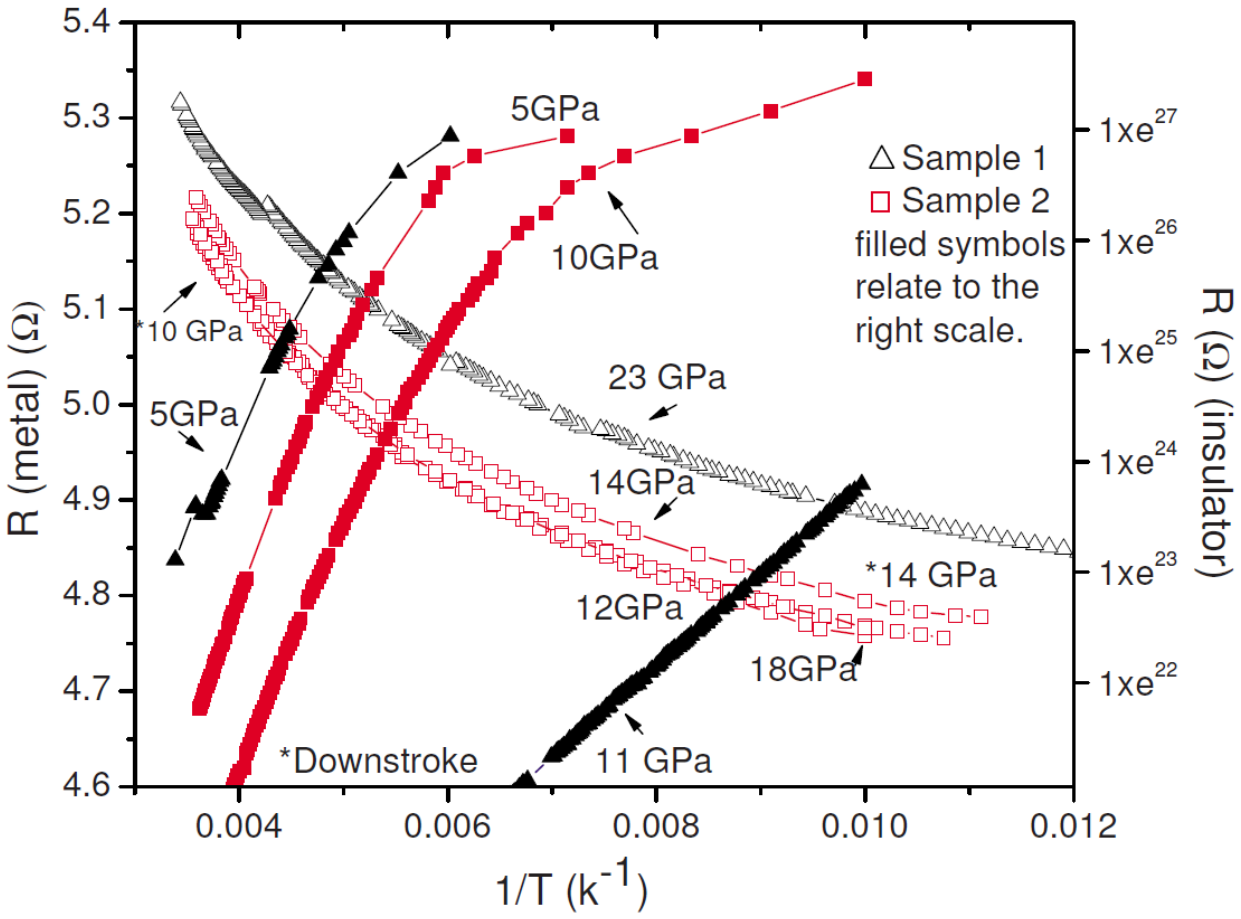

Figure 5.5 Temperature dependence of SiO electrical resistance.

5.4 Bibliography

[1] E. Sterer, *M.Sc. thesis,* Tel-Aviv University, 1989.

[2] A. Pesach, R. Shuker and E. Sterer, "Pressure-induced insulator to metal transition in amorphous SiO," *Phys. Rev. B,* vol. 76, no. 16, p. 161102, Oct 2007.

[3] D. Leong, H. Feyrit, A. D. Prins, V. A. Wilkinson, K. P. Homewood and D. J. Dunstan, "Laminated gaskets for absorption and electrical measurements in the diamond anvil cell," *Review of Scientific Instruments,* vol. 63, pp. 5760-5763, 1992.

[4] A. Pesah, *Thesis.*

[5] E. Sterer, *performed at Nuclear Research Center – Negev Beer-Sheva, Israel.*

[6] N. E. Christensen, A. Svane and E. L. Peltzer y Blanca, "Electronic and structural properties of SnO under pressure," *Phys. Rev. B,* vol. 72, no. 1, p. 014109, Jul 2005.

[7] E. Sterer, A. Pesah, A. Melchior and C. Marini, *EXAFS study on an electronic transition in SnO;Experiment HS-4380,* Scientific report to ESRF, 2010.

6. Optical cryostat Based on Gifford McMahon Cryocooler

6.1 Introduction

The standard way of cryogenic studies of diamond anvil cells is to use a liquid helium/liquid nitrogen cryostat with an optical tail [1]. In this chapter we describe a system to use a so called cryogen free cryostat based on a Gifford McMahon cryocooler[4]. The principal problem with such cryostats is the large level of vibration that can be coupled to the sample. We present a design which can suppress the vibrations to an acceptable level.

The short working distance (50 mm, 0.25 NA) cryostat for the diamond anvil cell **(DAC)** is suitable for optical studies of samples down to 3 K without vibration decoupling and 15 K with a modification to suppress vibration coupling to the DAC. The **DAC** was described in [1]. With this system we use cryogenic loading of the sample into the DAC. A gaseous sample can be loaded into a cold DAC via a capillary by condensing to the liquid phase. The DAC pressure can be adjusted while the sample is in the cryostat. The system features a low level of vibration compatible with studies of micron size samples and can be built in a typical machine shop. The cryostat is made of all aluminum tubing, both rectangular and cylindrical, with no welds; all sections are epoxied together with vacuum tight seals. By using standard rectangular aluminum tubing in the optical tail, the window mounts can be very compact facilitating the short working distance.

6.2 Cryostat construction

The cryostat is designed around a two-stage Sumitomo cryocooler[1] operating on the Gifford McMahon cycle. It was designed and tested a few years earlier, and often used for cryogenic loading of DACs. It is shown in Fig. 6.1 without detail regarding the cell suspension. The outer body and the 30 K radiation shield are built from aluminum. There is a common vacuum space which prevents the use of exchange gas cooling but dramatically simplifies the construction. It is especially relevant for the vacuum

[4] RDK-408BW Cryocooler. Cooling power: 2nd stage 1. W at 4.2 K; first stage: 42 W at 40K

sealing of the optical windows, since only the room temperature window mount have to be made vacuum tight and this is done with rubber o-rings. To minimize the radiation load from the room temperature body to the T = 30 K radiation shield, the inside walls of the cryostat were covered with very smooth aluminum foil tape which has higher reflectance then the aluminum body of the cryostat. The two vacuum tight joints (marked in Fig. 6.1) did not experience temperature cycling and were made using Lord 320/322 and Lord 305 epoxies. Ports into the cryostat were either epoxied or threaded and Teflon taped.

The DAC was originally rigidly mounted to the second stage flange (called the 4 K flange, but cools to ~3K with no thermal load) shown in Fig. 6.1. However, when the GM was operating the vibration amplitude of the DAC (~20 microns) was too large for measurements in the laser heating experiment. The DAC would remain at temperatures around 4 K for about 30-40 minutes, when the GM was turned off which might have been a sufficient solution to the vibration problem. However, when laser heating the sample, this time was severely reduced by a factor of 3-4. As the DAC and GM support heated, the sample would drift out of the focal region due to thermal expansion; this also prevented useful measurements. Thus, the design was modified to suppress the vibrations.

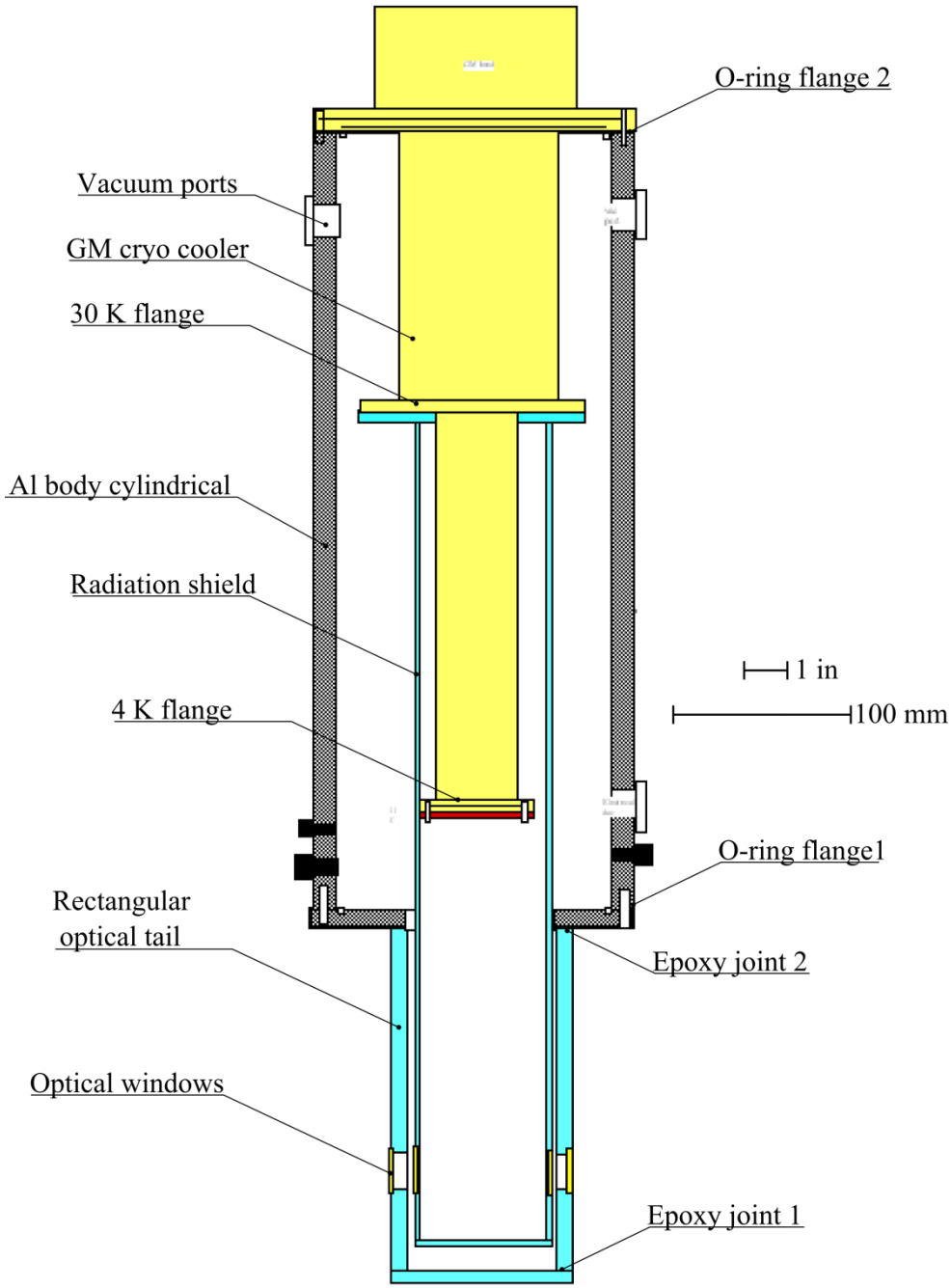

Figure 6.1: The aluminum cryostat with the Gifford McMahon cryocooler. The DAC is not shown here.

The Vascomax steel DAC was originally designed to be used with exchange gas cooling, however in this cryostat cooling was by conduction between metal parts. The low thermal conductivity of Vascomax at cryogenic temperatures results in a large temperature gradient from the region of the diamond to the cold flange of the cryocooler and the cooling rate is thermally bottlenecked. Therefore to efficiently cool it a copper plate was installed along the back and bottom surfaces of the DAC to improve

thermal contact and promote uniform and rapid cooling (see Fig. 6.2). The plate was screwed on and enhanced surface contact was made with vacuum grease, compatible with the temperature range of operation.

To minimize the optical working distance for optics external to the cryostat, both outer body and the radiation shield of the optical tail were made from square cross-section aluminum tubing. This allows installation of the flat optical windows mounted in the aluminum walls as opposed to a round cross-section of the cryostat body which requires special mounting fixtures that greatly increase the working distance. Both room temperature and 30 K windows were made of calcium fluoride, transparent out to $\lambda \sim 10\ \mu m$ in the infrared. The 30 K windows were thermally anchored to the aluminum radiation shield by vacuum grease and held in place by a thin metallic clamping sheet. Room temperature windows were sealed using neoprene o-rings.

To adjust the pressure in the DAC mechanical torque had to be transferred to the cold cell from outside. In a conventional cryostat a rotatable straight tubing along the axis of the cryostat can be used to adjust the pressure [1]. However the GM cryocooler does not have a clearance hole along its axis, therefore the torque had to be transferred along a curved path. A flexible steel drive shaft was used inside the cryostat for this purpose. A Wilson seal was used to bring the shaft through from outside to the vacuum. To couple the torque to the DAC without transmitting the GM vibration, a T shaped coupling was used which would only engage when the load is applied and can be backed off to disengage (see Fig. 6.3). A gearbox with ratio 1:2 was used on the cell to decrease the load on the shaft and to be able to change the pressure in finer increments.

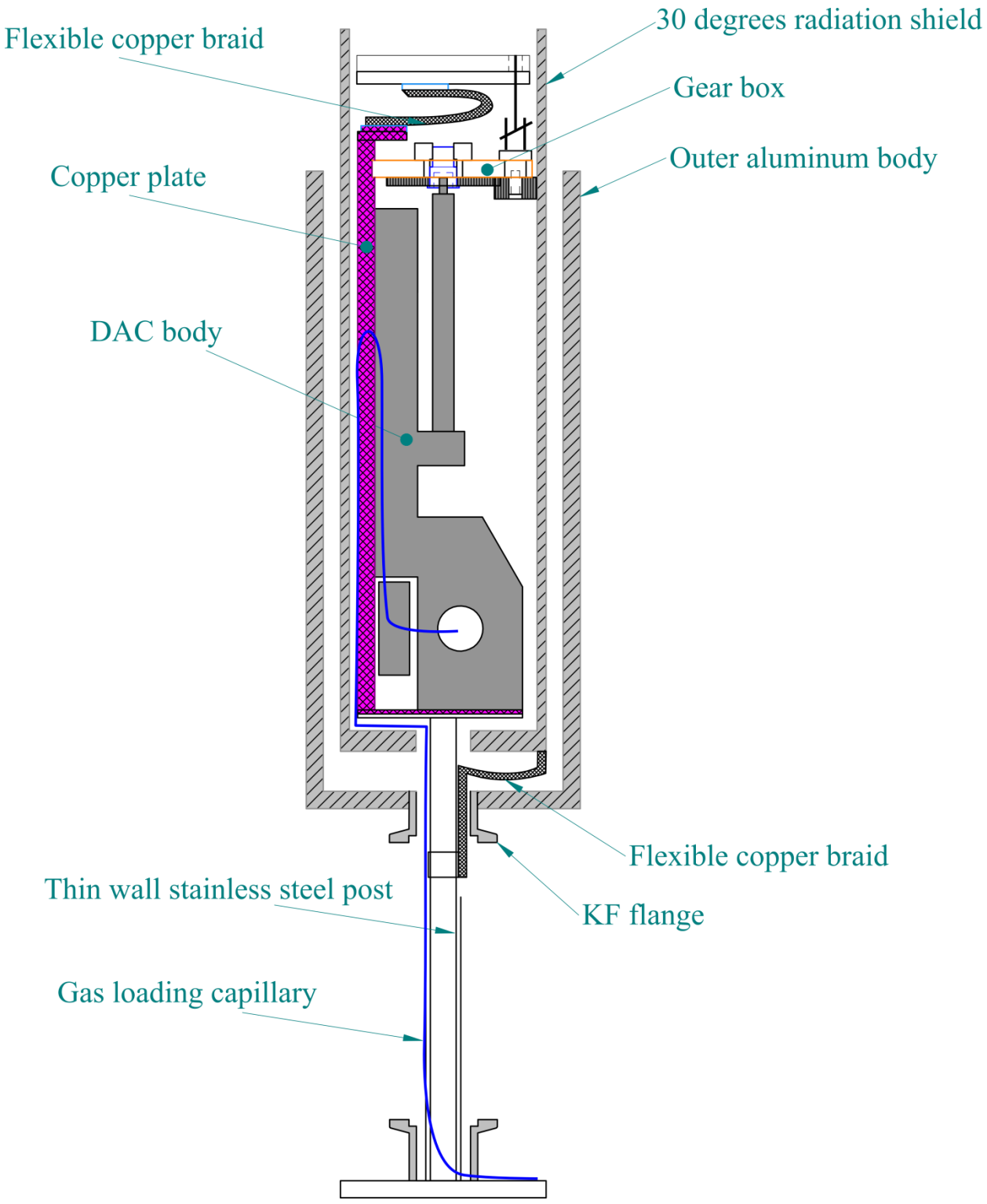

Figure 6.2: Vibration isolation of the cell side view. To scale.

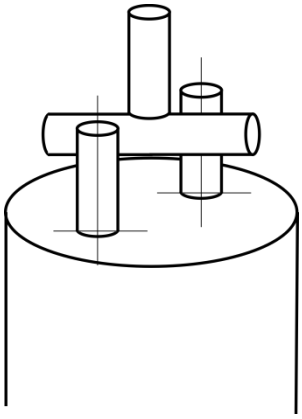

Figure 6.3: T-coupling for torque transfer, schematic

For each cool down the cryostat had to be assembled and evacuated. Total time for cryostat preparation was about one hour for assembly and a half hour for evacuation. The cooling time from room temperature to 15 K was about 5 hours. A typical cool down temperature trace is shown on the Fig. 6.4.

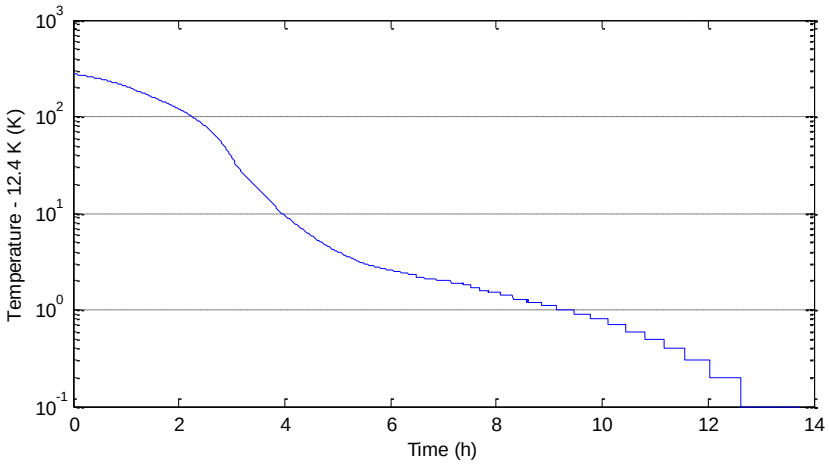

Figure 6.4: A typical cool down curve

6.3 Vibration management

During normal operation the GM cryocooler produces strong pulsed vibration at a ~1 Hz rate which interferes with optical measurements in the case of small samples. The elastic vibration amplitude of the sample when the DAC was rigidly mounted to the cold flange was about 20 microns - above the tolerance threshold for laser heating experiments requiring it to be less than several microns.

The goal was to decrease the transverse vibrations (with respect to the optical axis) of the sample to enable the optical studies of small samples. We designed an inverted pendulum support geometry where the cell rests on the thin wall stainless steel post mechanically attached to the massive optical table at room temperature (see Fig. 6.2). Thermal contact to the cell was via a flexible copper braid between the cold flange and the DAC. This provided good thermal contact and minimized the coupled vibration. Because of the shape of the displacement pulse of the cryocooler head (sharp spike once a second), the braid also performed a function of damping of the two lowest frequency transverse pendulum modes (7 Hz, Fig. 6.5, first and second from left) of the heavy cell during the rest of the cycle while the GM head was not moving.

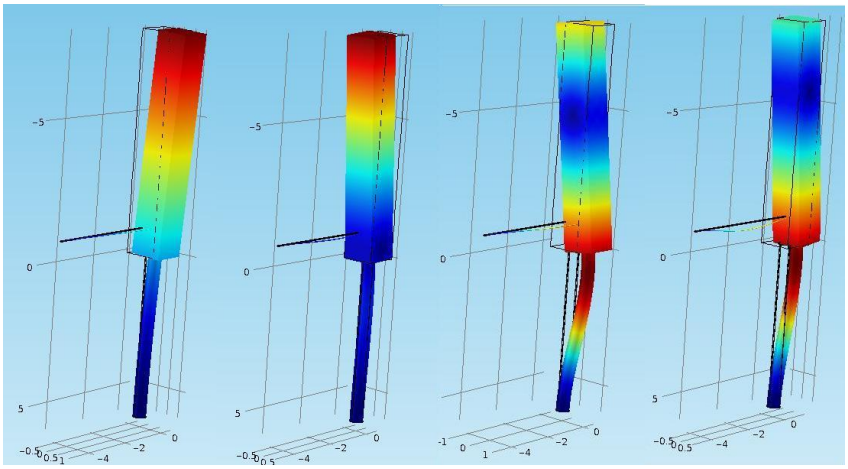

Figure 6.5: The lowest frequency modes of the cell vibration. Color codes the amplitude of displacement.

Although this new mounting substantially suppressed the vertical oscillation of the cell, the sharp mechanical spikes of the GM head could set the DAC into transverse vibration, still too large to tolerate. One of the next two lowest frequency transverse modes (bending of the post and rotating the DAC, Fig. 6.5, third from the left) was suppressed using a stainless steel rod, (2 mm diameter, 250 mm length) coming from room temperature and attached to the DAC body by a permanent magnet. A schematic drawing of the connection is shown in Fig. 6.6. The rod did not put a measurable heat load on the cell.

Both the bottom support tubing and the transverse rod passed through flexible brass bellows connected with quick connect KF flanges and shared the vacuum of the cryostat, shown in Fig. 6.6. Thus

although the cryostat with the GM head had large vertical vibrations due to the GM head, the DAC was essentially stationary, as the stainless steel tubing was clamped to the massive optical table. Very little vibration was coupled to the optical table but was absorbed in the bellows. The thin wall stainless steel tubing was thermally anchored midway to the 30 K radiation shield to absorb most of the thermal heat leak from the room temperature table and redirect it to the more powerful first stage; a flexible copper braid was used for this purpose. A thin wall stainless steel capillary used for loading gas samples into the DAC was wound along the DAC support post (shown in Fig. 6.2). The mini chamber described in the Laser Heating chapter was used to contain liquefied hydrogen and prevent degradation of the vacuum in the cryostat during loading.

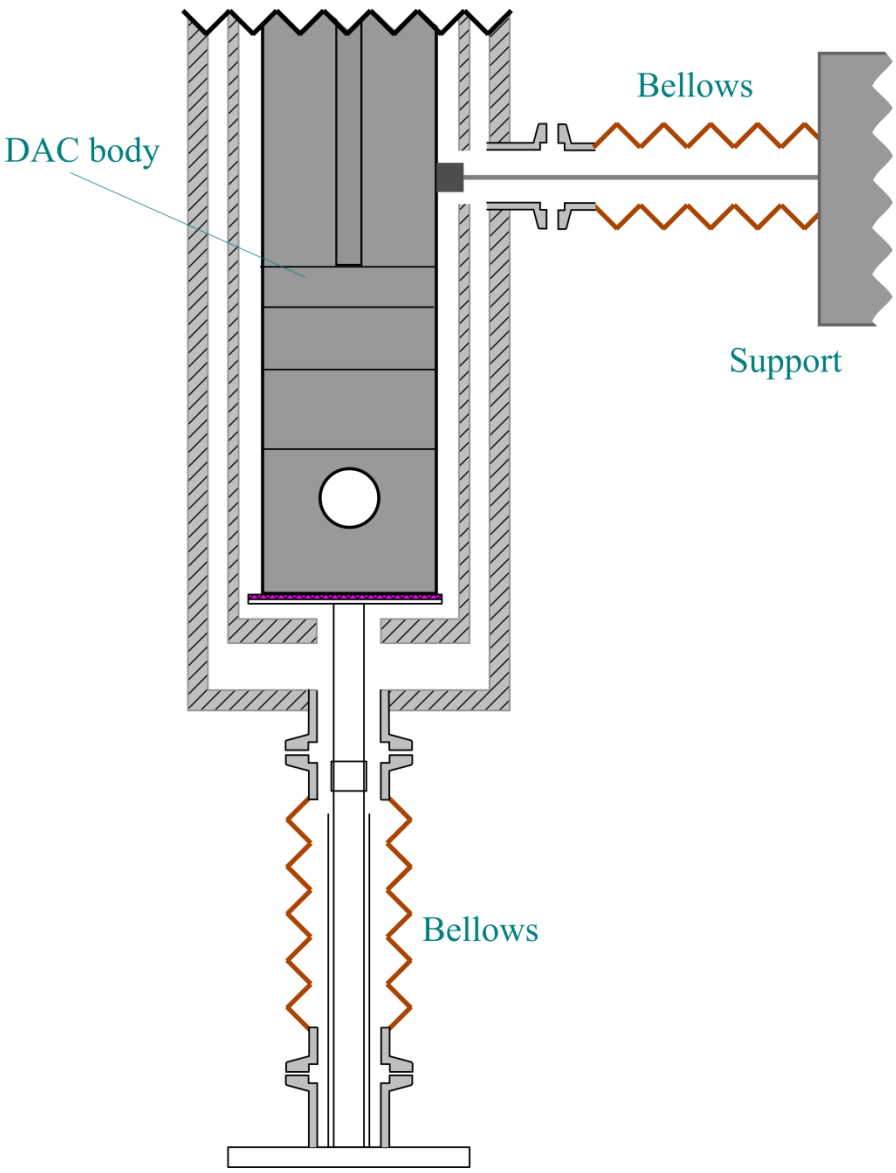

Figure 6.6: DAC in Cryostat Front view. Not to scale

The vibration performance was confirmed using a simple video setup: the actual DAC with a 50 micron sample hole was mounted in the cryostat at the position of a sample. It was back illuminated and imaged on a CMOS 30 frames per second camera with magnification such that about 2 camera pixels corresponded to 1 micron in the sample space. The video feed was processed so that for every frame the image position and broadening due to motion blur was calculated. The observed vibration levels were 2($\pm$1) and 1($\pm$0.5) micron root mean square for horizontal and vertical directions, respectively. A typical

time trace of rms vibration amplitude is shown n Fig. 6.7. No excess broadening above the motion blur was observed suggesting the amplitude of the vibration with frequencies above the camera frame rate is not significant.

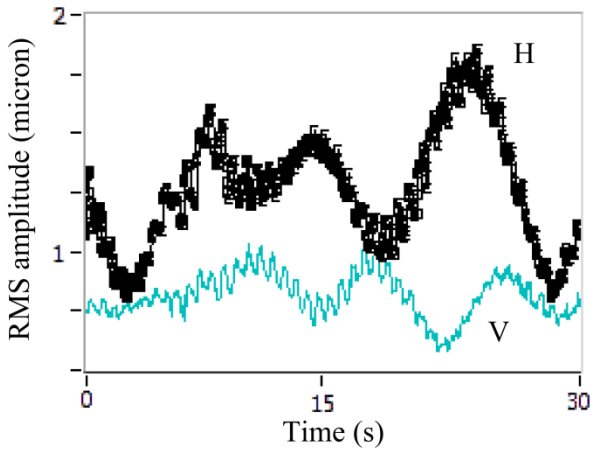

Figure 6.7: Typical rms vibration amplitude for horizontal (H) and vertical (V) directions as a function of time.

6.4 Conclusion

A cryogen free cryostat based on Sumitomo (?) GM cryocooler has been developed and tested for optical measurements in a diamond anvil cell. The cryostat features small optical working distance of ~50 mm. The metal DAC to be cooled has physical dimensions of ~2x2x6 inches and mass of ~2 kg. The vibrations inherent to a GM cryocooler are suppressed enough to allow optical measurements of micron scale samples.

Benefits of this design include its simplicity - it can be built in a typical machine shop from commercially available stock materials and without welding. The rectangular optical tail enables shorter working distance optics. In practice it can run 24 hours a day at low temperature, not requiring periodic helium or liquid nitrogen transfers. This results in economic operation and little low temperature maintenance. A problem inherent to the single vacuum space design is the vulnerability to runaway gas

desorption: in the case of a slow gas leak (say during the loading of the sample) into the vacuum chamber the gas is cryopumped onto the second stage. If the leak rate is too fast or the second stage temperature is allowed to rise, the second stage desorbs the gas and the thermal exchange with the room temperature walls leads to run away temperature rise. This problem can be countered with a high speed vacuum pump connected to the cryostat.

6.5 Bibliography

[1] I. Silvera and R. Wijngaarden., "Diamond anvil cell and cryostat for low temperature optical studies," *Rev. Sci. Instrum.,* vol. 56, no. 121, 1985.

7. Appendix – Instrumentation and Techniques

7.1.Detailed Loading Procedure

Presented is a step by step sequence for the cryogenic DAC loading routine which was used in the hydrogen runs

- Seal the cell at room temperature, mount it in the cryostat and set diamond separation to 50 μm. As the cell cools down interdiamond separation decreases, thus there is some margin left above 20μm, which is the gasket thickness.
- Before cooling, evacuate mini chamber and exchange gas chamber, fill the mini chamber with hydrogen above 1 atm to prevent contamination of the sample with air.
- Cool down to helium temperature and collect ruby fluorescence spectrum as a reference
- Warm the cell above the melting temperature of hydrogen and control the temperature at 15K to maintain hydrogen in liquid state.
- Note the starting diamond separation and start condensing hydrogen in until the nd value jumps by 10%
- Set the flow of hydrogen to stabilize pressure in MC manifold at 1.5 atm to compensate for slow possible leaks.
- Note the strain gauge meter reading and start closing the cell. As diamonds advance the nd value first drops (as a function of lead screw position) because the pressure of liquid hydrogen is essentially constant. When the diamonds touch the gasket, the nd value stops changing as the load is increased. The moment of touch is clearly observable in reflected light because of fringes at gasket-diamond interface.
- Increase the load on the sample above the gasket compressive strength to seal the sample. When the gasket is starting to yield (as seen by decreasing hole size) nd value should not change much, because decrease in thickness is essentially compensated by increase in hydrogen index of refraction if it is sealed.

- Cool down to liquid helium temperature to decrease the risk of boiling the hydrogen out in case of a bad seal and measure ruby fluorescence to confirm the pressure.
- Pump away the unused hydrogen and warm up the cryostat while monitoring the sample pressure. It increases because of frozen in load in the indium seal is released during the warm up. If the pressure is increasing above the desired value the load on the sample can be decreased to stay in the desired pressure range.